GARCIA

CENTER FOR POLYMERS AT ENGINEERED INTERFACES

2025

Research Scholars Program

Summer 2025

This year the Garcia Program was marked by an outstanding broad range of interests in the basic sciences. We were very proud of our students who formed interdisciplinary teams to address multiple challenges facing society today. The students, who have multiple talents, designed logos which expressed their views of the program. The following logos were selected by their peers to represent the group;

The runner up was designed by Danica Stout which illustrates some of the experimental groups which formed spontaneously this year—they ranged from the pipette—representing spin casting, contact angle, representing surface energy engineering, chemistry, and flame retardants—or the leaves that resist adversity and flower despite the fires.

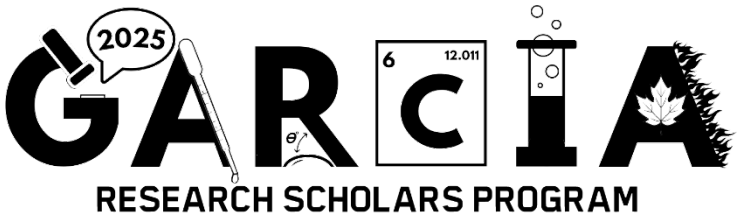

The winning logo was designed by Danielle Lu who describes the logo as follows;
"*In this logo, I wanted to encapsulate the diverse interests here at Garcia. I included the stethoscope for medicine, and the DNA and polymer for kids interested in genetics and chemistry. The combination of the "2025" and the test tube and some letters with objects/Stonybrook logo represented my passions for art and science meshing together.*

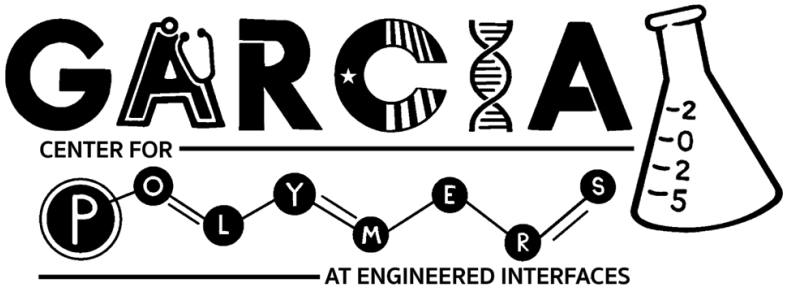

The Garcia Center for Polymers at Engineered Interfaces was founded in 1996 and is named after the late Queens College professor, Narciso Garcia, who was a pioneer in the integration of education and research. The Center focuses on the broad application of materials research to engineering, medicine, and energy, and recently, AI, machine learning, and computational modeling. The Center also supports innovation through entrepreneurship and has multiple collaborations with industry and national laboratories. In the research program, high school students work together with undergraduates, PhD , post PhD and faculty who collaborate in addressing challenges at the cutting edge of modern science. The students are encouraged to publish in refereed scientific journals, present their results at national conferences, and develop patents to protect their intellectual property. Our goal is to convey to the students the excitement we enjoy daily in research and provide for them a supportive network within the scientific community. Research is a lifelong experience and we hope to remain as a resource to our students long after "graduation".

Sincerely,

Miriam Rafailovich and Jon Sokolov

High School Students

Chetas Aduri


Ishita Bafna

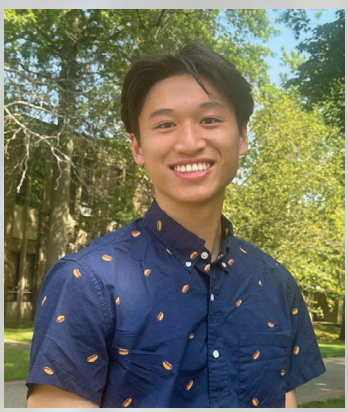
Christian Chan

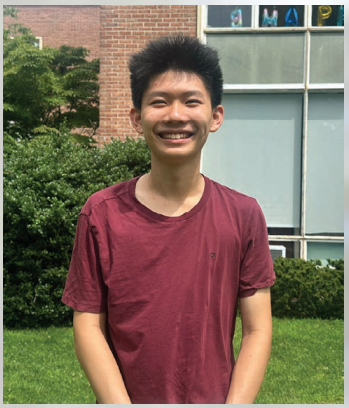
Alexander Cheng

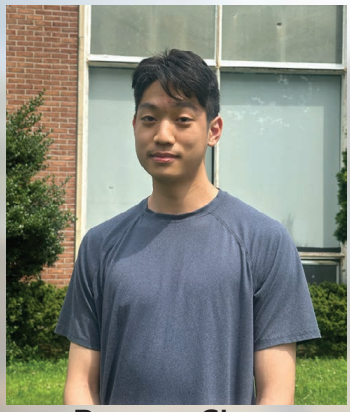
Benson Chou


Sarah Dabees


Katelyn Deng


Emily Do


Kayla Etra


Harper Falivene

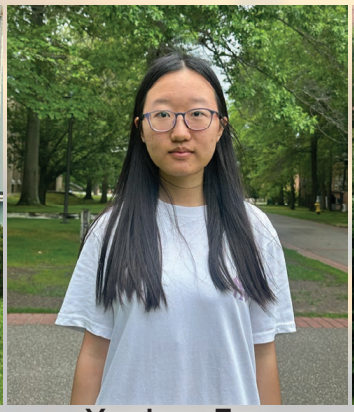
Xuehan Fan


Joshua Feigenbaum

Madeleine Gaillard


Nathaniel Gao


Zhanhui (Lemi) Gao


Jerry Gu

High School Students


Ryan Gu


Christian Hackett


Yixuan (Michael) He

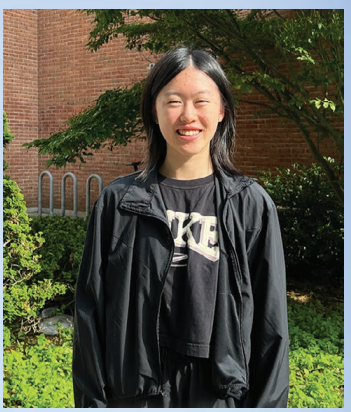
Chloe Ho


Lucas Hofflich

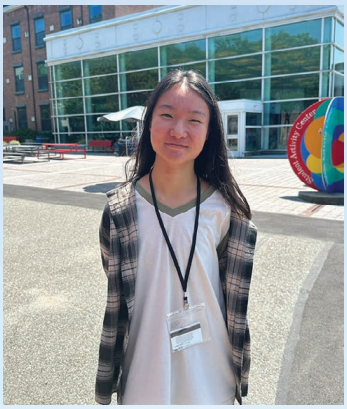
Alice Hu

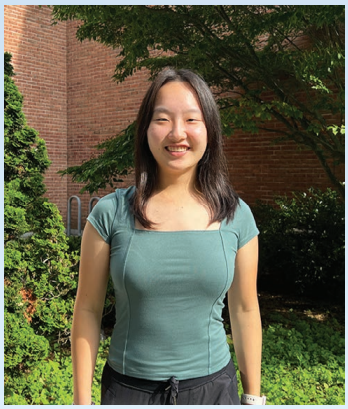
Audrey Huang

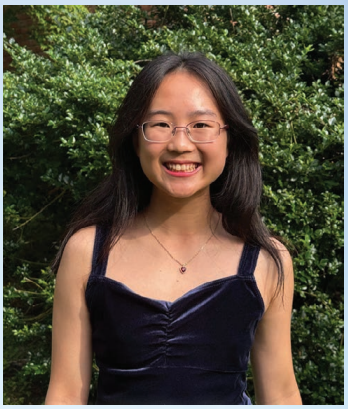
Charlotte Huang

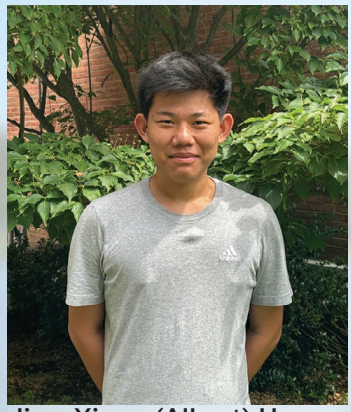
Jing-Xiang (Albert) Huang

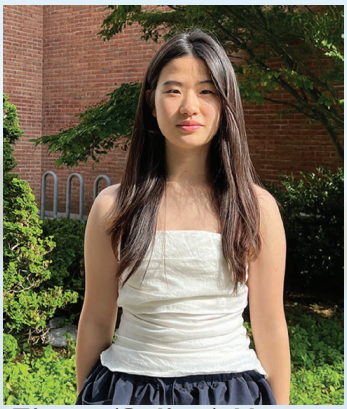
Ziyan (Selina) Huang


Nirati Iyer

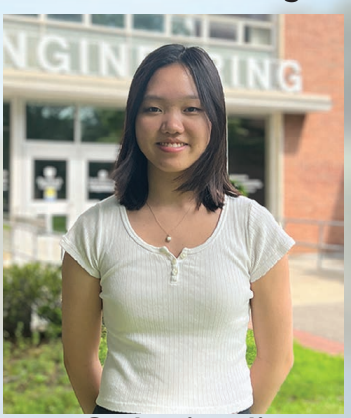
Catherine Ji


Eric Ji


Andy Jiang

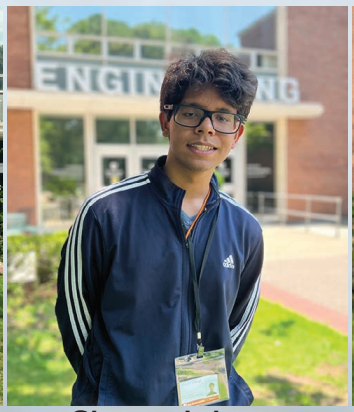
Shaun Johnet


Alli Katila-Miikkulainen

High School Students


Ian Kim

Juwon (Joelle) Kim

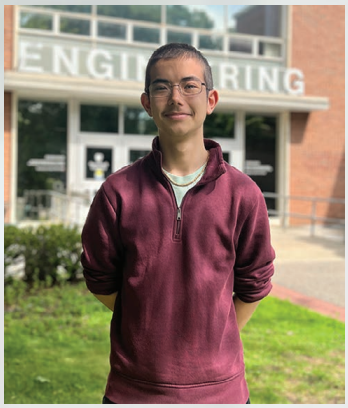
Cassidy Kirschenbaum


Aiden Kwon


Sze Tin (Kitty) Lai

Rachel Lee

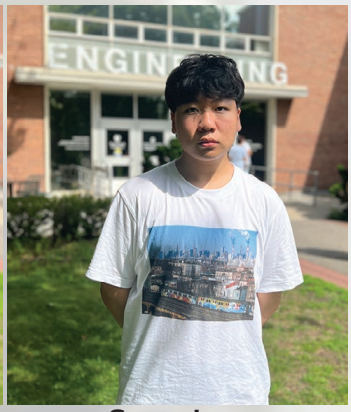
Sean Lee


Chunman Li

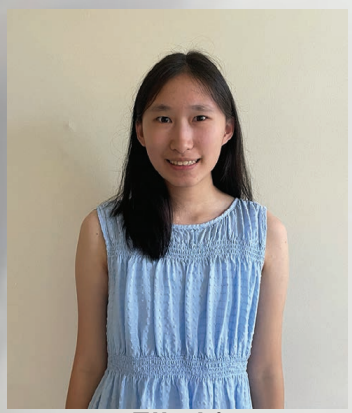
Ella Li

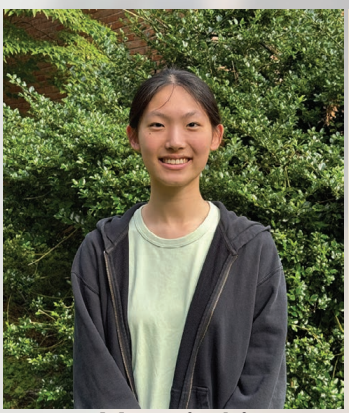
Maggie Li


Shuyan (Emily) Li


Xinying (Louis) Li


Xinyu (Tiffany) Li


Fangqi (Felicity) Liao

Shawn Lim


Eric Lin

High School Students


Evan Liu


Rosalie Liu


Danielle Lu


Julianne Mayetani


George Mirgorodskiy


Aaratrika Mondal


Suhrith Muvvala

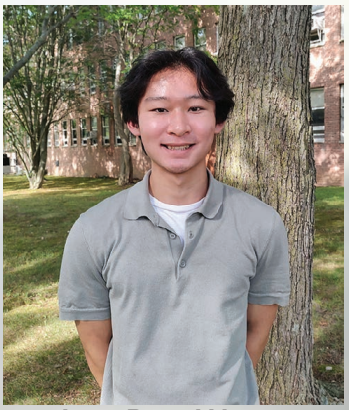
Leo Pan-Wang


Krish Patel


Nina Pfeffer

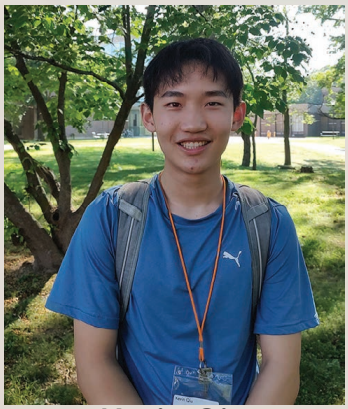
Kevin Qiu

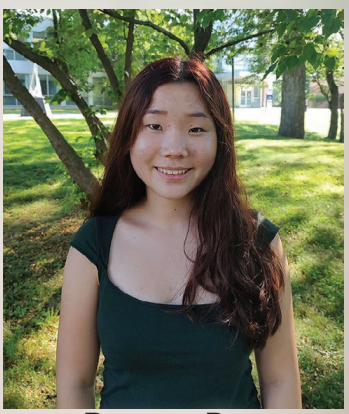
Brenna Ren


Kaden Ren


Emily Segall


Liaoliao (Eric) Shi


Chloe Shim

High School Students

Ishmeet Singh


Caleb Son

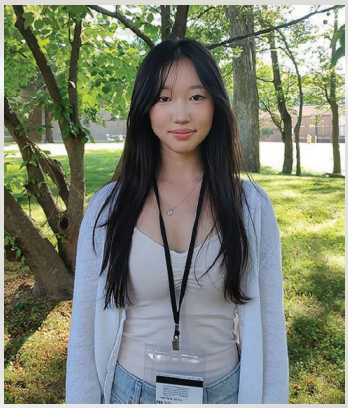
Yeji Son

Ahyoung Song


Eun-Seo (Emily) Song


Jasper Stackawitz


Danica Stout


Sarah Sullivan

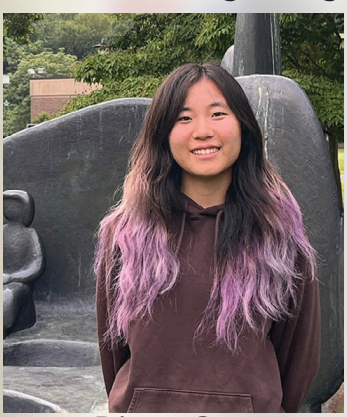
Diana Sun


Alessandro Verona


Timur Volkov

Alyssa Wang


Andrew Wang


Christopher Wang


Xuandi (Mathieu) Wang

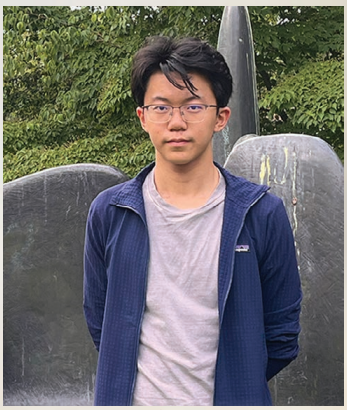
Mengdi (Oscar) Xie

High School Students

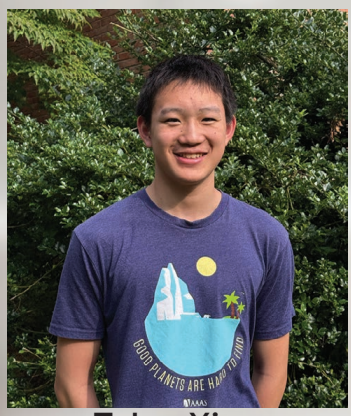

Talon Xing

Ke (Cleo) Xu

Max Xu

Chujia (Susie) Yang

Hanyuan Yang

Yuanxi (Cici) Yao

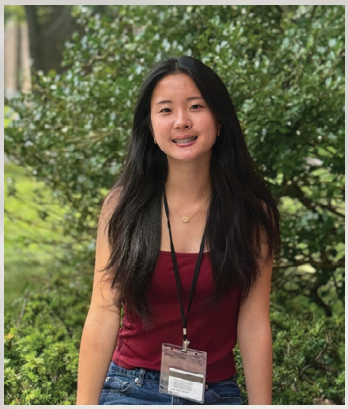

Chloe Yim

Kiara Yoon

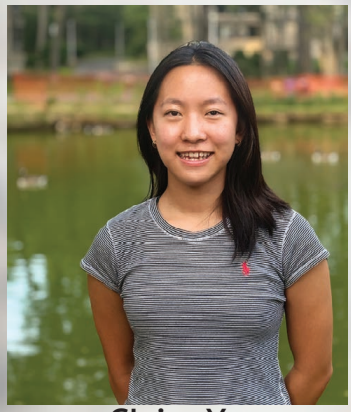

Claire Yu

Wenxin (Wendy) Yu

Ian Zhang

Kevin Zhang

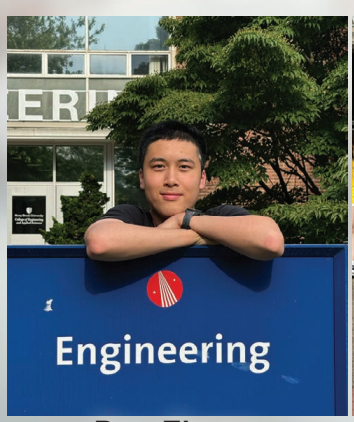

Ray Zhang

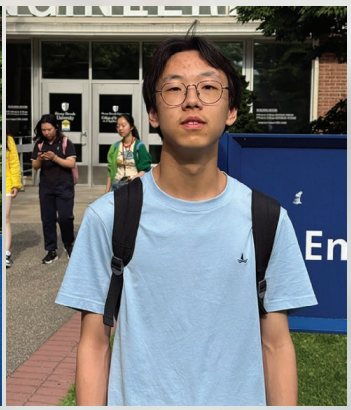

Yicheng (Ken) Zhang

Anthony Zhao

Connor Zhao

High School Students

Yanguo (Spark) Zhao

Daniel Zhou

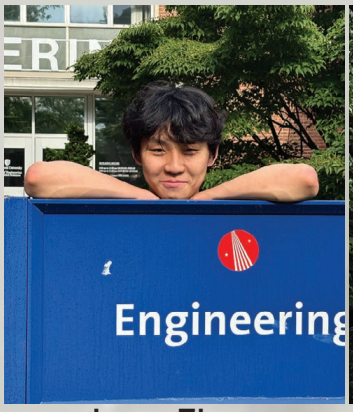

Leon Zhou

Lingfei (Angel) Zhu

Research Experience For Undergraduates (REU)

Christian Apostol

Jessica Bogen

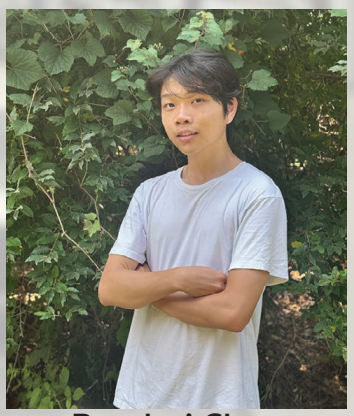

Bandari Chen

Fiona Chen

Damien Crowley

Sahana Dhama

Bernard Essuman

Research Experience For Undergraduates (REU)


Jashmin Gill

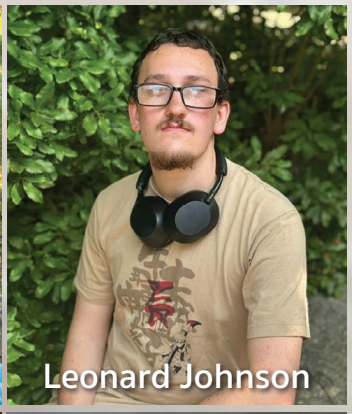
Leonard Johnson


Laila Juma


Kira Klayman


Krystal Lazo

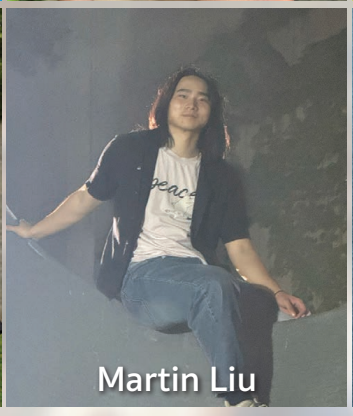
Martin Liu


Tabarjah Neal

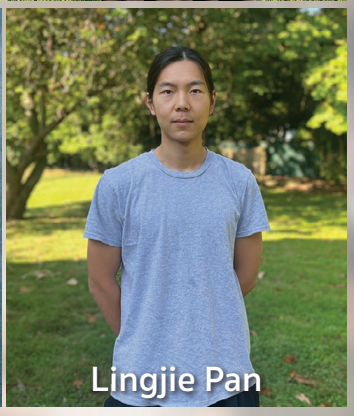
Lingjie Pan


Cosmo Perfetti


Hugh Rosshirt


Amanda Salanitri


Sam Specht

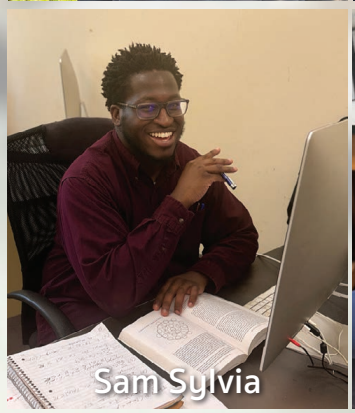
Sam Sylvia


Briman Yang


Selina Zhang


Phoebe Zheng

Graduate Students


Allen Bethancourt


Muyun Cui


Sangita Das


Haoyan Fang


Yiwei Fang

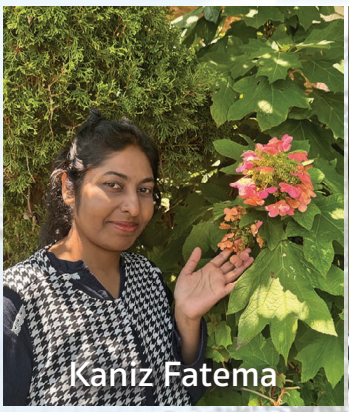
Kaniz Fatema


Shi Fu

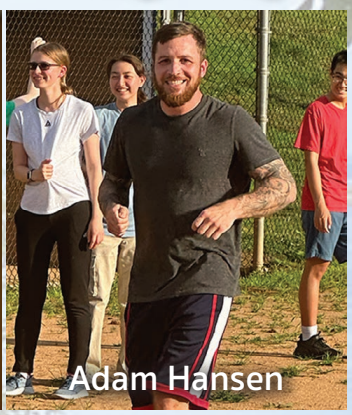
Adam Hansen


Karin Hasegawa


Jessica Hofflich


Zoe Katevatis


Huiting Luo


Dezhao Meng

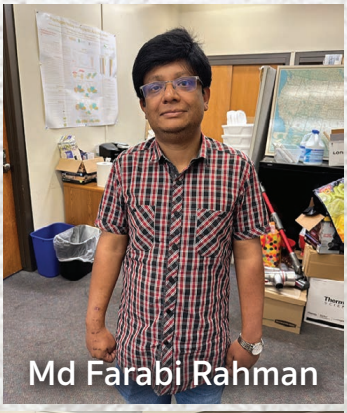
Md Farabi Rahman


Nabila Tripti

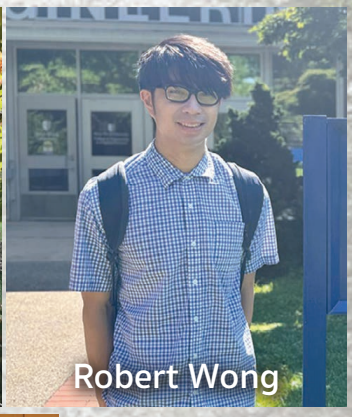
Robert Wong


Ashraful Islam


Kuldeepsinh Raj

Faculty/Staff

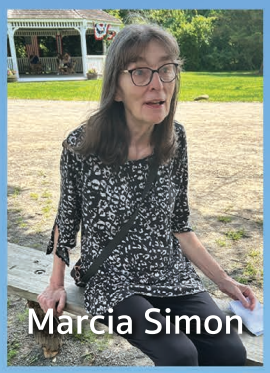
Marcia Simon

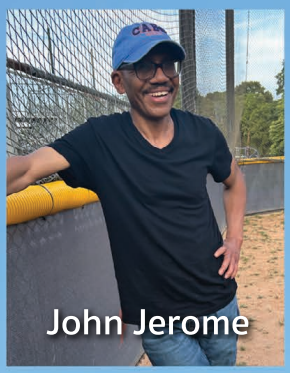
John Jerome

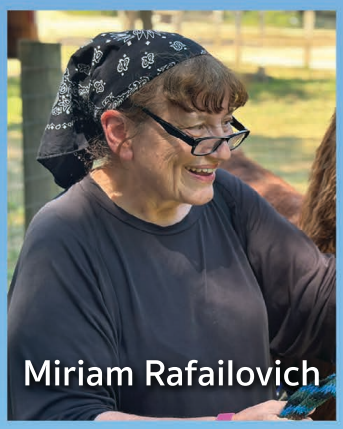
Miriam Rafailovich


Mike Cuiffo

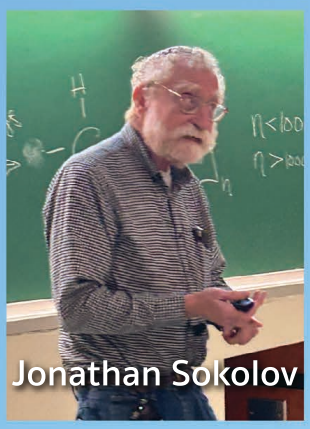
Jonathan Sokolov


Zhixing (Tony) Huang

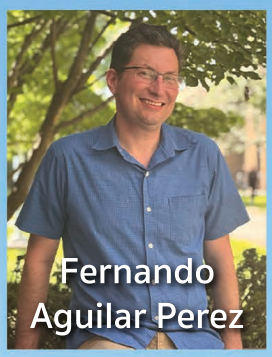
Fernando Aguilar Perez


Aaron Sloutski


Akash Pati

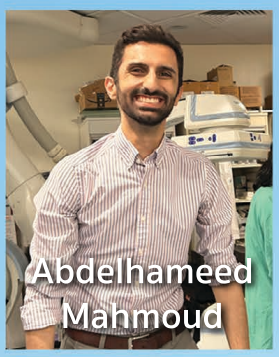
Abdelhameed Mahmoud


Dilip Gersappe


Taejin Kim


Yuefan Deng


Nidhi Rajput


Michael Mak

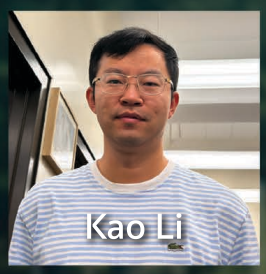
Kao Li


Shoumik Saha


Chander Sadasivan


Jay Gao


Hyeonji Park


David Black


Rebecca Isseroff


Herb Weiss


Gurtej Singh


David Sprouster

Research Bootcamp!

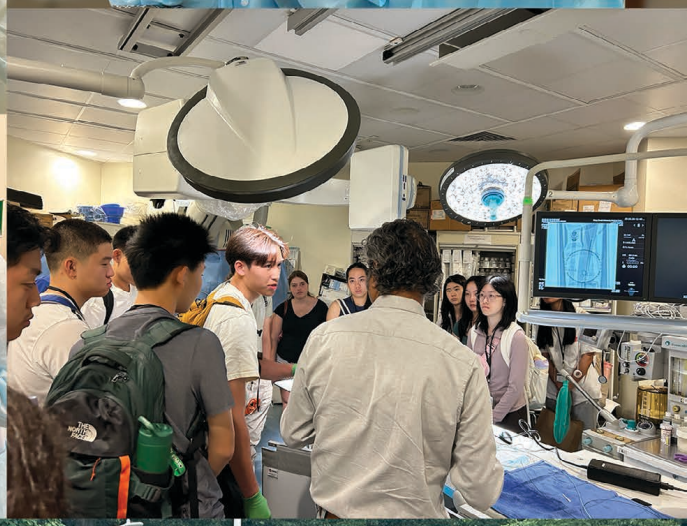

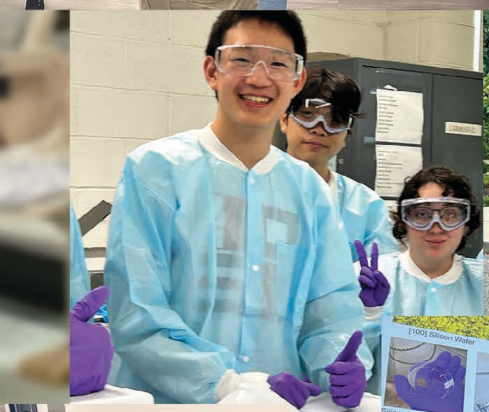

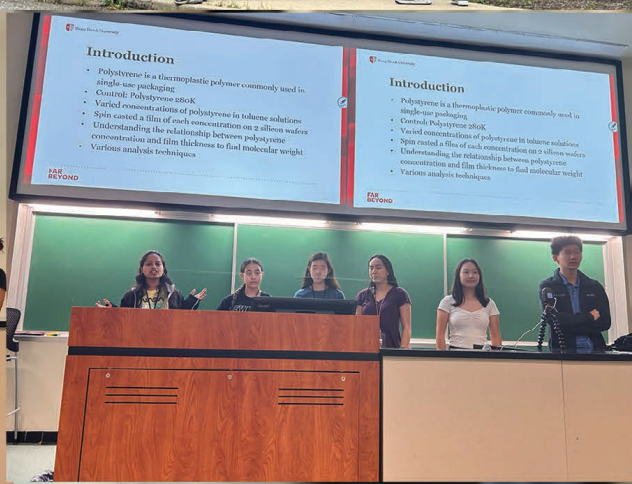

Presentations!

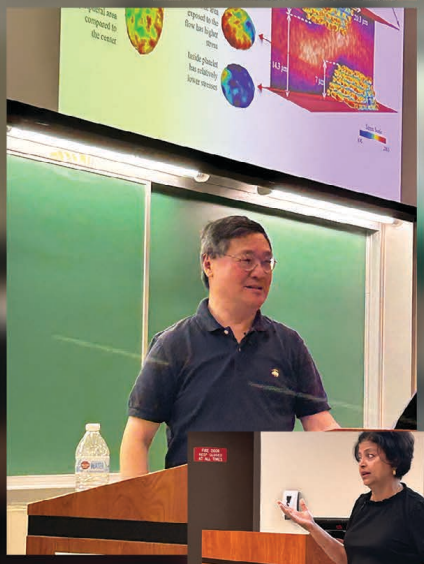

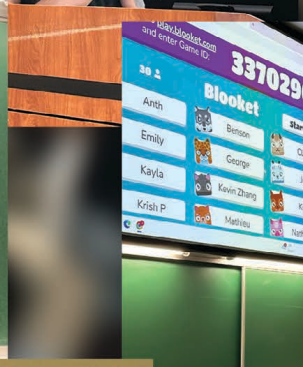


Fishing!
adidas
SCIENCE
CG


Canoeing!


SAFEAIRE

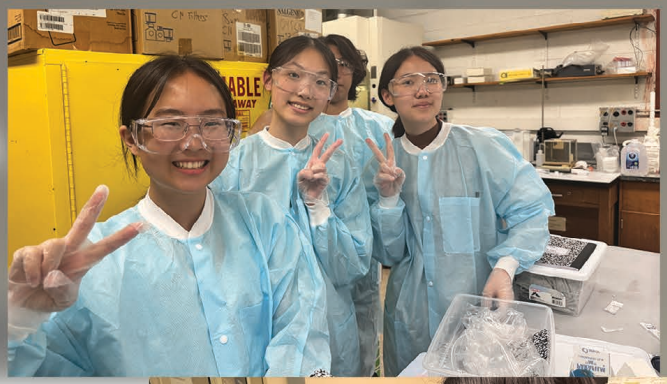

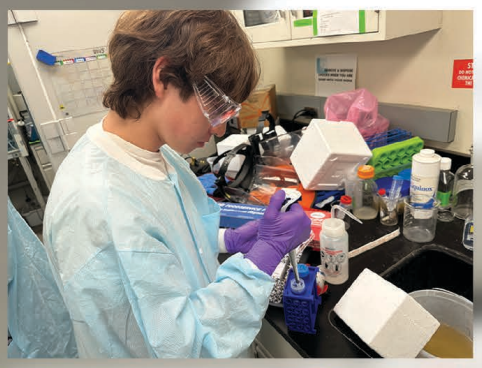

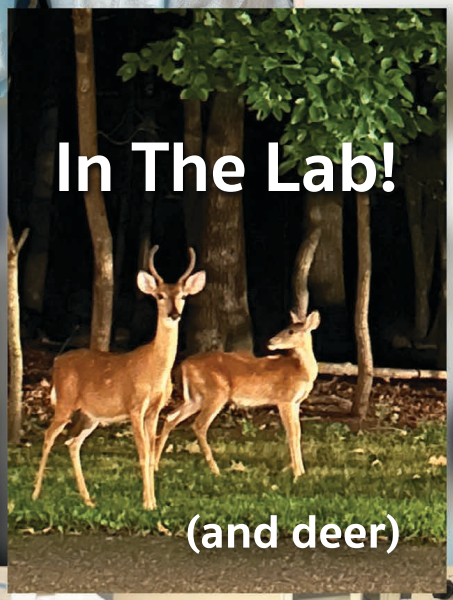
In The Lab!
(and deer)

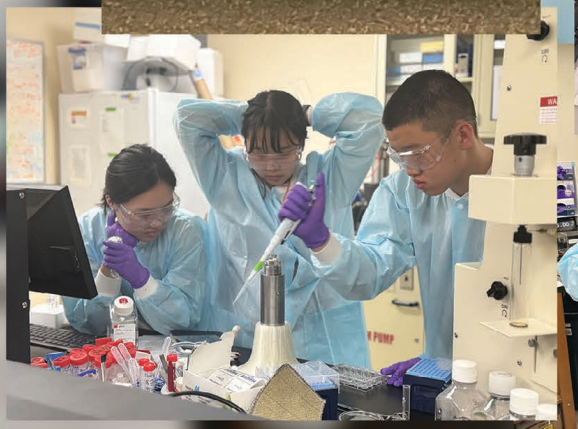

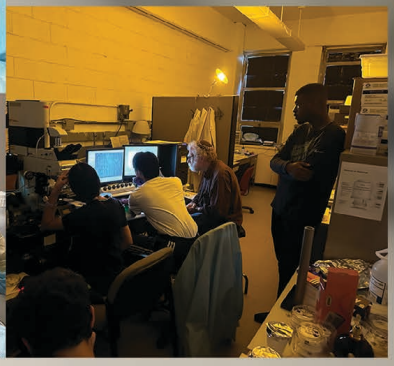


PluCoil
In-Vitro aneurysm filling
Injection pressure
Rheological study of F88DMA- F88 blends
Vessel forming and hydrogel coating
Cell adhesion and proliferation on F88DMA- F88 blends
Swelling of F88DMA-F88 blends
DSC of F88DMA-F88 blends
PluCoil packing density
Injection pressure 2nd method
Cell adhesion and proliferation on F88DMA-Eb, CoK,Xan blends
Stony Brook University
FAR BEYOND

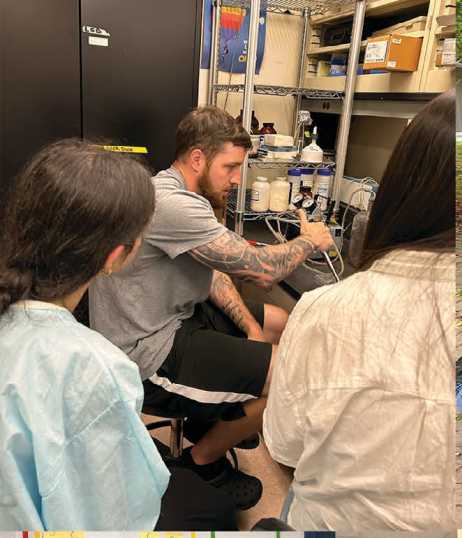



Rheological study of F88DMA-F88 blends
Vessel forming and hydrogel coating
Cell adhesion and proliferation on F88DMA-F88 blends
Swelling of F88DMA-F88 blends
DSC of F88DMA-F88 blends
Cell adhesion and proliferation on F88DMA-F8, Col, Vah blends
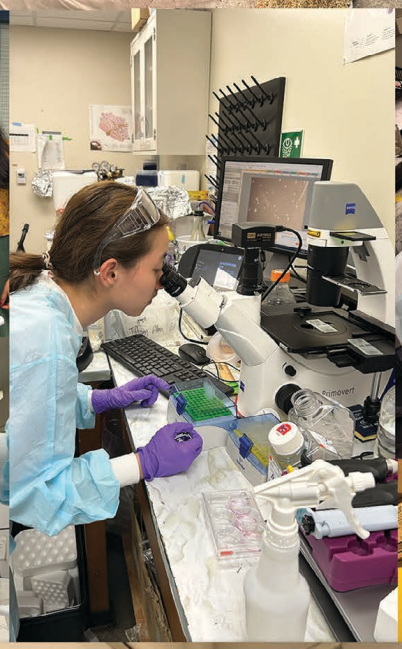
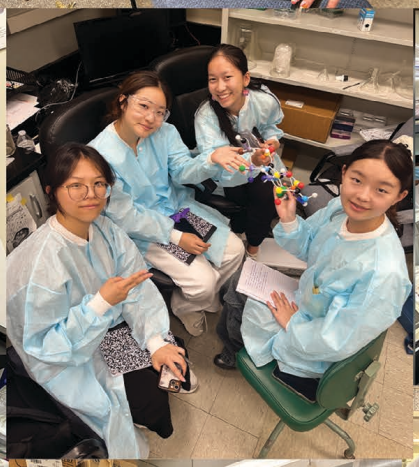


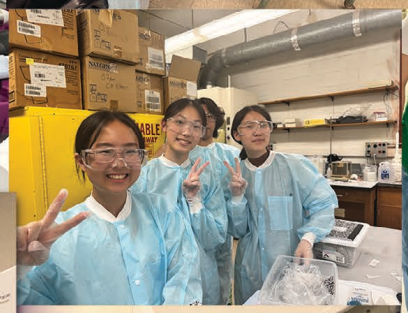

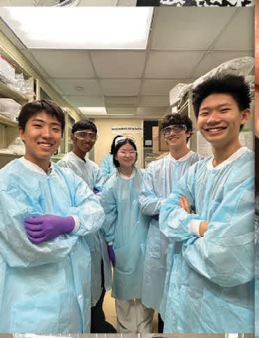





STONY BROOK SOFTBALL
CHAPIN RAINBOW STAGE
Canon
Getting Outside!


Ropes Course!
Jones Beach!
Nature Center!

Brookhaven® National Laboratory

Summer Sundays

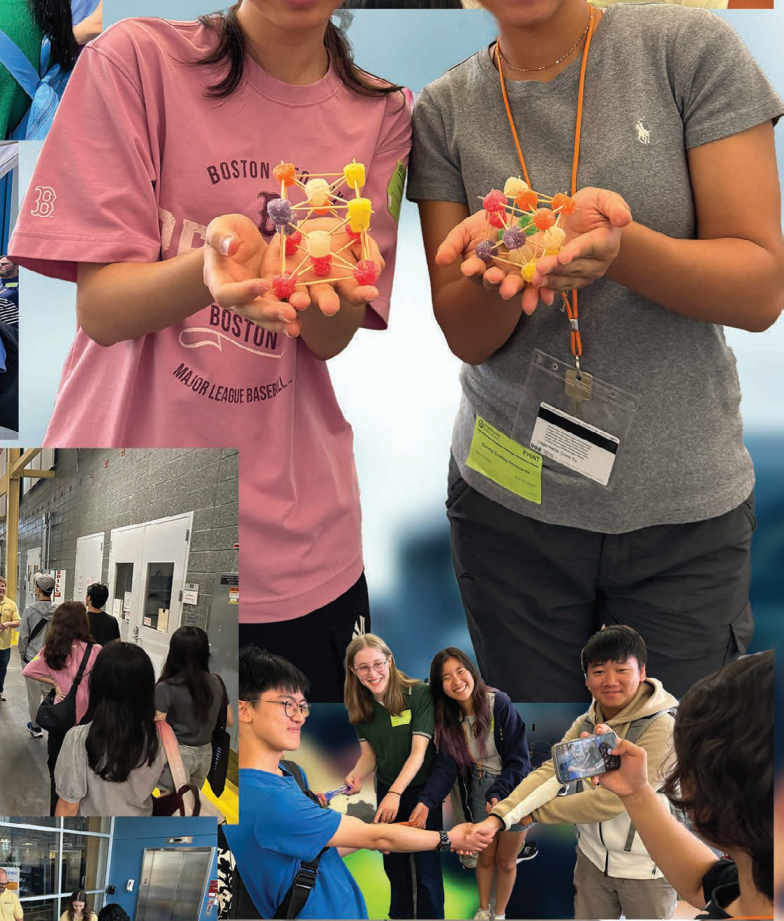

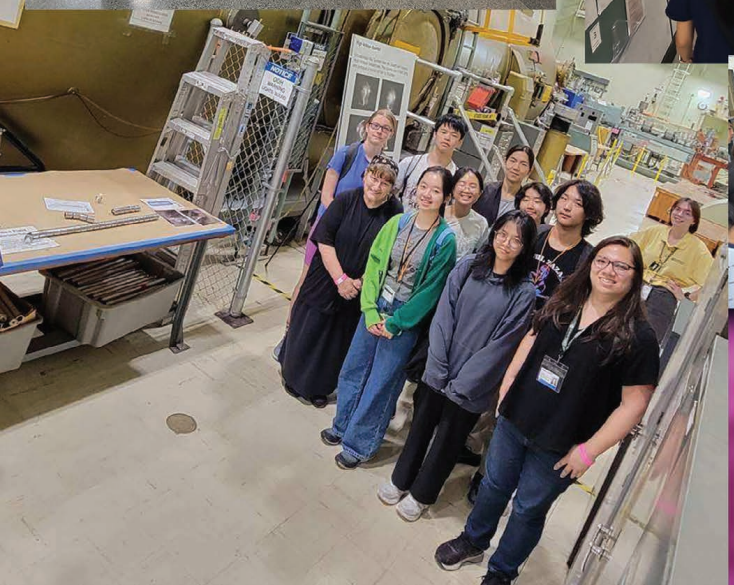

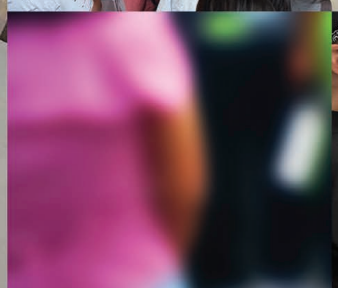

Student Presentations!

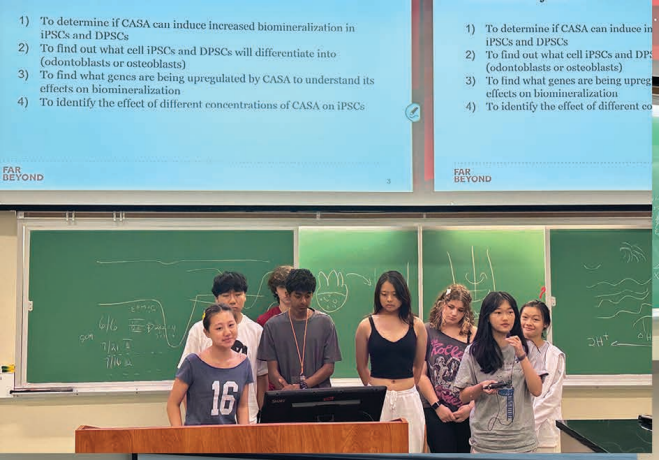

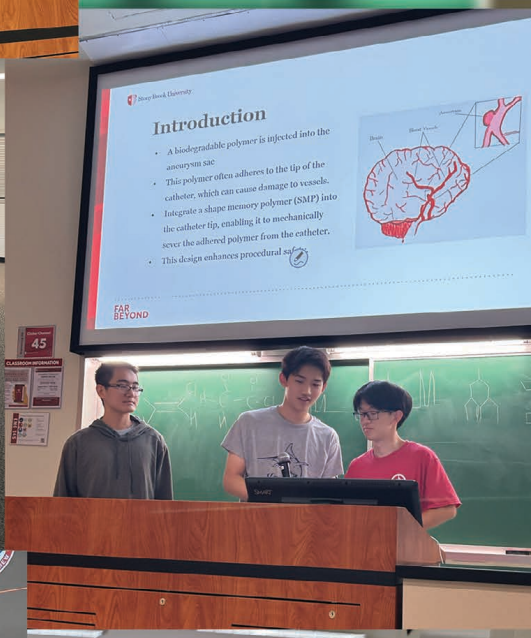

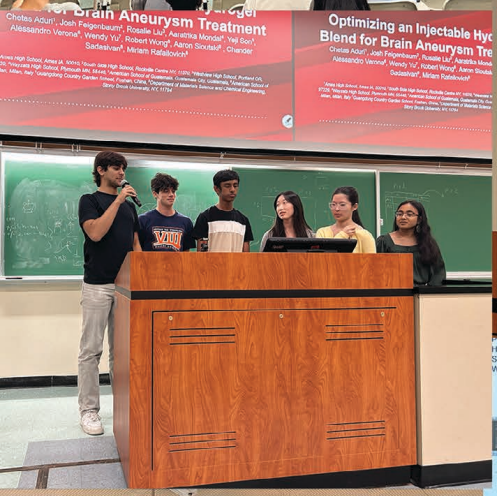

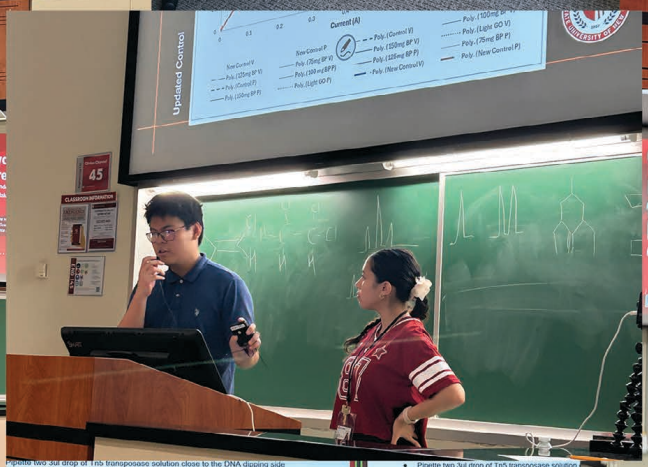

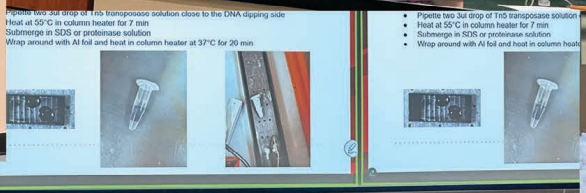

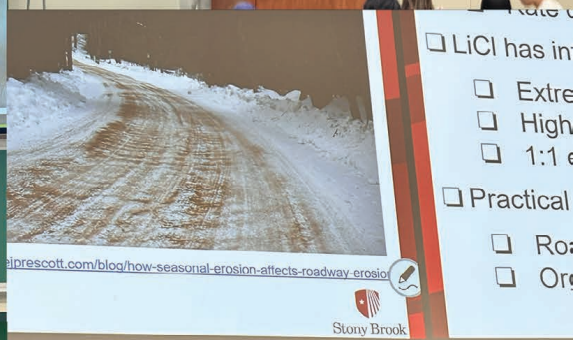





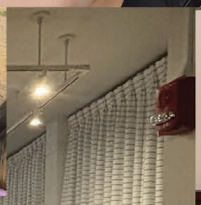


Let us CAKE!
ORDER HERE





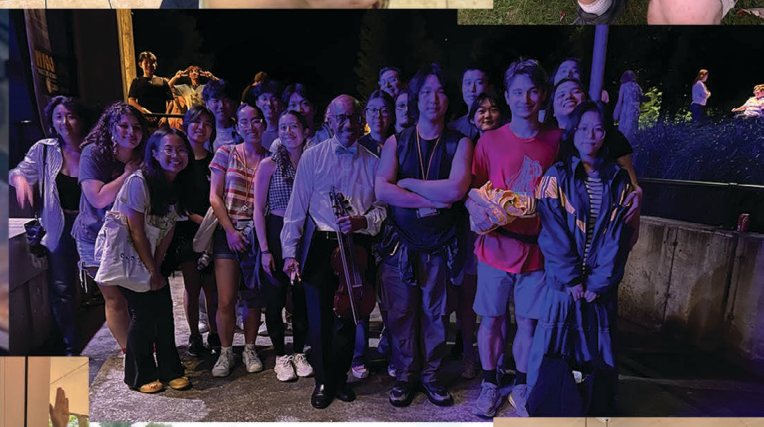












DUKE




CARDOZO HALL


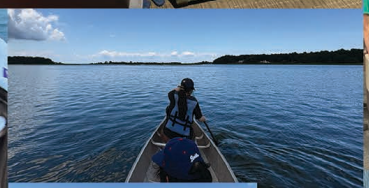


American Girl
SMURFS


BUT AVERAGE
Stony Brook University


ESCAPE QUEEN
I NEED a DRINK!
BEST TEAM EVER
IT'S MY BIRTHDAY





THE MET








Summer Scholar Schedule of Weekly Activities

Each day starts with a mandatory group meeting at 10:15 AM!

Daily Schedule: Week of 6/26

			Thursday – 6/27	Friday – 6/28
			10:15 – 10:30: Greetings by: SBU Provost Dr. Carl Lejuez & Morin Charitable Trust Officer Steve Vaccarelli **10:30 – 11:15:** Dr. Steve Walker: Working with Bacteria & Microbial Resistance **11:15 – 12:00:** Dr. Tai-De Li: XPS, TOF-SIMS, & AFM Imaging **12:00 – 12:45:** Dr. Dennis T. Lee: Exploring Porous Materials **12:30 – 1:00:** Pizza Working Lunch **1:00 – 4:15:** Facilities Tour **4:15:** Ice Cream!	**10:15 – 10:30:** Organizational Meeting **10:30 – 11:45:** Madeline Augustine: Working at Boeing **11:45 – 12:15:** Pizza Working Lunch **12:15 – 1:00:** Prof. Vitaly Citovsky **1:00 – 1:45:** Prof. Y-X Qin **1:45 – 2:15:** Dr. Abdelhameed Mahmoud, DDS

Summer Scholar Schedule of Weekly Activities

Each day starts with a mandatory group meeting at 10:15 AM!

Daily Schedule: Week of 6/30

Monday – 6/30	Tuesday – 7/1	Wednesday – 7/2	Thursday – 7/3	Friday – 7/4
10:15 – 10:30: Organizational Meeting **10:30 – 11:15:** Dr. Aaron Slouski **11:15 – 12:00:** Prof. Taejin Kim **12:00 – 1:00:** Lunch **1:00 – 1:50:** Dr. Chander Sadasivan **1:50 – 2:40:** Prof. Nidhi Rajput **2:40 – 3:30:** Prof. Michael Mak **3:30 – 4:20:** Prof. Dilip Gersappe **4:00:** Ice Cream!	**10:15 – 10:30:** Organizational Meeting **10:30 – 11:30:** Dr. Adam Singer **11:30 – 12:45:** Prof. Jonathan Sokolov **12:45 – 1:45:** Lunch **1:45 – 3:00:** Dr. Ulas Sunar **3:00 – 5:00:** Journal Club: Student Presentations **4:00:** Ice Cream!	**10:15 – 10:30:** Organizational Meeting **10:30 – 11:30:** Dr. Ying Liu, EH&S: Chemical Safety Training **11:30 – 12:15:** Walter Julias, EH&S: Waste Management Safety Training **12:15 – 1:15:** Lunch **1:15 – 3:00:** Facilities Tour Part I **3:00 – 3:45:** Rebecca Isseroff: Graphene Oxide **3:45 – 4:45:** Supercritical CO_2 Presentation **4:00:** Ice Cream!	**10:15 – 11:15:** Chris Kuhlow, EH&S: Biosafety Training **11:15 – 12:15:** Janet Oseni, EH&S: Radiation Safety Training **12:15 – 1:00:** Lunch **1:00 – 4:00:** Facilities Tour Part II **4:00 – 5:00:** Dr. Gurtej Singh **4:00:** Ice Cream!	**Happy Fourth of July!!** 

Summer Scholar Schedule of Weekly Activities

Each day starts with a mandatory group meeting at 10:15 AM!

Daily Schedule: Week of 7/7

Monday – 7/7	Tuesday – 7/8	Wednesday – 7/9	Thursday – 7/10	Friday – 7/11
10:15 – 10:30: Organizational Meeting **10:30 – 10:50:** Safety Exam **10:50 – 11:20:** Rebecca Isseroff: Keeping a Lab Notebook **11:20 – 11:30:** Lab Box Distribution **11:30 – 4:30:** Spin Casting Experiment Day I **4:00:** Ice Cream!	**10:15 – 10:30:** Organizational Meeting **10:30 – 4:00:** Spin Casting Experiment Day II **4:00:** Ice Cream!	**10:15 – 10:30:** Organizational Meeting **10:30 – 11:15:** Dr. Michelle Hutchins: VIPER @ UPenn **11:15 – 11:45:** Dr. Ying Liu, EH&S: SOP Training **11:45 – 12:30:** Statistics Lecture & Spin Casting Data Analysis **12:30 – 1:30:** Lunch **1:30 – 2:15:** Dr. Stephen Walker **2:15 – 4:15:** Project Talks: & Ice Cream! Dr. Shoumik Saha Prof. Jonathan Sokolov Dr. Wilson Lee & Dr. Bicheng Wu Rebecca Isseroff **5:00 – 9:00:** Fishing on Celtic Grace in Port Jefferson	**10:15 – 10:30:** Organizational Meeting **10:30 – 11:15:** Dr. Tai-De Li: XPS & Materials Characterization **11:15 – 12:30:** Project Talks: Dr. Aaron Sloutski Adam Hansen Bernard Essuman **12:30 – 1:15:** Project Talks: Dr. Haoyan Fang, Md Farabi Rahman, Allen Bethancourt Dr. Tony (Zhixing) Huang Yiwei Fang, Damien Crowley, Dr. Akash Pati Dr. Shi Fu **4:00:** Ice Cream!	**10:15 – 10:30:** Organizational Meeting **10:30 – 11:15:** Battle of the Spin Casting Groups! Student Presentations **11:15 – 12:30:** Project Talks: Dr. Shi Fu, Huiting Luo, Muyun Cui **12:00:** Working Pizza Lunch **12:30 – 1:00:** Project Talks: Rajput Theory Group Adam Hansen **1:00 – 2:45:** Selection of Projects

Summer Scholar Schedule of Weekly Activities

Each day starts with a mandatory group meeting at 10:15 AM!

Daily Schedule: Week of 7/14

	Monday – 7/14	Tuesday – 7/15	Wednesday – 7/16	Thursday – 7/17	Friday – 7/18
7/13: **Field Trip to BNL NSLS-II!**	**10:15 – 10:30:** Organizational Meeting **10:30:** Write SOPs and start **Lab Work!** (According to your group's schedule)	**10:15 – 10:30:** Organizational Meeting **10:30 – 10:45:** Introduction to JESTI (Journal of Ethics in Scientific and Technological Innovations): Kevin Zhang **10:45:** **Lab Work!** (According to your group's schedule)	**10:15 – 10:30:** Organizational Meeting **10:30:** **Lab Work!** (According to your group's schedule) **5:30 – 8:00:** Annual Garcia Softball Game! Feat. Dunkin' and Baskin Robbins!	**10:15 – 10:30:** Organizational Meeting **10:30 – 11:15:** Atomic Layer Deposition: Dr. Chang Yon Nam **11:15:** **Lab Work!** (According to your group's schedule)	**10:15 – 10:30:** Organizational Meeting **10:30:** **Lab Work!** (According to your group's schedule) **12:00:** Working Pizza Lunch

Summer Scholar Schedule of Weekly Activities

Each day starts with a mandatory group meeting at 10:15 AM!

Daily Schedule: Week of 7/21

	Monday – 7/21	Tuesday – 7/22	Wednesday – 7/23	Thursday – 7/24	Friday – 7/25
7/20: **Field Trip to Nassau Pops Symphony Orchestra**	**10:15 – 10:30:** Organizational Meeting **10:30 – 11:30:** Intellectual Property: Donna Tuminello **11:30:** **Lab Work!** (According to your group's schedule)	**10:15 – 10:30:** Organizational Meeting **10:30 – 11:15:** Writing the Perfect Abstract: Prof. Lashmi Rai **11:15:** **Lab Work!** (According to your group's schedule)	**10:15:** **Annual Garcia Canoe Trip!**  **3:00:** **Lab Work!** (According to your group's schedule)	**10:15 – 10:30:** Organizational Meeting **10:30:** **Lab Work!** (According to your group's schedule)	**10:15 – 10:30:** Organizational Meeting **10:30:** **Lab Work!** (According to your group's schedule) **11:30:** Working Pizza Lunch and Student Research Presentations

Summer Scholar Schedule of Weekly Activities

Each day starts with a mandatory group meeting at 10:15 AM!

Daily Schedule: Week of 7/28

	Monday – 7/28	Tuesday – 7/29	Wednesday – 7/30	Thursday – 7/31	Friday – 8/1
7/27: **Field Trip Jones Beach Energy and Nature Center and WildPlay Ropes Course!**	**10:15 – 10:30:** Organizational Meeting **10:30 – 11:15:** Fire Safety Training: Fire Marshall Scott Gershowitz **11:15:** **Lab Work!** (According to your group's schedule) **4:00:** Ice Cream Social and Student Research Presentations	**10:15 – 10:30:** Organizational Meeting **11:15:** **Lab Work!** (According to your group's schedule) **4:00:** Ice Cream Social and Student Research Presentations	**10:15 – 10:30:** Organizational Meeting **10:30:** **Lab Work!** (According to your group's schedule) **4:00:** Ice Cream Social and Student Research Presentations	**10:15 – 10:30:** Organizational Meeting **10:30 – 11:15:** Presenting at the Materials Research Society Conference: Marla Boots **11:15:** **Lab Work!** (According to your group's schedule) **4:00:** Ice Cream Social and Student Research Presentations	**10:15 – 10:30:** Organizational Meeting **10:30:** **Lab Work!** (According to your group's schedule) **12:00:** Working Pizza Lunch and Student Research Presentations **1:00 – 2:00:** Dr. Kuan-Che Feng: Biomineralization

Summer Scholar Schedule of Weekly Activities

Each day starts with a mandatory group meeting at 10:15 AM!

Daily Schedule: Week of 8/4

	Monday – 8/4	Tuesday – 8/5	Wednesday – 8/6	Thursday – 8/7	Friday – 8/8
8/3: **Field Trip to BNL Summer Sunday: Fascinating Physics @ the Relativistic Heavy Ion Collider (RHIC) and Tandem Van de Graff & Llama Farm!**	**10:15 – 10:30:** Organizational Meeting **10:30:** **Lab Work!** (According to your group's schedule) **4:00:** Ice Cream Social and Student Research Presentations	**10:15 – 10:30:** Organizational Meeting **10:30 – 11:15:** Preparing for Medical School – HS and Undergrad Opportunities: Dr. Jack Fuhrer **11:15:** **Lab Work!** (According to your group's schedule) **4:00:** Ice Cream Social and Student Research Presentations	**10:15 – 10:30:** Organizational Meeting **10:30 – 11:15:** Biomineralization in Pediatric Orthopedics: Dr. Jidapa Wongcharoenwatana **11:15:** **Lab Work!** (According to your group's schedule) **4:00:** Ice Cream Social and Student Research Presentations	**10:15 – 10:30:** Organizational Meeting **10:30:** **Lab Work!** (According to your group's schedule) **7:00:** Field Trip: Escape Room! 	

GARCIA POLYMERS 2025

Please join us for the

Garcia End of Summer Research Symposium

Friday, August 8, 2024

10:00 AM-1:30 PM

Bauman Center for Leadership and Service

Welcome – Carl Lejuez

Musical arrangement – Garcia ensemble led by Prof. John Jerome

Research Presentations: Garcia Program Students

Formal Luncheon-Wing Wan of West Hempstead

Parking in lot #4 (Stony Brook Union) or Admin Garage

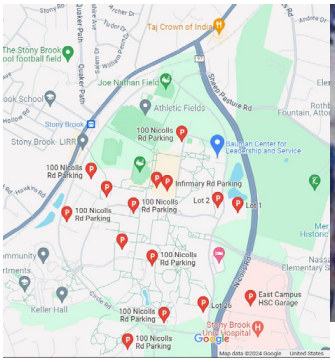

GARCIA CENTER FOR POLYMERS AT ENGINEERED INTERFACES

End-of-Summer Research Symposium

Friday, August 8 – Bauman Center for Leadership and Service

10:00 AM	***Musical Arrangement: Garcia 2025 Orchestra*** *Conducted by Prof. John Jerome*
	Welcome Dr. Carl Lejuez, Provost, Stony Brook University
10:20 AM	**Session I: Nucleotides & Proteins on Surfaces** **Chairs: Selina Zhang - Harvard University** **& Kira Klayman - Binghamton University**
1.1	Ordered DNA Fragmentation over UV-patterned SU-8 Using Tn5 Transposase **Christian Hackett** - South Side High School, Rockville Centre, New York **Alice Hu** - King Senior High School, Tampa, Florida **Cassidy Kirschenbaum** - Brookline High School, Brookline, Massachusetts **Xinyu (Tiffany) Li** - Shenzhen College of International Education, Shenzhen, Guangdong, China **Kevin Zhang** - North Hunterdon High School, Annandale, New Jersey
1.2	The Domain Specific Interactions of P12 and Albumin and their Inhibition of Fibrin Polymerization **Madeleine Gaillard** - South Side High School, Rockville Centre, New York **Ziyan (Selina) Huang** - The Winsor School, Boston, Massachusetts **Nina Pfeffer** - Stella K Abraham, Hewlett, New York **Sarah Sullivan** - Yeshiva University High School for Girls, Hollis, New York
1.3	Molecular Dynamics and Energy Calculations of P12 Peptide on a Hydrophobic, Carbon Fluoride Surface **Audrey Huang** - Woodbridge High School, Irvine, California **Katelyn Deng** - Connecting Waters Charter School East Bay, Union City, California **Connor Zhao** - North Hollywood Senior High School, North Hollywood, California **Liaoliao (Eric) Shi** - Eastside High School, Taylors, South Carolina
1.4–6	Analysis of P12 Binding Behavior to Fibrinogen Domains Through Molecular Dynamic Simulations **Katelyn Deng** - Connecting Waters Charter School East Bay, Union City, California **Audrey Huang** - Woodbridge High School, Irvine, California **Connor Zhao** - North Hollywood Senior High School, North Hollywood, California **Liaoliao (Eric) Shi** - Eastside High School, Taylors, South Carolina
10:35 AM	**Session II: Biomineralization** **Chairs: Lingjie Pan & Briman Yang - Stony Brook University**
2.1	Characterization of TRACE-Fabricated Collagen Scaffold and Application to Tissue Construction **Alexander Cheng** - Spring Branch Academic Institute, Houston, Texas **Shaun Johnet** - Archimedean Upper Conservatory, Miami, Florida **Xinying (Louis) Li** - Shenzhen Middle School, Shenzhen, China **Timur Volkov** - University of Toronto Schools, Toronto, Ontario, Canada **Anthony Zhao** - Ladue Horton Watkins High School, St. Louis, Missouri

2.2	Determining cell specific gene markers for osteoblasts and odontoblasts using scRNA seq data **Chunman Li** - Beijing World Youth Academy, Beijing, China
2.3	Effect of Static Magnetic Fields on the Proliferation and Differentiation of Dental Pulp Stem Cells Cultured In Vitro on Collagen Scaffolds **Alexander Cheng** - Spring Branch Academic Institute, Houston, Texas **Shaun Johnet** - Archimedean Upper Conservatory, Miami, Florida **Xinying (Louis) Li** - Shenzhen Middle School, Shenzhen, China **Timur Volkov** - University of Toronto Schools, Toronto, Ontario, Canada **Anthony Zhao** - Ladue Horton Watkins High School, St. Louis, Missouri
2.4	Evaluation of in-vitro CASA-induced biomineralization via stem cell differentiation **Suhrith Muvvala** - Portola High School, Irvine, California **Fangqi (Felicity) Liao** - Cushing Academy, Ashburnham, Massachusetts **Sean Lee** - Lambert High School, Suwanee, Georgia **Alyssa Wang** - East Ridge High School, Woodbury, Minnesota **Shuyan (Emily) Li** - Suzhou North America High School, Suzhou, Jiangsu, China **Ahyoung Song** - International Academy East, Troy, Michigan **Harper Falivene** - South Side High School, Rockville Center, New York **Lucas Hofflich** - Tuckahoe High School, Eastchester, New York
2.5	In Vivo Evaluation of an Innovative Injectable and Retrievable Drug Delivery System for Endodontic Therapy Using a Canine Model **Brenna Ren** - The Harker School, San Jose, California
2.6	Deep Learning-Based Segmentation of CBCT Sinus Scans for Mucosal Thickening Classification **Eun-Seo (Emily) Song** - Cornerstone Collegiate Academy of Seoul, Seoul, Republic of Korea (South Korea) **Katelyn Deng** - Connecting Waters Charter School East Bay, Union City, California
10:55 AM	**Session III: Energy Generation** **Chairs: Cosmo Perfetti & Leonard Johnson - Stony Brook University** **Jessica Bogen - Suffolk County Community College**
3.1	Improved Proton-Exchange Membrane Fuel Cell Efficiency through Integration of *Rhizobium tropici* derived Extracellular Polymeric Substance **Sarah Dabees** - Aubrey Rogers High School, Naples, Florida **Jerry Gu** - Princeton International School of Mathematics and Science, Princeton, New Jersey **Nirati Iyer** - West Windsor-Plainsboro High School South, West Windsor, New Jersey **Leo Pan-Wang** - The Peddie School, Hightstown , New Jersey **Eric Ji** - South Forsyth High School, Cumming, Georgia
3.2	Performance Enhancement of Anion Exchange Membrane Fuel Cells via ZnO Atomic Layer Deposition and Silver Nanoparticle LB Coating **Kayla Etra** - Yeshiva University High School for Girls, Queens, New York **Yixuan (Michael) He** - Shanghai Pinghe School, Shanghai, China **Xuandi (Mathieu) Wang** - BASIS International School Hangzhou, Hangzhou, China **Hanyuan Yang** - Shanghai World Foreign Language Academy, Shanghai, China

3.3	Cost-Effective Thiol-Capped Copper Nanoparticle Surface Engineering for Enhanced Durability and Performance in Proton Exchange Membrane Fuel Cells **Eric Ji** - South Forsyth High School, Cumming, Georgia **Ian Kim** - Hicksville High School, Hicksville, New York **Sze Tin (Kitty) Lai** - Milton Academy, Milton, Massachusetts
3.4	High-Throughput DFT Modeling of Graphite-Dimethoxyethane and Platinum-Water Interfaces for Energy Applications **Jasper Stackawitz** - Pennsbury High School, Fairless Hills, Pennsylvania **George Mirgorodskiy** - The Loomis Chaffee School, Windsor, Connecticut **Maggie Li** - Jericho High School, Jericho, New York
11:10 AM	**Session IV: Computational Methodology** **Chairs: Bernard Essuman, Jashmin Gill, & Fiona Chen - Stony Brook University**
4.1	Leveraging a Large Language Model to Build Structured Electrolyte Databases for Multicomponent Property Prediction **Ray Zhang** - St. George's School, Vancouver, Canada **Jing-Xiang (Albert) Huang** - Saigon South International School, Ho Chi Minh City, Vietnam **Yuanxi (Cici) Yao** - Shenzhen Middle School, Shenzhen, China
4.2	Adaptive-Balance Active Learning for Neural Operators **Aiden Kwon** - Palos Verdes Peninsula High School, Rolling Hills Estates, California
4.3	Fourier-Denoising for Noisy Hamiltonian Systems: Enhancing Symplectic Dynamics Learning **Chloe Ho** - Basis Independent Silicon Valley, San Jose, California
4.4	Seasonal-Trend-Noise Decomposition via Frequency Band Splitting **Andy Jiang** - Stuyvesant High School, Manhattan, New York **Yanguo (Spark) Zhao** - BASIS International School Guangzhou, Guangzhou, China
4.5	Using Velocity-Inferred Hamiltonian Networks: Symplectic Dynamics from Position-Only Observations **Claire Yu** - Germantown Friends School, Philadelphia, Pennsylvania
4.6	The Effect of Temperature on the Binding Dynamics Between the SARS-CoV-2 Spike Glycoprotein and Polylactic Acid Surface **Audrey Huang** - Woodbridge High School, Irvine, California
11:25 AM	**Session V: Biopolymers** **Chairs: Damien Crowley - Stanford University** **Samuel Sylvia, & Laila Juma - Stony Brook University**
5.1	Mechanisms of Soil-Strengthening for Polyelectrolyte Nanocomposite Gels **Nathaniel Gao** - Lower Merion High School, Ardmore, Pennsylvania **Benson Chou** - Great Neck South High School, Great Neck, New York **Max Xu** - Enloe Magnet High School, Raleigh, North Carolina **Daniel Zhou** - Skyline High School, Ann Arbor, Michigan

5.2	Characterization of the Metal Absorption Capability of Rhizobium Tropici-Produced Exopolysaccharide **Alli Katila-Miikkulainen** - Palo Alto High School, Palo Alto, California **Caleb Son** - Mount Hebron High School, Ellicott City, Maryland **Talon Xing** - North Allegheny Senior High School, Wexford, Pennsylvania **Ian Zhang** - Martin Luther King High School, Riverside, California
5.3	Evaluation of the Structural and Electrochemical Properties of Extracellular Polymeric Substance Derived from *Rhizobium tropici* **Sarah Dabees** - Aubrey Rogers High School, Naples, Florida
5.4	Impact of Rhizobium Tropici-Produced Biopolymer on the pH of Acidic and Basic Solutions **Lingfei (Angel) Zhu** - Shenzhen Middle School, Shenzhen, Guangdong Province, China **Chujia (Susie) Yang** - Sendelta International Academy, Shenzhen, China
5.5	Rhizobium Tropici-Produced Biopolymer Impact on Water Evaporation and Sublimation **Christian Chan** - South Side High School, Rockville Centre, New York **Ella Li** - Lexington High School, Lexington, Massachusetts
5.6	Stabilization of Silty Sand Using Xanthan Gum, Locust Bean Gum, and Rhizobium Tropici Biopolymer **Evan Liu** - Lynbrook High School, San Jose, California
11:45 AM	**Session VI: Brain Aneurysm Models** **Chairs: Sahana Dhama - Cornell University** **& Sam Specht - Duke University**
6.1	Engineering UV-crosslinked Poly(vinyl alcohol)-based Vascular Graft and Brain Aneurysm Models **Rachel Lee** - Palos Verdes Peninsula High School, Rolling Hills Estates, California
6.2	Optimizing Mechanical Properties of Pluronic Hydrogel Blends for Study of Brain Aneurysms **Chetas Aduri** - Ames High School, Ames, Iowa **Joshua Feigenbaum** - South Side High School, Rockville Centre, New York **Rosalie Liu** - Westview High School, Portland, Oregon **Aaratrika Mondal** - Wayzata High School , Plymouth, Minnesota **Yeji Son** - American School of Guatemala, Guatemala City, Guatemala **Alessandro Verona** - American School of Milan, Milan, Italy **Wenxin (Wendy) Yu** - Guangdong Country Garden School, Foshan, China
6.3	Optimizing Injection Procedure of a Pluronic Hydrogel Blend for Brain Aneurysm Treatment **Chetas Aduri** - Ames High School, Ames, Iowa **Joshua Feigenbaum** - South Side High School, Rockville Centre, New York **Rosalie Liu** - Westview High School, Portland, Oregon **Aaratrika Mondal** - Wayzata High School , Plymouth, Minnesota **Yeji Son** - American School of Guatemala, Guatemala City, Guatemala **Alessandro Verona** - American School of Milan, Milan, Italy **Wenxin (Wendy) Yu** - Guangdong Country Garden School, Foshan, China

6.4	Polymer-based Flow Diverter Systems for Endovascular Embolization **Danielle Lu** - South Side High School, Rockville Centre, New York **Juwon (Joelle) Kim** - Seoul Academy, Seoul, South Korea
6.5	Thermal Shape-Memory Polymer for Mechanical Severance of Injected Polymer in Brain Aneurysm Treatments **Kevin Qiu** - Wayzata High School, Plymouth, Minnesota **Ishmeet Singh** - Stockdale High School, Bakersfield, California **Christopher Wang** - Solon High School, Solon, Ohio **Connor Zhao** - North Hollywood Senior High School, North Hollywood, California
12:00 AM	**Session VII: Biomechanics & Biomedical Devices** **Chairs: Hugh Rosshirt - Stony Brook University** **& Amanda Salantiri - University of Connecticut**
7.1	Expression Detection from Where's Waldo Using Digital Image Speckle Correlation (DISC) **Kiara Yoon** - Palo Alto High School, Palo Alto, California **Ryan Gu** - Westwood High School, Austin, Texas **Catherine Ji** - New Trier High School, Winnetka, Illinois **Zhanhui (Lemi) Gao** - Dulwich Beijing International School, Beijing, China **Chloe Shim** - Hong Kong International School, Hong Kong, Hong Kong **Chloe Yim** - Great Neck South High School, Great Neck, New York **Yanguo (Spark) Zhao** - BASIS International School Guangzhou, Guangzhou, China
7.2	Porker Poker: Developing a Noninvasive Method to Measure Tensile Metrics Using Digital Image Speckle Correlation (DISC) **Andy Jiang** - Stuyvesant High School, Manhattan, New York **Chloe Shim** - Hong Kong International School, Hong Kong, Hong Kong **Chloe Yim** - Great Neck South High School, Great Neck, New York **Yanguo (Spark) Zhao** - BASIS International School Guangzhou, Guangzhou, China **Jerry Gu** - Princeton International School of Mathematics and Science, Princeton, New Jersey
7.3	Supercritical CO2-Mediated Decellularization of Human Dermis Samples **Zhanhui (Lemi) Gao** - Dulwich Beijing International School, Beijing, China **Ryan Gu** - Westwood High School, Austin, Texas **Catherine Ji** - New Trier High School, Winnetka, Illinois **Kiara Yoon** - Palo Alto High School, Palo Alto, California
7.4	Build and Design of a Page Turner Based on Proportional Integral Derivatives (PIDs) **Jerry Gu** - Princeton International School of Mathematics and Science, Princeton, New Jersey **Andy Jiang** - Stuyvesant High School, Manhattan, New York **Yanguo (Spark) Zhao** - BASIS International School Guangzhou, Guangzhou, China **Chujia (Susie) Yang** - Sendelta International Academy, Shenzhen, China
7.5	Reverse Thermo-Responsive Polymer-Based Systems for Bioadhesive Applications **Ke (Cleo) Xu** - Phillips Academy Andover, Andover, Massachusetts

7.6	Spreadable Poly(tetramethylene ether)glycol/Poly(ε-caprolactone)-Based Crosslinkable Polymer for Biomedical Applications **Yicheng (Ken) Zhang** - The High School Affiliated to Renmin University of China, Beijing, China **Xuehan Fan** - The Experimental High School Attached to Beijing Normal University, Beijing, China **Mengdi (Oscar) Xie** - The Experimental High School Attached to Beijing Normal University, Beijing, China
12:20 PM	**Session VIII: PLA-Based Blends & Composites** **Chairs: Phoebe Zheng & Tabarjah Neal - Stony Brook University**
8.1	Eco-friendly Phosphorus-Based Flame Retardant Formulations for Wildfire Prevention in Vegetation **Ishita Bafna** - William G. Enloe High School, Raleigh, North Carolina **Emily Do** - The Brearley School, New York, New York **Danica Stout** - Montclair High School, Montclair, New Jersey
8.2	Development of Graphene-Enhanced Biodegradable Polymer Nanocomposites for Conductive Applications **Alli Katila-Miikkulainen** - Palo Alto High School, Palo Alto, California **Caleb Son** - Mount Hebron High School, Ellicott City, Maryland **Talon Xing** - North Allegheny Senior High School, Wexford, Pennsylvania **Ian Zhang** - Martin Luther King High School, Riverside, California
8.3	Unraveling the morphology of PS/PLA homopolymer blends by planar-substrate model system **Eric Lin** - Adlai E. Stevenson High School, Lincolnshire, Illinois **Brenna Ren** - The Harker School, San Jose, California **Kaden Ren** - Martin Luther King High School, Riverside, California
8.4	Local morphological changes of PS/PLA blends in Si substrate based thin films **Eric Lin** - Adlai E. Stevenson High School, Lincolnshire, Illinois **Brenna Ren** - The Harker School, San Jose, California **Kaden Ren** - Martin Luther King High School, Riverside, California
12:35 PM	**Session IX: Nanoparticles for Catalysis & Enzymatic Reactions** **Chairs: Bandari Chen - Stony Brook University** **& Krystal Lazo - Suffolk County Community College**
9.1	Comparing the Properties of GO, pRGO, and Metallized pRGO **Diana Sun** - Jericho High School, Jericho, NY **Julianne Mayetani** - Palos Verdes Peninsula High School, Rolling Hills Estates, California **Shawn Lim** - Syosset High School, Syosset, New York **Leon Zhou** - Rye Country Day School, Rye, New York

9.2	A Novel Approach of Developing Metal Oxide + hBN/BNNT Nanocatalysts: Fundamental Studies of BN Materials and Support Effect on TMO_x **Krish Patel** - The Academy for Mathematics, Science, & Engineering (Morris County), Rockaway, New Jersey
9.3	Characterization of the Freezing and Melting Behavior of Lithium Chloride Aqueous Solutions **Andrew Wang** - Riverdale Country School, Bronx, New York **Juwon (Joelle) Kim** - Seoul Academy, Seoul, South Korea
12:45 PM	**Session X: TiO2 Nanoparticles** **Chair: Martin Liu - University of Washington**
10.1	Quantifying TiO2 Nanoparticle Uptake and Its Effects on Proliferation of Human Endothelial Cells and Fibroblasts **Ahyoung Song** - International Academy East, Troy, Michigan **Chunman Li** - Beijing World Youth Academy, Beijing, China **Emily Segall** - Yeshiva University High School for Girls, Queens, New York **Charlotte Huang** - William Tresper Clarke High School, Westbury, New York **Suhrith Muvvala** - Portola High School, Irvine, California **Fangqi (Felicity) Liao** - Cushing Academy, Ashburnham, Massachusetts **Alyssa Wang** - East Ridge High School, Woodbury, Minnesota **Shuyan (Emily) Li** - Suzhou North America High School, Suzhou, Jiangsu, China **Sean Lee** - Lambert High School, Suwanee, Georgia **Lucas Hofflich** - Tuckahoe High School, Eastchester, New York **Harper Falivene** - South Side High School, Rockville Center, New York
10.2	Decoding the Crosstalk: Computational Analysis of TiO2 Exposure and Its Overlap with Alzheimer's and Osteoporotic Signaling **Xinying (Louis) Li** - Shenzhen Middle School, Shenzhen, China
12:50 PM	**Session XI: Journal of Ethics in Scientific and Technological Innovations (JESTI)** **Chair: Kevin Zhang – North Hunterdon High School**
1:00 PM	*Gala Luncheon provided by Wing Wan of West Hempstead*

We gratefully acknowledge the support of the Louis Morin Charitable Trust

Session I: Nucleotides and Proteins on Surfaces

Chairs:

Christian Saby, Adam Hansen, Nabila Jaman Tripti, Bernard Essuman

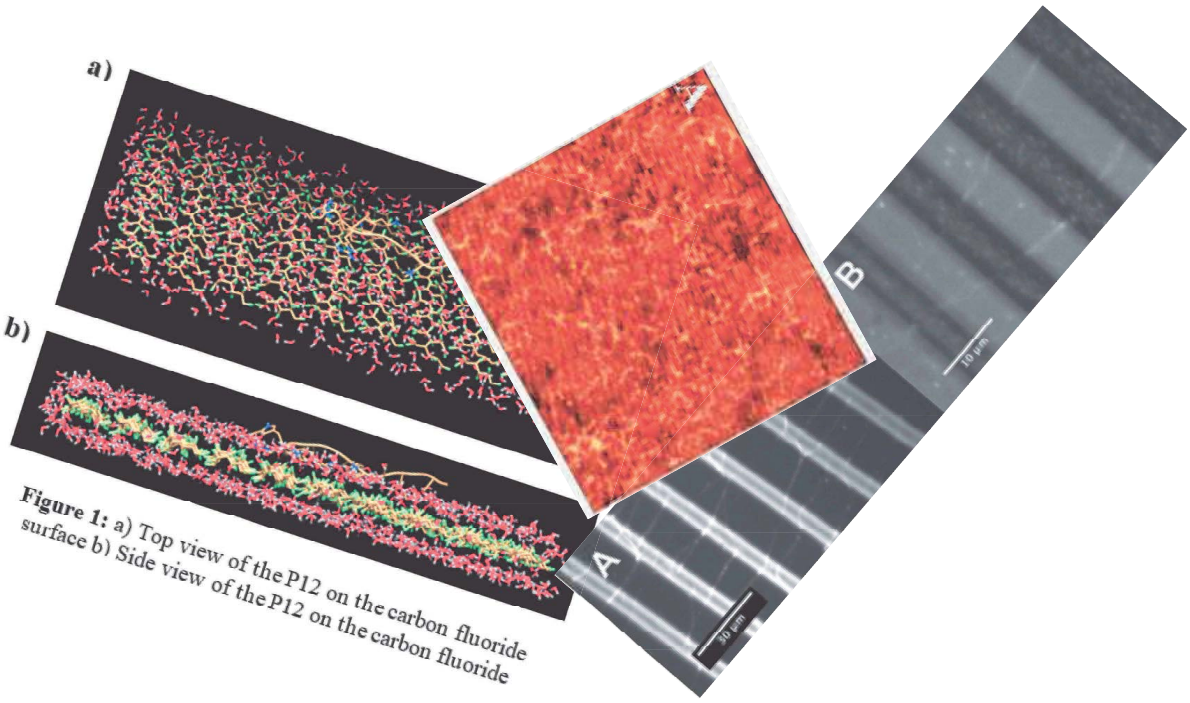

Figure 1: a) Top view of the P12 on the carbon fluoride surface b) Side view of the P12 on the carbon fluoride

Ordered DNA Fragmentation over UV-patterned SU-8 Using Tn5 Transposase

Christian Hackett[1 †], Alice Hu[2 †], Cassidy Kirschenbaum[3 †], Tiffany Li[4 †], Kevin Zhang[5 †], Selina Zhang[6 †], Christian Saby[7], Jonathan Sokolov[7], Miriam Rafailovich[7]

† Authors contributed equally to this work

[1]South Side High School, NY, 11570, [2]King High School, FL, 33647, [3]Brookline High School, MA, 02445, [4]Shenzhen College of International Education, Shenzhen, China, [5]North Hunterdon High School, NJ, 08801, [6]Harvard University, MA, 02138, [7]Stony Brook University, NY, 11794

DNA sequencing is increasingly required for wide applications in medicine, forensics, biology, etc., with a need to sequence large quantities of DNA. Current mainstream methods include Next Generation Sequencing and Whole Genomic Sequencing. Strands must first be fragmented before sequencing and then reassembled via computational means. However, without a complete genome sequence, reconstruction may form chimeric sequences and fragmented contigs. Therefore, either a significant sample of DNA must be present, or the sample must be amplified, which costs resources and incurs replicational error. Ordered DNA fragmentation would mitigate both concerns by preserving sequence.

In our work, we examined the viability of patterning a thin film composed of SU-8. The SU-8 based photoresist SQ2 (film thickness of 2 μm) was selected as the preferred substrate for its negative photoresist properties—enabling rapid crosslinking when exposed to UV light—as well as its consistency and lithographic reproductivity, both of which are required for microfluidic applications. KemLab's SQ2 was spuncast onto 5.5 mm x 20 mm silicon wafer slivers using KemLab's recommended program [1]. Silicon wafers with SQ2 coating were positioned over a soda-lime glass photomask and exposed to a 365 nm LED (10-15mW output) from a distance of 3 inches, creating a striped pattern of varying widths. UV exposure time of 3 minutes yielded successful patterning.

E. coli transposase Tn5 was utilized for its artificially modified 19-base pair recognition site for DNA binding and cleaving. Its specific binding allows for the attachment of unique barcodes and labels, such as PCR handles, to DNA. These molecular flags in turn can indicate the spatial origin and order, which is essential for accurate post-sequencing genome assembly [2]. Patterned SQ2 wafers were dipped in mouse DNA solution and then developed in propylene glycol methyl ether acetate for 1 minute, leaving DNA suspended across any patterned regions to reduce steric hindrance. The DNA solution was composed of 5 μL Novagen mouse DNA solution (1 mg/mL), 5 μL of 10x diluted SYBR Gold dye (1.24 mM [3]), and 1390 μL DNase reaction buffer (NEB). Droplets of 3 μL of 5.26% loaded Diagenode Tn5 transposase solution (prepared using 4 μL 2 mg/mL Tn5, 36 μL 2x tagmentation buffer, and 36 μL water) were deposited onto samples. The samples were heated at 55°C for 7 minutes (in a low-volume space so as to prevent evaporation) to initiate DNA cleaving. Tn5 was finally digested for 20 minutes in 15 μL Proteinase K solution diluted in 985 μL of DNase buffer. Fluorescence microscopy was employed to gauge the efficacy of Tn5 cutting and Proteinase K digestion.

Overall, tests demonstrated successful DNA bridging, particularly over gaps less than 20 μm, with moderate efficiency of DNA fragmentation. Our studies show that 5.26% Tn5 concentrations proved to be effective for DNA cutting (Fig. 1B). Initial experiments with positive photoresist polymethyl methacrylate have shown some promise, suggesting that further investigation is warranted. Future directions of work also include optimizing Tn5 scission of the DNA and proteinase (or SDS) digestion of the Tn5 as well as selective removal of the DNA.

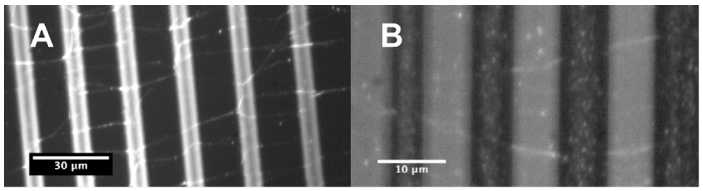

Figure 1. Leica confocal microscope imaging.
A) Mouse DNA stretched over 3-minute UV-patterned SQ2.
B) Sample from A) after Tn5 and Proteinase K treatment; mouse DNA is cut.

[1] KemLab. (2021). *HARE SQ™*. https://www.kemlab.com/_files/ugd/5b8579_2d82cd4d3986446fb7d22ce6f1be67c9.pdf

[2] Li, N., Jin, K., Bai, Y., Fu, H., Liu, L., & Liu, B. (2020). Tn5 Transposase Applied in Genomics Research.*International journal of molecular sciences, 21*(21), 8329. https://doi.org/10.3390/ijms21218329

[3] Kolbeck, P.J., Vanderlinden, W., Gemmecker, G., Gebhardt, C., Lehmann, M., Lak, A., Nicolaus, T., Cordes, T., & Lipfert, J. (2021). Molecular structure, DNA binding mode, photophysical properties and recommendations for use of SYBR Gold.*Nucleic Acids Research, 49*(9), 5143-5158. https://doi.org/10.1093/nar/gkab265

The Domain Specific Interactions of P12 and Albumin and their Inhibition of Fibrin Polymerization

Madeleine Gaillard[1], Selina Huang[2], Kira Klayman[3], Nina Pfeffer[4], Sarah Sullivan[5] , Adam Hansen[6], Miriam Rafailovich[6]

[1]South Side High School, NY, 11570, [2]The Winsor School, MA, 02215 [3] Binghamton University, NY, 13902, [4]Stella K. Abraham High School For Girls, NY, 11557, [5]Yeshiva University High School for Girls, NY, 11423, [6]Department of Materials Science and Chemical Engineering, Stony Brook University, NY, 11794

Fibrinogen, a 340 kDa glycoprotein, composed of two sets of three polypeptide chains, plays a key role in clot formation. Upon tissue damage, the coagulation cascade is triggered, leading the thrombin to cleave fibrinogen into fibrin by removing N-terminal fibrinopeptides[1]. This fibrin polymerizes into fibers that form a clot mesh and support platelet aggregation. On hydrophobic surfaces, fibrinogen exposes its αC domains, leading to fiber formation[2]. The compound P12 inhibits this process by reducing fibrin polymerization, significantly lowering thrombogenicity on materials like polystyrene. Therefore, studying the domain specific interactions between fibrinogen, P12, and albumin is important for analyzing their antithrombogenic properties.

This study investigates the effects of the P12 peptide — a fibronectin-derived sequence — on fiber formation, with particular attention to its interaction with specific fibrinogen domains. We assessed how varying concentrations of P12 and albumin affect fibrin polymerization and fibrinogen interactions on surfaces. Fibrinogen was pipetted onto spin-coated polystyrene silicon wafers and analyzed via atomic force microscopy (AFM) and confocal microscopy. Variants of fibrinogen lacking the C-terminal of the αC domain and the N-terminal of the αC domain were used to explore domain-specific effects. Red-stained fibrinogen and green-stained albumin were applied to investigate their relationship. In addition, different antibodies were added to attach to the specific regions of the αC domain. The influence of P12 on fibrin polymerization was assessed across varying concentrations of P12.

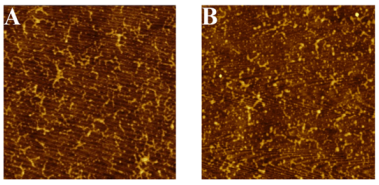

Figure 1:AFM images of Fibrinogen on Polystyrene Surface without P12 (A) and with P12 (B)

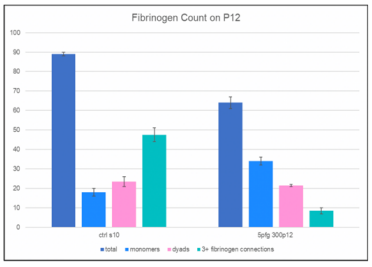

Figure 2: Difference in fibrinogen connections between control sample and P12 sample

When analyzing the images of the P12 wafers on the AFM, as P12 concentration increased with a minimum dependence of 1μM, fibers ceased to form on the surface. In the control sample (Figure 1A) there are many long, complex fibrinogen networks that are formed and in the 300 nM P12 sample (Figure 1B) there are few interactions between neighboring molecules on the surface fibers due to the inhibition of polymerization caused by P12. The total number of fibrinogen counted as well as the number of fibrinogen with more than three connections was much higher in the control sample compared to the P12 sample (Figure 2). When studying the domain specific interactions of the P12 and albumin, we found using confocal microscopy and AFM that they likely bind to the αC domain. Using fibrinogen lacking the N-Terminal of the des-αc region and fibrinogen that was lacking the C-terminal of the des-αc region we found that P12 and albumin may bind specifically to the αC domain and likely the N-terminal. This demonstrates P12's potential as an antithrombotic agent and provides insights into fibrinogen structure-function relationships and the domain specific interactions between P12, albumin and fibrinogen.

[1] Kattula, S., Byrnes, J. R., & Wolberg, A. S. (2017). Fibrinogen and Fibrin in Hemostasis and Thrombosis. Arteriosclerosis, thrombosis, and vascular biology, 37(3), e13–e21. https://doi.org/10.1161/ATVBAHA.117.308564

[2] Zhang, Liudi, et al. "The Influence of Surface Chemistry on Adsorbed Fibrinogen Conformation, Orientation, Fiber Formation and Platelet Adhesion." *Acta Biomaterialia*, vol. 54, Mar. 2017, pp. 164–74, doi:10.1016/j.actbio.2017.03.002.

Analysis of P12 Binding Behavior at the Central E Domain of Fibrinogen Through Molecular Dynamic Simulations

Katelyn Deng[1], Audrey Huang[2], Connor Zhao[3], Liaoliao Shi[4], Nabila Jaman Tripti[5], Bernard Essuman[5], Yuefan Deng[5], Miriam Rafailovich[6]

[1]Connecting Waters Charter School East Bay, Union City, CA 94587, [2]Woodbridge High School, Irvine, CA, 92604, [3]North Hollywood High School, North Hollywood, CA, 91601, [4]Eastside High School, Taylors, SC, 29687, [5]Department of Applied Mathematics and Statistics, Stony Brook University, Stony Brook, NY 11794, [6]Department of Materials Science and Chemical Engineering, Stony Brook University, Stony Brook, NY 11790

While blood clotting is essential for preventing blood loss after injury, unintended thrombin-activated formation of fibrin on abnormal surfaces can cause life-threatening conditions like thrombosis or stroke. P12, a 14-residue peptide derived from fibronectin, has been proposed to inhibit clotting by binding to key fibrinogen regions. We evaluate its potential to disrupt early fibrin polymerization by targeting the E domain. The E domain is located in the center of fibrinogen, where it holds the N-terminal regions of all three polypeptide chains (Aα, Bß, and γ)[1]. It initiates fibrin polymerization by exposing binding sites that drive end-to-middle (D:E) interactions, which are essential for protofibril formation, and establishing the structural foundation of the blood clot[2].

Initial P12 conformations were generated through five independent 10 ns molecular dynamics (MD) simulations in explicit solvent in order to capture peptide structure variability. From these simulations, we selected seven centroid clusters to dock onto the fibrinogen E domain using the docking tool ClusPro. The highest-scoring binding pose was chosen through principal component analysis (PCA).

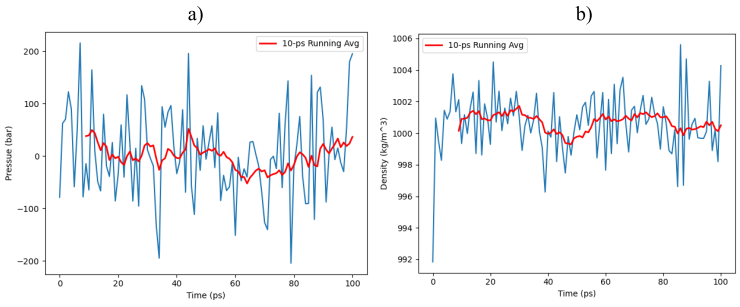

Figure 1: equilibration monitoring of the P12-E domain system. a) pressure of the system over 100 ps of NPT equilibration. The red line indicates a 10-ps running average for smoother visualization. b) density of the system over the same time frame.

The top-ranked E domain-P12 complex was then prepared for full molecular dynamics simulation using GROMACS with the CHARMM27 force field and TIP3P water model. The system was placed in a rhombic dodecahedron box with a 1.0 nm buffer, solvated, and neutralized with Na^+ and Cl^- ions. After energy minimization using the steepest descents algorithm, the system underwent sequential NVT (constant volume) and NPT (constant pressure) equilibration to ensure thermodynamic stability, as shown in Figure 1. Production MD was run for 100 ns using GPU acceleration on the SeaWulf high-performance computing cluster. Simulation outputs were recentered and custom index files were generated to isolate energy groups for the E domain and P12. Binding free energy calculations were performed using gmx_MMPBSA, allowing quantification of the interaction strength and stability throughout the trajectory. Our future work includes comparing unbinding behavior across different fibrinogen domains to better understand domain-specific interaction strengths.

[1]Mosesson, M. W., Siebenlist, K. R., & Meh, D. A. (2006). The Structure and Biological Features of Fibrinogen and Fibrin. Annals of the New York Academy of Sciences, 936(1), 11–30. https://doi.org/10.1111/j.1749-6632.2001.tb03491.x

[2]Mosesson, M. W. “Fibrinogen and Fibrin Structure and Functions.” Journal of Thrombosis and Haemostasis, vol. 3, no. 8, Aug. 2005, pp. 1894–1904, https://doi.org/10.1111/j.1538-7836.2005.01365.x.

Characterizing P12 Binding Dynamics to N-Terminal of αC Domain of Fibrinogen

Audrey Huang[1], Katelyn Deng[2], Connor Zhao[3], Liaoliao Shi[4], Nabila Jaman Tripti[5], Bernard Essuman[5], Yuefan Deng[5], Miriam Rafailovich[6]

[1]Woodbridge High School, Irvine, CA, 92604, [2]Connecting Waters Charter School East Bay, Union City, CA 94587, [3]North Hollywood High School, North Hollywood, CA, 91601, [4]Eastside High School, Taylors, SC 29687, [5]Department of Applied Mathematics and Statistics, Stony Brook University, Stony Brook, NY 11794, [6]Department of Materials Science and Chemical Engineering, Stony Brook University, Stony Brook, NY 11790

Fibrinogen plays a key role in the blood clotting process, with thrombin-mediated conversion of fibrinogen into fibrin fibers stabilizing the clots. The αC domain of fibrinogen is a critical part of this process, enhancing the lateral aggregation phase of clotting, producing thicker fibers with larger pores and determining key parts of the clot's mechanical properties, such as stiffness and deformation[1]. While essential, fibrinogen can also lead to clotting on undesirable surfaces, triggering pathological thrombosis. To prevent this abnormal clot formation, we investigate P12, a 14-residue peptide that could inhibit fibrinogen. We focus on P12's interactions with the αC domain, specifically the N-terminal.

A combination of molecular modeling and simulation tools (GROMACS, UCSF Chimera, ClusPro, Geo Energy Analyzer, SeaWulf, gmx_MMPBSA) were employed. Five independent 10 ns MD simulations were run in explicit solvent, and the resulting conformers were clustered into seven centroids. Each centroid was docked to the N-terminal of the αC domain using ClusPro, a software for protein-protein docking. Spheres were then generated on the surface of the fibrinogen, based on the features of its topology (e.g., binding pockets, cavities), and the poses from the docking were evaluated using principal component analysis (PCA), with the first principal component (PC1), which included metrics such as the fraction of atoms buried, the mean depth of the buried atoms, and hydrophobicity, and the second principal component (PC2), which included other metrics. A plot was generated (Figure 1), and the top three poses were chosen by PC1 value. The centroids of all poses were then plotted, and we found that the majority of the P12 poses preferred the biologically important part of the N-terminal (Figure 2). In particular, all three of the top poses bind to the Aα425-503 fragment of the N-terminal.

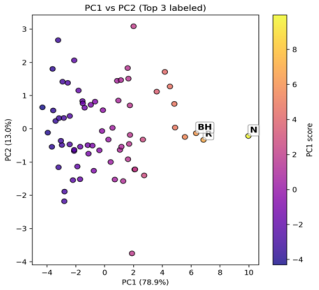

Figure 1: PCA analysis plot. Top three P12 poses for N-terminal are labeled.

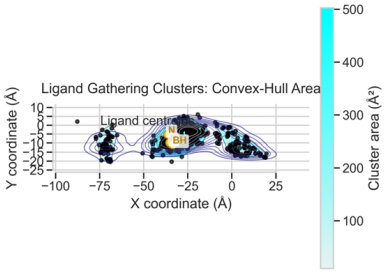

Figure 2: Centroids of P12 poses on N-terminal. Top three poses are labeled.

The single top pose was chosen and combined with the N-terminal to form a complex. A rhombic dodecahedron unit cell was defined and solvated, one chlorine ion was added to neutralize the charge of the system, and energy minimization and NVT and NPT equilibration were conducted on SeaWulf, the HPC cluster. The production MD was run and analyzed using gmx_MMPBSA[2] for binding free energy calculations.

We identified P12's top pose on the N-terminal of the αC domain of fibrinogen and investigated the binding dynamics of the pose. We will conduct steered MD simulations next, applying external forces to P12 to see how quickly it disengages.

[1]Collet, J.-P., Moen, J. L., Veklich, Y. I., Gorkun, O. V., Lord, S. T., Montalescot, G., & Weisel, J. W. (2005). The αC domains of fibrinogen affect the structure of the fibrin clot, its physical properties, and its susceptibility to fibrinolysis. *Blood, 106*(12), 3824–3830. https://doi.org/10.1182/blood-2005-05-2150

[2]Valdés-Tresanco, M. S., Valdés-Tresanco, M. E., Valiente, P. A., & Moreno, E. (2021). gmx_MMPBSA: A New Tool to Perform End-State Free Energy Calculations with GROMACS. *Journal of Chemical Theory and Computation, 17*(10), 6281–6291. https://doi.org/10.1021/acs.jctc.1c00645

Computational Analysis of P12 Peptide Binding to D-Domain of Fibrinogen

Connor Zhao[1], Liaoliao Shi[2], Audrey Huang[3], Katelyn Deng[4], Nabila Jaman Tripti[5], Bernard Essuman[5], Yuefan Deng[5], Miriam Rafailovich[6]

[1]North Hollywood High School, North Hollywood, CA, 91601, [2]Eastside High School, Taylors, SC 29687, [3]Woodbridge High School, Irvine, CA, 92604, [4]Connecting Waters Charter School East Bay, Union City, CA 94587, [5]Department of Applied Mathematics and Statistics, Stony Brook University, Stony Brook, NY 11794, [6]Department of Materials Science and Chemical Engineering, Stony Brook University, Stony Brook, NY 11790

Excessive blood clotting on undesirable surfaces can lead to life-threatening conditions such as stroke and thrombosis; however, inhibiting fibrinogen interactions with P12, a short, 14-residue peptide derived from the clotting protein fibronectin, offers a promising strategy to prevent unusual clot formation. Blood clotting occurs in two phases: primary hemostasis, in which platelets activate and aggregate into a weak clot, and secondary hemostasis, in which a coagulation cascade leads to thrombin-activated formation of fibrin fibers from fibrinogen monomers to stabilize the clot[1]. Specifically, γ-nodules of the D domain interact with uncovered "knobs" of the N-terminal in knob-hole interactions[2]. Additionally, fibrinogen aggregates laterally through covalent and intermolecular interactions between adjacent D domains. This fiber-forming process sometimes results in excessive clotting, which P12 may be able to prevent.

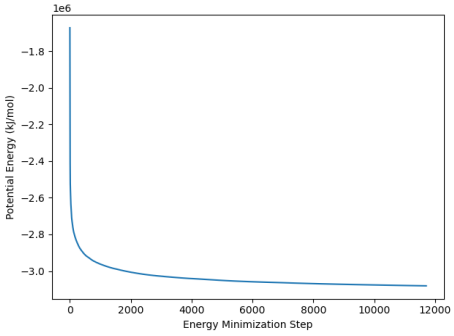

Figure 1: The energy of the system converges to a minimum iteratively during energy minimization

First, molecular dynamics (MD) simulations in GROMACS were run to generate seven conformations of P12. Next, each one of these were docked with the D-domain using ClusPro, generating numerous poses. A new structure for MD simulations was then constructed by combining the top pose from PCA and the D-domain. Based on this structure, a 100 ns MD simulation was performed in a rhombic dodecahedron unit cell in GROMACS. The system was then solvated and the charge was neutralized by additional ions. Next, energy minimization was conducted to remove any steric or geometric clashes (Figure 1). The solvent was then equilibrated around the protein under a NVT ensemble with a position restraining force (Figure 2), followed by NPT equilibration conducted to stabilize the density. Next, the MD simulation was conducted on SeaWulf and the resulting structure was indexed and the free energy was calculated with gmx_MMPBSA.

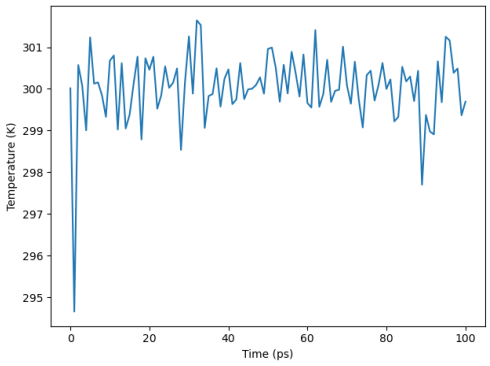

Figure 2: The temperature of the system oscillates around the target value of 300K during the NVT equilibration

In this project, the interaction between the D-domain and the P12 protein was characterized through molecular docking and MD simulations. The top poses identified so far will continue to be analyzed through quantum mechanics computations to improve energy calculations and steered MD simulations that test energy profiles through applied forces.

[1]Wiesel, J.W., & Litvinov, R. L. (2013). Mechanisms of fibrin polymerization and clinical implications. *Blood, 121*(10), 1712-1719. doi: https://doi.org/10.1182/blood-2012-09-306639

[2]Wolberg, A. S. (2023). Fibrinogen and fibrin: synthesis, structure, and function in health and disease. *Journal of Thrombosis and Haemostasis, 21*(11), 3005–3015. https://doi.org/10.1016/j.jtha.2023.08.014

Molecular Dynamics and Energy Calculations of P12 Peptide on a Hydrophobic, Carbon Fluoride Surface

Audrey Huang[1], Katelyn Deng[2], Connor Zhao[3], Liaoliao Shi[4], Nabila Jaman Tripti[5], Bernard Essuman[5], Yuefan Deng[5], Miriam Rafailovich[6]

[1]Woodbridge High School, Irvine, CA, 92604, [2]Connecting Waters Charter School East Bay, Union City, CA 94587, [3]North Hollywood High School, North Hollywood, CA, 91601, [4]Eastside High School, Taylors, SC 29687, [5]Department of Applied Mathematics and Statistics, Stony Brook University, Stony Brook, NY 11794, [6]Department of Materials Science and Chemical Engineering, Stony Brook University, Stony Brook, NY 11790

P12 is a short, 14-residue protein that has been found to reduce fibrin fiber formation on surfaces, such as polystyrene[1], lowering the risk of thrombus formation and thus strokes and pulmonary embolisms. In particular, *in vivo*, P12 has shown a preference for hydrophobic regions of fibrinogen, but the details behind this affinity remain unknown. We aim to explore P12's interactions with hydrophobic surfaces to investigate whether these regions in fibrinogen possess additional unique properties that P12 prefers, or whether this preference is driven by hydrophobicity alone.

We created the surface by building a linear six-carbon fluorinated hydrocarbon chain with terminal hydrogen atoms ([H]C(F)C(F)C(F)C(F)C(F)C(F)[H]). This chain was duplicated using GROMACS and CHARMM-GUI parameters and tiled into a larger crystalline slab, which served as the surface for placing and simulating the behavior of the P12. The surface was highly hydrophobic because of the fluorine atoms' steric bulk and electron-withdrawing nature, and it mirrored real materials, such as poly(carbon monofluoride) and short perfluoroalkane segments. As the proper orientation of P12 is not yet known, we positioned the P12 in two different orientations ("face up" and "face down") on the slab, creating P12-surface complexes.

For each complex, a molecular dynamics (MD) simulation was set up. The CHARMM36 force field and TIP3P water model were used. A rhombic dodecahedron box was defined and solvated. To neutralize the charge of the system, four chlorine ions were added. Energy minimization and NVT and NPT equilibration were performed, followed by a 100 ns production run, with position restraints applied on the surface to keep it in place. The final structure created after the production run was visualized in Chimera (Figure 1), and the simulation trajectories were analyzed using gmx_MMPBSA for binding free energy calculations.

In this study, we investigated P12's behavior on a hydrophobic, carbon fluoride surface. We will conduct further analysis to better understand P12's affinity for the hydrophobic regions of fibrinogen, which can inform potential strategies to reduce excessive blood clot formation.

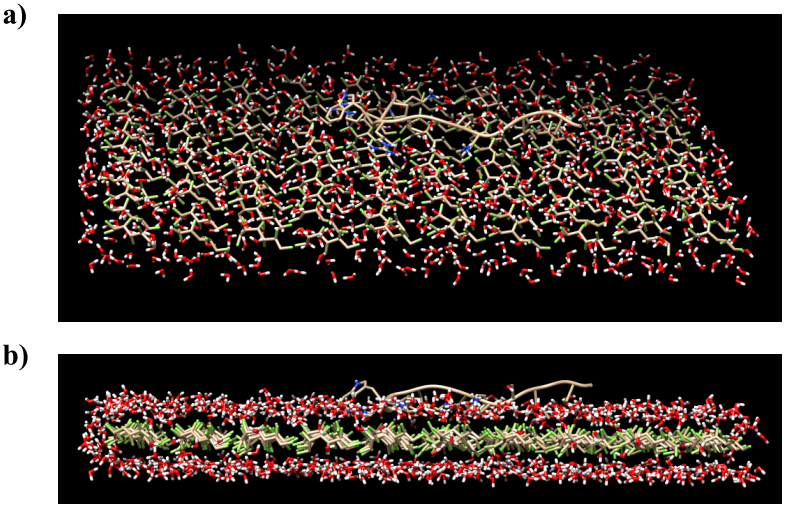

Figure 1: a) Top view of the P12 on the carbon fluoride surface b) Side view of the P12 on the carbon fluoride surface

[1]Doilidov, A., El-Saieh, S., Faria, S., & Lo, P. (2019). The Effect of P12 Peptide on Fibrinogen Fiber Formation and Endothelial Cell Attachment on Polystyrene. *Journal of Undergraduate Chemical Engineering Research, 8*, 19–23.

Session II: Biomineralization

Chairs:

Kao Li, Muyun Cui, Karin Hasegawa, Jessica Hofflich, Huiting Luo

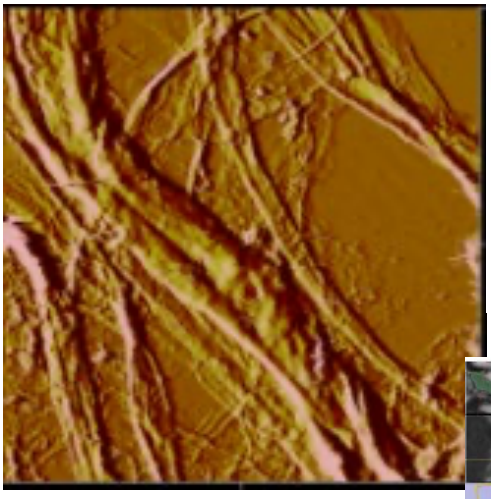

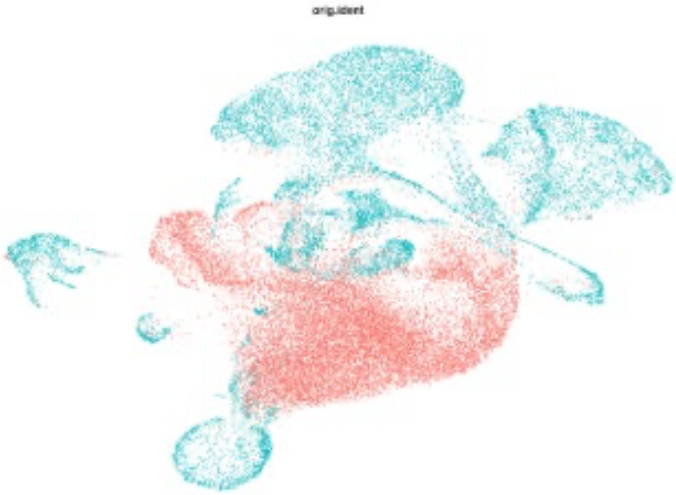

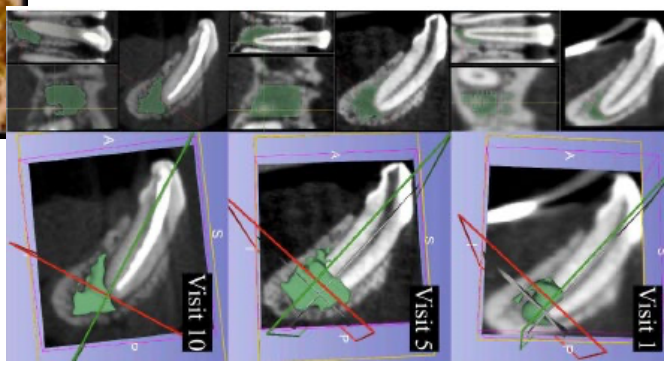

Characterization of TRACE-Fabricated Collagen Scaffold and Application to Tissue Construction

Alexander Cheng[1], Shaun Johnet[2], Xinying (Louis) Li[3], Timur Volkov[4], Anthony Zhao[5], Xiangyu Gong[6], Lingjie Pan[7], Zixie Liang[6], Kao Li[8], Huiting Luo[9], Miriam Rafailovich[9]

[1] Spring Branch Academic Institute, Houston, TX 77079, [2]Archimedean Upper Conservatory, Miami, FL 33183, [3]Shenzhen Middle School, Guangdong, China 518000, [4] University of Toronto Schools, Toronto, ON M5S 2R7 ,[5] Ladue Horton Watkins High School, Ladue, MO 63124, [6]Department of Pharmacological Sciences, Renaissance School of Medicine, Stony Brook University, Stony Brook, NY 11794, [7]Department of Chemistry, Stony Brook University, Stony Brook, NY 11794, [8]School of Biomedicine and Nursing, Shandong Institute of Petroleum and Chemical Technology, Shandong, China 257099, [9]Department of Materials Science & Engineering, Stony Brook University, Stony Brook, NY 11794, USA

Collagen, a main structural protein in the animal and human body, provides important biological and physical support for the extracellular matrix (ECM)[1]. As such, Collagen I is a key scaffolding material in tissue engineering, but challenges in controlling assembly kinetics in a biocompatible manner limits its application as a primary scaffold in biofabrication. Tunable rapid assembly of collagenous elements (TRACE), a novel method of collagen scaffold fabrication, made rapid assembly and accurate positioning of soluble collagen possible by using high concentrations of polyethylene glycol (PEG) as a crowding agent in order to form collagen bundles.[2] In this study, we investigated applications of TRACE-processed collagen in scaffold construction.

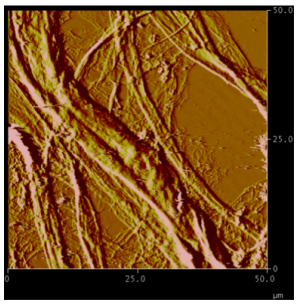

Fig 1. AFM of 8mg/ml TRACE-processed collagen bundle

Dental pulp stem cells (DPSCs) of passage 5 and Enhanced Green Fluorescent Protein (EGFP) expressing human umbilical vein endothelial cells (HUVEC) of passage 6 were cultured in collagen-coated flasks. DPSCs were seeded onto both collagen bulk gel and TRACE-processed collagen bundles, while HUVECs were seeded onto TRACE-processed collagen bundles only. For later investigation of cell differentiation, DPSCs of passage 7 were seeded on the surface of collagen scaffolds and in free-floating media three days after the first round of seeding.

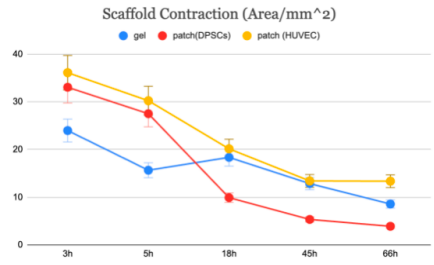

Fig 2. Scaffold Contraction Curve of Area

Scaffold characterization through light microscopy and atomic force microscopy (AFM) demonstrated that TRACE generated much thicker collagen bundles than regular methods, suggesting stronger mechanical properties (Figure 1). Conventional gelation methods yielded fibrils <1 μm in diameter, whereas TRACE-processed bundles reached up to 80 μm in width and had an approximate mean thickness of 27.15 μm. Fluorescence imaging showed that HUVEC-seeded collagen bundles maintained a normal scaffolding structure. Collagen contraction was also monitored in 66 hours after the first round of cell seeding. Continuous contraction of collagen scaffolds was observed (Figure 2). An over-contraction was observed in all collagen samples, causing a decreased amount of cells attached to collagen in the second round of DPSC seeding. To mitigate cell contraction of the collagen scaffold, we designed an iron ring-inserted collagen environment with a combination of conventional gel, TRACE-processed bundle, and fibrin. A combination of DPSCs/HUVEC and fibroblast/HUVEC would be a future option for coculture.

qRT-PCR of DPSCs will be conducted on Day 0, 14, and 28 to determine the effect of different collagen scaffolds on osteogenic differentiation. SEM will be performed on Day 28 to characterize biomineral deposition by differentiated DPSCs. Our results demonstrate that TRACE provides a viable approach to rapid collagen scaffold fabrication, which holds great promise in 3D bioprinting and bone regeneration.

[1] Dong, C., & Lv, Y. (2016). *Application of Collagen Scaffold in Tissue Engineering: Recent Advances and New Perspectives*. Polymers, 8(2), 42. https://doi.org/10.3390/polym8020042

[2]Gong, X., Wen, Z., Liang, Z., Xiao, H., Lee, S., Rossello-Martinez, A., Xing, Q., Wright, T., Nguyen, R. Y., & Mak, M. (2025). *Instant assembly of collagen for tissue engineering and bioprinting*. Nature Materials, 24(8), 1307–1318. https://doi.org/10.1038/s41563-025-02241-7

Determining cell specific gene markers for osteoblasts and odontoblasts using scRNA seq data

Chunman Li[1], Muyun Cui[2], Miriam Rafailovich[2]
[1] *Beijing World Youth Academy, Beijing,* [2] *Stony Brook University, NY, 11790*

Osteoblasts and odontoblasts play key roles in the development of bone and teeth structures. In-vitro experimentation on such cells are essential for better understanding the properties, growth, and repair of our bones and teeth for biomedical and dental applications. However, they are not easily distinguishable in in-vitro experiments where cells are differentiated and cultured. Both osteoblasts and odontoblasts are results of differentiated mesenchymal stem cells and common methods of identifying either cell type rely on their outward morphology[1] or calcium staining[2,3], which do not effectively distinguish osteoblasts and odontoblasts from other cells or from each other.

A method utilized by recent studies involves using cell specific gene markers to reliably identify cells by measuring gene expression. However, a variety of gene markers are utilized as identifiers. This report aims to evaluate the validity of established cell specific gene markers for osteoblasts and odontoblasts as well as identify new potential markers for osteoblasts and odontoblasts through analyzing preexisting single cell RNA sequencing (scRNA seq) data.

To achieve this, scRNA seq data of *Mus musculus* bone[4] and molar[5] cells from in vivo-experiments was downloaded from GEO and analyzed using the Seurat package. Data is cleaned using a standard scRNA seq preprocessing workflow. UMAPs and feature plots with respective to known markers were visualized to establish their viability in identifying osteoblast and odontoblast cell lines. Data of identified osteoblast and odontoblast cells were also combined to find identifying markers that differentiated them.

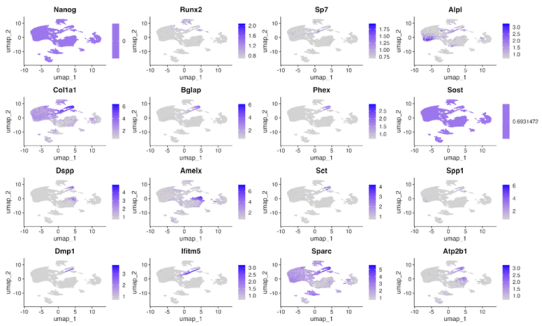

Figure 1: Feature plots of marker genes in teeth cells

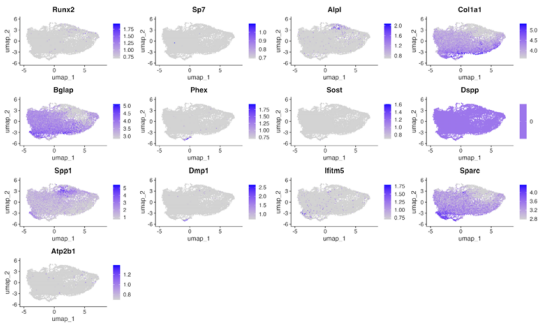

Figure 2: Feature plots of marker genes in bone cells

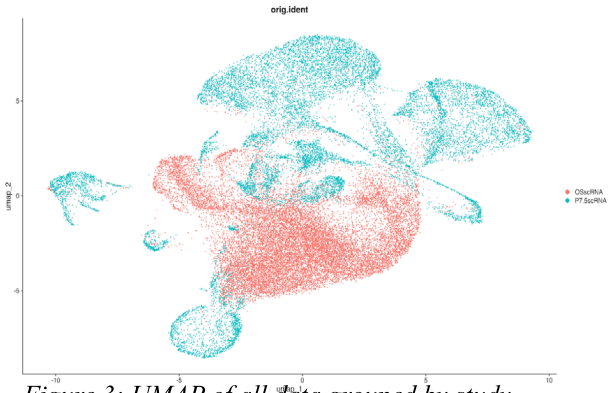

Figure 3: UMAP of all data grouped by study

Observing feature plots of known markers in osteogenic and odonto-genic cells (Figures 1, 2), certain markers seem to be effective in identifying odontoblasts out from other molar cells: *Bglap, Phex, Dmp1, Ifitm5* resulting in the clustering nature of expression within the UMAPs. *Dspp* and *Amelx* appear to be odontoblast specific markers as they are not expressed in any osteogenic cells. However, they are not consistently expressed across the cells. Extracting identifying gene markers separating the two sets of data (Figure 3) revealed *Bglap* and *Spp1* among other genes as top markers highly expressed in only osteogenic cells.

[1]*Inoue, Miho et al. "In vitro response of osteoblast-like and odontoblast-like cells to unsubstituted and substituted apatites." Journal of biomedical materials research. Part A vol. 70,4 (2004): 585-93. doi:10.1002/jbm.a.30116*
[2]Akisaka, T et al. "Ultracytochemical investigation of calcium-activated adenosine triphosphatase (Ca++-ATPase) in chick tibia."*Journal of bone and mineral research : the official journal of the American Society for Bone and Mineral Research*vol. 3,1 (1988): 19-25. doi:10.1002/jbmr.5650030105[3]Mizumachi, Hiroyuki et al. "Calcium-sensing receptor-ERK signaling promotes odontoblastic differentiation of human dental pulp cells." *Bone* vol. 101 (2017): 191-201. doi:10.1016/j.bone.2017.05.012
[4]*Wang, Jialiang S., et al. "Control of Osteocyte Dendrite Formation by Sp7 and Its Target Gene Osteocrin. Nature Communications, vol. 12, no. 1, 1 Nov. 2021, p. 6271, www.nature.com/articles/s41467-021-26571-7,https://doi.org/10.1038s41467-021-26571-7.*
[5]*Jing, Junjun, et al. "Spatiotemporal Single-Cell Regulatory Atlas Reveals Neural Crest Lineage Diversification and Cellular Function during Tooth Morphogenesis." Nature Communications, vol. 13, no. 1, 16 Aug. 2022, https://doi.org/10.1038/s41467-022-32490-y.*

Effect of Static Magnetic Fields on the Proliferation and Differentiation of Dental Pulp Stem Cells Cultured In Vitro on Collagen Scaffolds

Alexander Cheng[1], Shaun Johnet[2], Xinying (Louis) Li[3], Timur Volkov[4], Anthony Zhao[5], Lingjie Pan[6], Kao Li[7], Huiting Luo[8], Miriam Rafailovich[8]

[1] Spring Branch Academic Institute, Houston, TX 77079, [2]Archimedean Upper Conservatory, Miami, FL 33183, [3]Shenzhen Middle School, Guangdong, China 518000, [4] University of Toronto Schools, Ontario, Canada M5S 2R7 ,[5] Ladue Horton Watkins High School, Ladue, MO 63124, [6]Department of Chemistry, Stony Brook University, Stony Brook, NY 11794, [7]School of Biomedicine and Nursing, Shandong Institute of Petroleum and Chemical Technology, Shandong, China 257099, [8]Department of Materials Science & Engineering, Stony Brook University, Stony Brook, NY 11794

Type I Collagen is the most abundant protein in the human body and makes up most of the extracellular matrix (ECM). As such, synthetic collagen scaffolds have shown promise in replicating body ECM conditions in order to culture cells, highly applicable in regenerative medicine, a field focused on repairing damaged tissues and organs [1]. In this study, we consider the generation of bone or dental constructs upon these scaffolds using dental pulp stem cells (DPSCs). Following past publications that demonstrate the ability of static magnetic fields (SMFs) to promote the differentiation and proliferation of these cells [2], we explored this technique in conjunction with collagen scaffolds.

DPSC cells of passage 5 were divided equally into four treatment groups: control, Type I collagen gel, SMF, and Type I collagen gel with SMF. To determine the effect of a range of magnetic fields on cells, SMFs of 26 - 296mT measured with a gaussmeter were applied to cells in the magnet treatment groups through the duration of the experiment by sandwiching cell plates between neodymium magnet plates of the same size. These cell plates were then incubated at 37°C and with 5% CO_2.

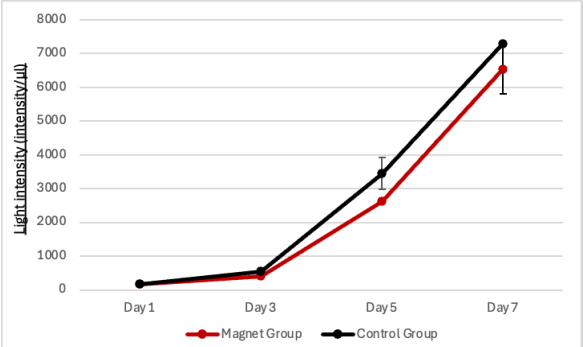

Figure 1: Cell Proliferation Measurement by AlamarBlue

To quantify the effect of the magnetic treatment versus control on cell proliferation, Alamar blue assay was performed on samples without collagen on days 1, 3, 5, and 7. A decreasing but not statistically significant (paired sample t-test, $p>0.05$) cell count was seen between magnet and control groups on day 1, 3, and 7, while there was a significant difference on day 5 (Fig 1).

Cell differentiation will be analyzed by comparing elastic modulus, aspect ratio, and actin fiber thickness. Cells were fixated and visualized under fluoroscopy (EVOS, Thermofisher) on day 7 to analyse their morphology. The next step is to collect and quantify these parameters.

In future study, this experiment will be repeated with a larger sample size to be statistically significant and robust. Cell differentiation and biomineralization will be determined using Alizarin Red staining (ARS), qRT-PCR, and AFM. ARS produces a red stain when bound to calcium ions and allows quantitative analysis of biomineralization. AFM with constant force will be used to determine the modulus of the cells as they mineralize, providing early insight into their differentiation progress [3]. qRT-PCR will be done on day 14 and day 28 to quantitatively determine the expression of genes relevant to differentiation (DSPP, DMP1, OCN, OPN, ALP and COL1A1) [4].

[1] Dong C, Lv Y. Application of Collagen Scaffold in Tissue Engineering: Recent Advances and New Perspectives. Polymers (Basel). 2016 Feb 4;8(2):42. doi: 10.3390/polym8020042. PMID: 30979136; PMCID: PMC6432532.

[2] Na J, Zhang L, Zheng L, Jiang J, Shi Q, Li C, Fan Y. Static magnetic field regulates proliferation, migration, and differentiation of human dental pulp stem cells by MAPK pathway. Cytotechnology. 2022 Jun;74(3):395-405. doi: 10.1007/s10616-022-00533-3. Epub 2022 Apr 20. PMID: 35733699; PMCID: PMC9206967.

[3] Jones, T. D., Naimipour, H., Sun, S., Cho, M., & Alapati, S. B. (2014). Mechanical changes in human dental pulp stem cells during early odontogenic differentiation. *Journal of Endodontics*, *41*(1), 50–55. https://doi.org/10.1016/j.joen.2014.07.030

[4] Ching, H.S., Kannan, T.P., Luddin N., Ab Rahman, I., & Ghani, N. R. N. A. (2020). Early Odontogenic Differentiation of Dental Pulp Stem Cells Treated with Nanohydroxyapatite–Silica–Glass Ionomer Cement. *Polymers*, *12*(9), 2125–2125. https://doi.org/10.3390/polym12092125

Evaluation of in-vitro CASA-induced biomineralization via stem cell differentiation

Suhrith Muvvala[1], Felicity Liao[2], Sean Lee[3], Alyssa Wang[4], Shuyan Li[5], Ahyoung Song[6], Harper Falivene[7], Lucas Hofflich[8], Briman Yang[9], Muyun Cui[9], Huiting Luo[9], Jessica Hofflich[9], Shi Fu[9], Miriam Rafailovich[9]

[1]Portola High School, Irvine, CA 92618, [2]Cushing Academy, Ashburnham, MA 01430, [3]Lambert High School, Suwanee, GA 30024, [4]East Ridge High School, Woodbury, MN 55129, [5]Suzhou North America High School, Jiangsu, China 215000, [6]International Academy East, Troy, MI 48083, [7]South Side High School, Rockville Center, NY 11570, [8]Tuckahoe High School, Eastchester, NY 10709, [9]Stony Brook University, Stony Brook, NY 11794

Endodontic infections initiated by *Enterococcus faecalis* remain the primary obstacle to successful root canal treatment, causing persistent tooth pain, reinfection, and degradation of surrounding bone tissue.[1,2] Calcium hydroxide and salicylic acid (CASA) is a novel material currently being studied as a prospective endodontic root canal treatment. A previous study has shown its antibacterial properties against *E. faecalis* and its potential to upregulate genes involved in osteogenic differentiation.[3] However, an exhaustive investigation of CASA's regenerative properties has yet to be conducted. Given its proven antibacterial properties, if CASA is proven to promote bone/tissue repair, it could serve as a more effective alternative to current commercial root canal fillings such as Vista-Cal™. Thus, the focus of this study is to characterize the regenerative potential of CASA by evaluating the biomineralization and differentiation of iPSCs and DPSCs.

CASA was prepared by mixing calcium hydroxide and salicylic acid in a 1:6 ratio. 20% w/w F127-DMA hydrogel was then combined with 0.1% w/v Lithium Phenyl Phosphinate (LAP), a UV-crosslinker and photo-initiator. CASA was then encapsulated in the photo-crosslinked, thermo-reversible F127-DMA hydrogel at varying concentrations and placed on cell culture inserts to treat iPSCs and DPSCs. After 21 days of exposure for iPSCs and 28 days of exposure for DPSCs, biomineralization was characterized through Alizarin Red Staining (ARS).

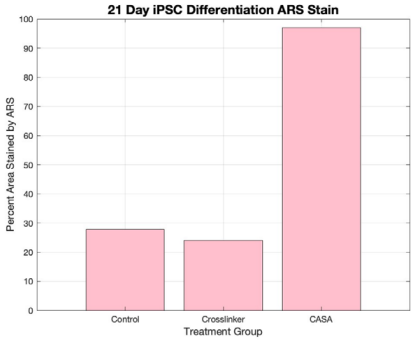

Figure 1: Percent area covered by the ARS stain after three washes with PBS was graphed. Minimal difference between the control and the hydrogel without CASA was shown, with a large increase of Alizarin-Red S retention in the group treated with CASA

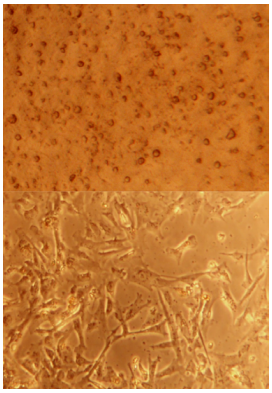

Figure 2: Microscopy image of cell morphology undifferentiated iPSCs (top), and twelve days into differentiation (bottom)

A significant increase in biomineralization was shown in the 20% CASA sample, with nearly 70% more area being covered by the ARS stain than with the control (Fig. 1). Further, changes in cell morphology indicative of differentiation were observed as well, including elongated and translucent cell bodies (Fig. 2). The exact composition and structure of biomineralization will be further validated via SEM/EDX, and the mechanism responsible for the differentiation of the cells will be quantified using qRT-PCR by focusing on genetic markers specific to osteoblasts and odontoblasts.

Our results provide a promising outlook on CASA as an endodontic root canal treatment to induce bone regeneration in the periapical dental region, positioning CASA as a novel substance with antibacterial and restorative properties that promotes recovery from persistent *E. faecalis* infection.

[1] F. Alghamdi and M. Shakir, "The influence of enterococcus faecalis as a dental root canal pathogen on endodontic treatment: A systematic review," Cureus, vol. 12, p. 7257, Mar 2020. PMID: 32292671; PMCID: PMC7152576.

[2] Z. Deng, B. Lin, F. Liu, and W. Zhao, "Role of enterococcus faecalis in refractory apical periodontitis: from pathogenicity to host cell response," Journal of Oral Microbiology, vol. 15, p. 2184924, Mar 2023.

[3] F. Koosha, J. Cymerman, T. Manders, M. Simon, S. Walker, and M. Rafailovich, "Non-cytotoxic root canal dressing with improved antimicrobial efficacy," Journal of Endodontics, vol. 4, pp. 205–211, Feb 2023. Epub 2022 Dec 14. PMID: 36528174.

In Vivo Evaluation of an Innovative Injectable and Retrievable Drug Delivery System for Endodontic Therapy Using a Canine Model

Brenna Ren[1], Abdel H. Mahmoud[2], Karin Hasegawa[3], Fernando Aguilar Perez[4], Nabila Jaman Tripti[3], Miriam Rafailovich[4]
[1]The Harker School, San Jose, CA 95129, [2]Stony Brook School of Dental Medicine, Stony Brook, NY 11790, [3]Department of Applied Mathematics and Statistics, Stony Brook University, Stony Brook, NY 11790, [4]Department of Materials Science and Chemical Engineering, Stony Brook University, Stony Brook, NY 11790

Endodontic treatment failures, commonly resulting from persistent apical periodontitis caused by *Enterococcus faecalis*, pose a significant challenge in dental treatment[1]. While calcium hydroxide remains the predominant medicament, it lacks sufficient antimicrobial efficiency against *E. faecalis*, is caustic, and has poor injection and retrieval properties. We developed a mixture of calcium hydroxide and salicylic acid (CASA) encapsulated in thermoreversible hydrogels (F127-DMA). Previous in vitro studies demonstrated the hydrogel's effective antimicrobial properties, flowability, retrievability, stability, and hydrophilicity, highlighting it as a promising alternative to calcium hydroxide in root canal treatments. In this preliminary study, we evaluated the in vivo performance of the F127-DMA/CASA hydrogel by assessing its impact on periapical healing and cortical bone regeneration in a canine model.

We studied 18 distinct teeth of 10-month-old and 16-month-old beagles across 10 visits, spaced two weeks apart for the first 8 visits and four weeks apart for the last 2 visits. Each dog had 3 teeth in each of the 3 treatment groups: F127-DMA/CASA, Vista-Cal (current gold standard), and non-medicated. The teeth were infected using *E. faecalis* at the 2nd visit, treated with the hydrogel at the 5th visit, and obturated with Gutta-Percha after the hydrogel was removed at the 7th visit. Cone beam computed tomography (CBCT) scans were taken at each visit.

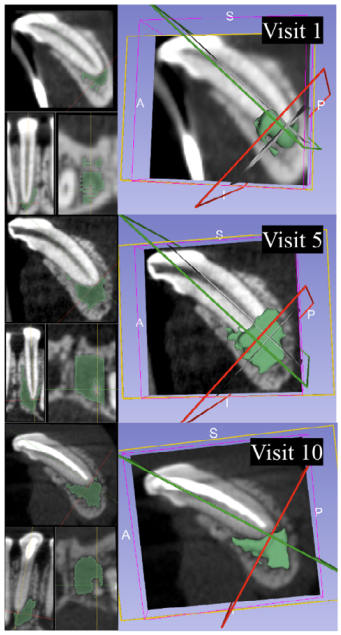

Figure 1. Axial, coronal, sagittal, and 3D views of the 1st upper left premolar tooth of the 16-month-old dog for the 1st visit (pre-inoculation), 5th visit (F127-DMA/CASA added), and 10th visit (18 weeks post-CASA).

Our preliminary analysis focused on one tooth per treatment group (the 1st and 2nd upper left incisors and 1st premolar of the 16-month-old dog). We performed 3D segmentation and volumetric analysis of the periapical regions using 3D Slicer Software, as shown in Figure 1. Each tooth was first isolated by cropping from CBCT scans. The periapical radiolucent regions, which are indicative of infection or inflammation, were segmented using standardized thresholding parameters and anatomical markers to ensure consistency. For cortical bone analysis, we measured the maximum length of visible discontinuity, which served as a metric of bone destruction and healing.

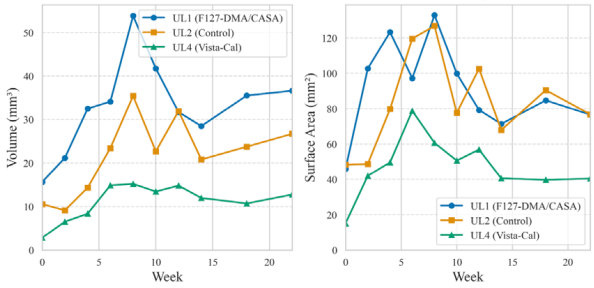

Figure 2. Volume (left) and surface area (right) of the periapical region of the 1st (UL1), 2nd (UL2), and 4th (UL4) upper left premolars in response to different treatments: F127-DMA/CASA (UL1), control (UL2), and Vista-Cal (UL4).

From the 5th to 10th visit, or 14 weeks post-treatment, the periapical region volume of the F127-DMA/CASA treated tooth decreased by 32.0%, which is greater than the volume decrease of the control (26.2%) and Vista-Cal (16.2%). The F127-DMA/CASA-treated tooth's surface area also decreased 42.4%, compared to the control (37.8%) and Vista-Cal (33.3%). These changes are summarized in Figure 2. Additionally, the maximum cortical bone discontinuity length decreased by 57.6%, exceeding the control (45.9%) and Vista-Cal (54.2%), demonstrating that F127-DMA/CASA promotes bone healing and regeneration.

While based on a limited sample size, these preliminary observations provide useful insights into the potential of F127-DMA/CASA hydrogels as an intracanal treatment. Further data analysis on the other teeth following the Garcia Summer Program is needed to validate these findings and better understand the hydrogel's therapeutic effects for persistent apical periodontitis in endodontic therapy.

[1]Alghamdi, Faisal, and Marwa Shakir. "The Influence of Enterococcus Faecalis as a Dental Root Canal Pathogen on Endodontic Treatment: A Systematic Review." Cureus, U.S. National Library of Medicine, 13 Mar. 2020, www.ncbi.nlm.nih.gov/pmc/articles/PMC7152576/.

Deep Learning-Based Segmentation of CBCT Sinus Scans for Mucosal Thickening Classification

Eun-Seo (Emily) Song[1], Katelyn Deng[2], Karin Hasegawa[3], Yuefan Deng[3]
[1]Cornerstone Collegiate Academy of Seoul, Seoul, South Korea, 06779, [2]Connecting Waters Charter School East Bay, Union City, CA 94587, [3]Department of Applied Mathematics and Statistics, Stony Brook University, Stony Brook, NY 11794

Chronic sinusitis, or long-term inflammation of the sinus, affects millions worldwide and is frequently associated with mucosal thickening, sinus obstruction, or in more severe cases, mucous retention cysts and tumors[1]. Accurate identification of such abnormalities is essential for diagnosis and surgical planning. Cone-beam computed tomography (CBCT) imaging enables high-resolution visualization of sinus structures for clinicians to annotate and segment; however, the manual segmentation process remains time-intensive, prone to inter-observer variability, and difficult to scale universally[2]. To address these limitations, we developed a fully automated deep-learning pipeline based on a 3D U-Net architecture to segment CBCT sinus scans into three voxel-level classes: background, maxillary sinus (air), and mucosal thickening (MT). The dataset, provided by the Stony Brook University Dental School, consisted of 3D CBCT volumes from patients with normal sinus anatomy and mucosal thickening, annotated by clinicians. Using the 3D Slicer tool, each scan was cropped and split into left and right maxillary sinuses, yielding 73 single-sinus volumes. We used 51 samples for training, 12 for validation, and 10 for inference, conducting multiple trials on the SeaWulf high-performance supercomputer to optimize segmentation performance.

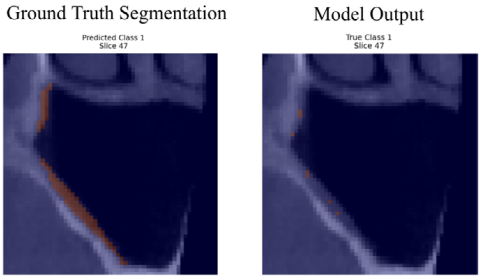

Figure 1. Ground truth segmentation versus model output - Mucosal Thickening visual results for Trial 3 (Refined Dice calculations for MT and MT + Air)

Trial 1 served as the baseline, using standard Dice loss and reporting a Dice Similarity Coefficient score of 0.6237 for mucosal thickening combined with air. In Trial 3, we refined the evaluation by separating Dice calculations for mucosal thickening (MT) and the combined class of MT and air. As shown in Figure 1, the MT Dice scores were extremely low at an average of 0.0265. The model performed slightly better at segmenting general air-filled regions with an average MT and air Dice score of 0.4488.

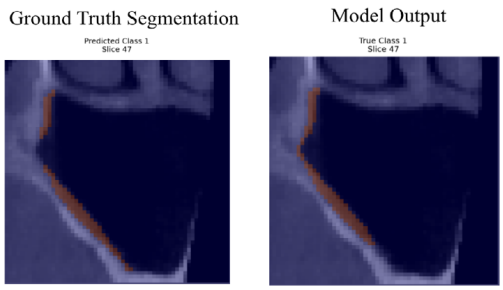

Figure 2. Ground truth segmentation versus model output - Mucosal Thickening visual results for Trial 9 (Added residual blocks and attention gates)

Between Trials 4 to 8, minor adjustments to the loss function and hyperparameters resulted in only modest Dice score gains, prompting Trial 9 to adopt a revised model architecture. This architecture incorporated residual connections to enhance gradient flow and deeper feature learning. We also added attention gates to allow the model to selectively focus on relevant regions within each 3D volume. This produced a marked performance increase (Figure 2), achieving an average Dice score of 0.5984 for MT only and 0.7763 for both MT and air, and IoU scores of 0.4380 and 0.9031, respectively. While performance on mucosal thickening alone still highlights challenges with class imbalance and subtle features, our improvements suggest strong potential for clinical use.

[1]Morgan, N., Van Gerven, A., Smolders, A., de Faria Vasconcelos, K., Willems, H., & Jacobs, R. (2022). Convolutional neural network for automatic maxillary sinus segmentation on cone-beam computed tomographic images. Scientific Reports, 12(1). https://doi.org/10.1038/s41598-022-11483-3

[2]Fernanda Nogueira Reis, Morgan, N., Nomidis, S. K., Adriaan Van Gerven, Nicolly Oliveira-Santos, Jacobs, R., & Pereira, C. (2022). Three-dimensional maxillary virtual patient creation by convolutional neural network-based segmentation on cone-beam computed tomography images. 27(3), 1133–1141. https://doi.org/10.1007/s00784-022-04708-2

Session III:
Energy Generation

Chairs:

Haoyan Fang, MD Farabi Rahman, Allen Bethancourt, Sourav Maiti

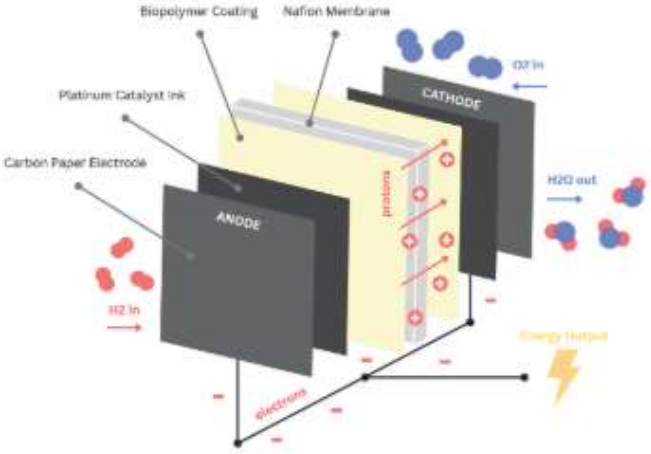

Figure 1: Membrane Electrode Assembly (MEA) using *Rhizobium tropici* derived biopolymer.

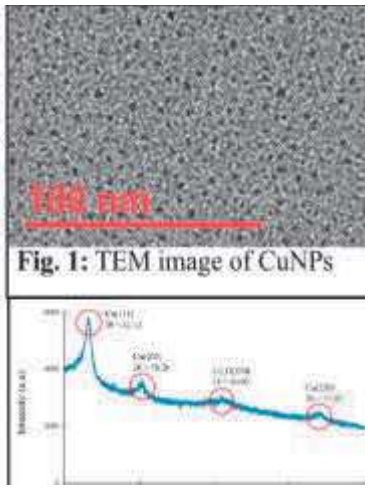

Fig. 1: TEM image of CuNPs

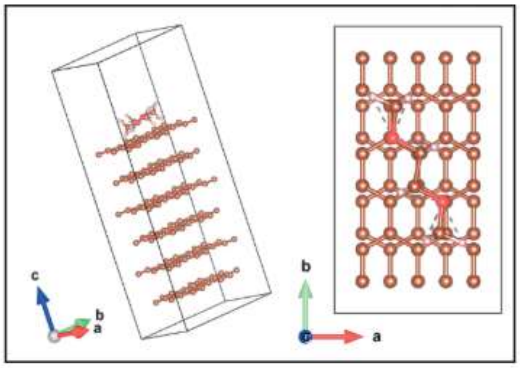

Figure 1: Graphene-DME Slab #3 in VESTA

Improved Proton-Exchange Membrane Fuel Cell Efficiency through Integration of *Rhizobium tropici* derived Extracellular Polymeric Substance

Sarah Dabees[1], Jerry Gu[2], Nirati Iyer[3], Leo Pan-Wang[4], Eric Ji[5], Allen Bethancourt[6], Miriam Rafailovich[6]

[1]Florida Gulf Coast University, Fort Myers, FL 33965, [2]Princeton International School of Mathematics and Science, Princeton, NJ 08540, [3]West Windsor-Plainsboro High School South, West Windsor Township, NJ 08550, [4]The Peddie School, Hightstown, NJ 08520, [5]South Forsyth High School, Cumming, GA 30041, [6]Stony Brook University, Stony Brook, NY 11794

As climate change demands a shift towards clean energy, optimization of renewable energy sources is necessary to meet growing electricity demands. Proton-Exchange Membrane Fuel Cells (PEMFCs) are efficient hydrogen fuel cells that utilize proton transport for the instantaneous conversion of energy stored as hydrogen fuel to electrical energy and are a promising future energy source [1]. Nafion®, a commonly utilized proton-exchange membrane, while highly efficient, also has limitations to operating temperature tolerance and affordability [2]. *Rhizobium tropici* is a common and beneficial bacterium for soil health whose derived biopolymer possesses similar structure to others previously tested with proton-conductive properties [3]. In this study, Extracellular Polymeric Substance (EPS) derived from *R. tropici* was applied to Nafion®-117 membranes to evaluate performance enhancement of a PEMFC (**Figure 1**). A Membrane Electrode Assembly (MEA) with platinum catalyst carbon electrodes was run in a fuel cell test station in contrast to an MEA using a biopolymer-coated Nafion® membrane for power density comparison. The EPS-coated membrane resulted in a wider power curve with higher maximum output, as well as a longer voltage drop for the same current density (**Figure 2**). Additionally, characterization of the EPS Nafion® using X-Ray Diffraction (XRD) and Differential Scanning Calorimetry (DSC) demonstrated both confirmed presence of the biopolymer on the Nafion® membrane and an increased thermal tolerance, respectively. The increase in both efficiency by roughly 45% and specific heat of the Nafion® membrane by 27% demonstrates the potential of this biopolymer as a sustainable means to enhance fuel cell efficiency.

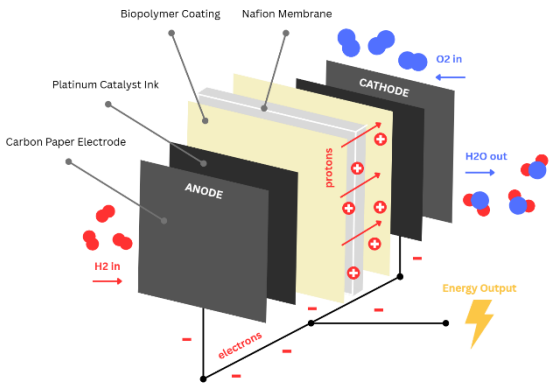

Figure 1: Membrane Electrode Assembly (MEA) using *Rhizobium tropici* derived biopolymer.

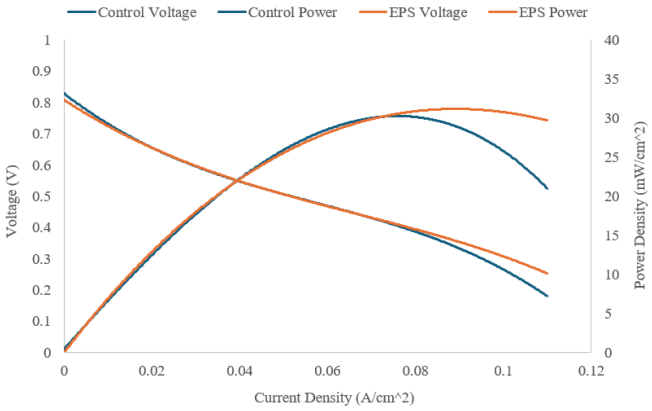

Figure 2: Polarization curve of Proton-Exchange Membrane Fuel Cell (PEMFC) using Extracellular Polymeric Substance (EPS) from *Rhizobium tropici.*

[1]Alaswad, A., Palumbo, A., Dassisti, M., & Olabi, A. G. (2016). Fuel Cell Technologies, applications, and state of the art. A reference guide. Reference Module in Materials Science and Materials Engineering. https://doi.org/10.1016/b978-0-12-803581-8.04009-1

[2]Ahmad, S., Nawaz, T., Ali, A., Orhan, M. F., Samreen, A., & Kannan, A. M. (2022). An overview of proton exchange membranes for fuel cells: Materials and manufacturing. International Journal of Hydrogen Energy, 47(44), 19086–19131. https://doi.org/10.1016/j.ijhydene.2022.04.099

[3]Jia, M., Kim, J., Nguyen, T., Duong, T., & Rolandi, M. (2021). Natural biopolymers as Proton Conductors in bioelectronics. Biopolymers, 112(7). https://doi.org/10.1002/bip.23433

Performance Enhancement of Anion Exchange Membrane Fuel Cells via ZnO Atomic Layer Deposition and Silver Nanoparticle LB Coating

Kayla Etra[1], Michael He[2], Mathieu Wang[3], Hanyuan Yang[4], Haoyan Fang[5], Miriam Rafailovich[5]

1. Yeshiva University High School for Girls, NY, USA 2. Shanghai Pinghe School, Shanghai, China 3. BASIS International School Hangzhou, Zhejiang, China 4. Shanghai World Foreign Language Academy, Shanghai, China 5. Department of Materials Science and Chemical Engineering, State University of New York at Stony Brook, NY, USA

Anion exchange membrane (AEM) fuel cells are a promising technology with high efficiency and low cost, solid advantages when compared to a traditional proton exchange membrane fuel cell. Previous efforts to optimize AEM fuel cell performance have focused on modifying critical components, such as the electrode catalyst and the AEM, in order to enhance the energy conversion efficiency, performance stability, and mechanical durability of the cell[1,2].

In this study, our objective is to determine the effects of zinc oxide (ZnO) coating, silver nanoparticles (AgNPs), and the synergy between them on the power density of AEM fuel cells. We utilized atomic layer deposition (ALD) to deposit layers of ZnO onto a Sustainion™ AEM and collected AEM fuel cell performance data using spray-coated PtRu/C (anode) and Pt/C (cathode) electrodes on a fuel cell test station produced by Fuel Cell Technologies, Inc. The peak power density of 0.668 W/cm^2 was obtained at 10 layers of ZnO coating. Then, we evaluated ZnO's catalytic effects when deposited onto the membrane or onto the electrodes, and found that a fuel cell with a ZnO-coated membrane has a significantly higher performance (Figure 1). We also assessed the effect of combining ZnO deposition with AgNPs by coating a 10-layer ZnO-coated membrane with AgNPs using a Langmuir-Blodgett Trough, reaching a peak power density of 0.689 W/cm^2.

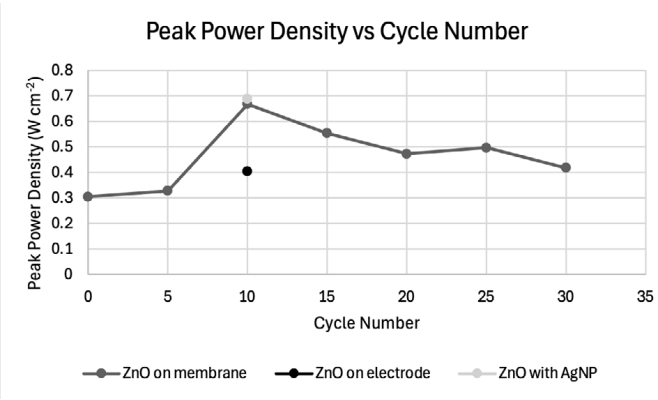

Figure 1. Peak power density of AEM fuel cells with different number of layers of ZnO coatings by ALD on membrane and electrode, with and without AgNPs.

Our results show that the performance of AEM fuel cells is strongly enhanced by the addition of atomic layer deposited ZnO, with a 119% increase in peak power density. The addition of AgNPs results in a further 3.14% increase in peak power density. This data shows the promising potential of applying techniques like ALD and nanoparticle coating to further develop AEM fuel cell technology as an applicable energy solution.

---

[1] Park, A. M., & Moore, J. S. (2021). Designing anion exchange membranes: From molecular mechanisms to macroscopic properties. Sustainable Energy & Fuels, 5(1), 47–67. https://doi.org/10.1039/D0SE01373K

[2] Géraldine Merle, Matthias Wessling, Kitty Nijmeijer, Anion exchange membranes for alkaline fuel cells: A review, Journal of Membrane Science, Volume 377, Issues 1–2, 2011, Pages 1-35, ISSN 0376-7388, https://doi.org/10.1016/j.memsci.2011.04.043

Cost-Effective Thiol-Capped Copper Nanoparticle Surface Engineering for Enhanced Durability and Performance in Proton Exchange Membrane Fuel Cells

Eric Ji[1,2], Ian Kim[1,3], Kitty Lai[1,4], Md. Farabi Rahman[1], Miriam Rafailovich[1]

[1]*Stony Brook University, Stony Brook, NY 11794,* [2]*South Forsyth High School, Cumming, GA 30041,* [3]*Hicksville High School, Hicksville, NY 11801,* [4]*Milton Academy, Milton, MA 02186*

Over the past few years, there have been significant global efforts to address decarbonization needs as outlined in the Paris Agreement of 2015, the latest major international treaty on climate change.[1] Utilizing abundant hydrogen fuel and emitting water as the only byproduct, hydrogen fuel cells constitute a cleaner and more sustainable energy source in comparison to traditional combustion-based fuels; independent of weather conditions, they generate energy that is more reliable and consistent compared to conventional renewable sources such as solar or wind power.[1] Furthermore, their portability and moderate operating conditions have placed proton exchange membrane fuel cells (PEMFC) at the forefront of hydrogen fuel cell technology.[2]

However, notable issues with using PEMFC include its low power density, poor long-term durability, and the risk of degradation of platinum catalysts from carbon monoxide (CO), a gas commonly found in hydrogen fuel sources.[2,3] This ongoing study aims to address these challenges by exploring the use of dodecanethiol-capped copper nanoparticles (CuNPs) for increasing both power output and lifetime.

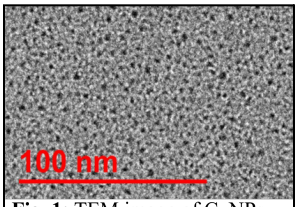

Fig. 1: TEM image of CuNPs

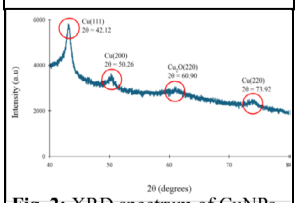

Fig. 2: XRD spectrum of CuNPs

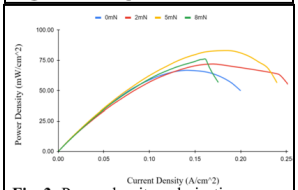

Fig. 3: Power density polarization curves

CuNPs are particularly attractive due to their reduced material cost while maintaining promising catalytic behaviors.[4] To evaluate CuNPs, this study utilizes a modified Brust-Schiffrin (B-S) method to investigate the effects on maximum power densities (MPD) and life cycle durability of PEMFCs via the surface engineering of proton exchange membranes with CuNPs.

CuNPs were synthesized through a modified B-S method in a two-phase process (inorganic and organic phase), where Cu(II) is reduced to Cu(0) in the presence of dodecanethiol and sodium borohydride.[5] The dodecanethiol then binds to the CuNPs via Cu–S interactions, forming a protective self-assembled monolayer that prevents CuNPs from oxidizing or aggregating. Characterization results from transmission electron microscopy (TEM) illustrate the successful synthesis of nanoparticles with no visible agglomeration as indicated by consistent spherical geometries of individual nanoparticles (mean diameter = 1.8 ± 0.44 nm) (Fig. 1). Further characterization through X-ray diffraction (XRD) exhibits characteristic diffraction peaks for crystalline CuNPs and a slight cuprous oxide diffraction peak likely from slight oxidation of CuNPs during synthesis or storage (Fig. 2), overall indicating successful synthesis.

The performance of the fuel cell was assessed using a fuel cell testing station with Pt-coated (0.01mg/cm^2) carbon electrode. CuNPs were deposited onto Nafion-117 membranes via Langmuir–Blodgett trough at surface tensions 2 mN/m, 5 mN/m, and 8 mN/m, pressures within the predetermined range for monolayer formation. For these pressures, testing results reveal a 7.86%, 24.4%, and 13.7% increase in maximum power density, respectively, compared to the control (0 mN/m) (Fig. 3), suggesting a significant enhancement in the catalytic/proton transfer mechanisms. A possible explanation for the decrease in MPD at 8 mN/m may be that the higher surface deposition of CuNPs exceeds the desired monolayer formation and thus is less efficient for proton transfer.

The present study contributes significantly to the literature seeking to validate CuNPs as PEMFC performance enhancers. Ongoing work aims to evaluate synergistic effects of CuNPs with zinc oxide atomic layer deposition, improvements in CO poisoning resistance, and enhancements in fuel cell durability up to 30K rapid charge/discharge cycles.

[1] Baharuddin, N. A., Yusoff, W. W., Abd Aziz, A. J., & Tahir, N. M. (2021, February). Hydrogen fuel cells for sustainable energy: Development and progress in selected developed countries. In IOP conference series: Materials science and engineering (Vol. 1078, No. 1, p. 012011). IOP Publishing.

[2] Park, S., Lee, E., Park, Y., Kim, M.-G., & Yoo, S. J. (2025). Toward hydrogen mobility: Challenges and strategies in electrocatalyst durability for long-term PEMFC operation. JACS Au, 5(4), 1617–1632. https://doi.org/10.1021/jacsau.5c00173

[3] Jiao, K., Xuan, J., Du, Q., Bao, Z., Xie, B., Wang, B., Zhao, Y., Fan, L., Wang, H., Hou, Z., Huo, S., Brandon, N. P., Yin, Y., & Guiver, M. D. (2021). Designing the next generation of Proton-exchange membrane fuel cells. Nature, 595(7867), 361–369. https://doi.org/10.1038/s41586-021-03482-7

[4] Gawande, M. B., Goswami, A., Felpin, F.-X., Asefa, T., Huang, X., Silva, R., Zou, X., Zboril, R., & Varma, R. S. (2016). Cu and Cu-based nanoparticles: Synthesis and applications in catalysis. Chemical Reviews, 116(6), 3722–3811. https://doi.org/10.1021/acs.chemrev.5b00482

[5] Brust, M., Walker, M., Bethell, D., Schiffrin, D. J., & Whyman, R. (1994). Synthesis of thiol-derivatised gold nanoparticles in a two-phase liquid-liquid system. Journal of the Chemical Society, Chemical Communications, (7), 801-802. https://doi.org/10.1039/C39940000801

High-Throughput DFT Modeling of Graphite-Dimethoxyethane and Platinum-Water Interfaces for Energy Applications

Jasper Stackawitz[1]*, George Mirgorodskiy[2]*, Maggie Li[3]*, Sourav Maiti[4], Nav Nidhi Rajput[4], Miriam Rafailovich[4]

[1]Pennsbury High School, PA, [2]The Loomis Chaffee School, CT, [3]Jericho Senior High School, NY, [4]Stony Brook University, NY

In lithium-ion batteries, graphite is often used as the anode material with an ethylene-carbonate (EC) electrolyte and its properties have been studied extensively. This study aims to explore certain energy-related properties of potential alternatives to graphite-EC batteries, specifically graphite-dimethoxyethane (DME) Li-ion batteries and platinum-water fuel cells, using automated Density Functional Theory (DFT) simulations.

DFT is a quantum-mechanical modeling method used to investigate the electronic structure of atoms, molecules, and solids by examining electron density as the fundamental variable. The interfaces were modeled with VESTA and the DFT calculations were done using VASP, which requires input files defining parameters for the calculation. PBE functional and PAW pseudopotentials were chosen.

Creating and validating these files by hand is time consuming, so parts of the process were automated using Python scripts. The main script calls the Materials Project API through Pymatgen to download crystal structures and generate atomic position files based on user-specified parameters, such as the compound and dimensions of the lattice and the properties of the slab. Additional scripts were used to automate the creation of the other files. This allows for high-throughput calculations and scalable exploration of interfaces, important for large systems.

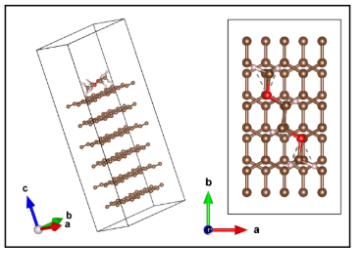

Figure 1: Graphene-DME Slab #3 in VESTA

For the graphite-DME interface, a 5-layer graphite slab model was created in VESTA with a DME molecule, chosen due to its high Li^+ mobility and low viscosity, placed on top in 3 different positions (*fig. 1)*[1]. An ionic relaxation was run in VASP to determine the adsorption energy (E_{ads}) of the system. Our results showed a strong adsorption energy in slabs 2 and 3 (-0.706 eV and -0.580 eV) and a weak adsorption energy in slab 1 (-0.0585 eV), suggesting that an *a-b* orientation of the DME results in better energy transfer and that graphite-DME may be a viable alternative to graphite-EC systems in Li-ion batteries.

Additionally, to understand the adsorption of water on platinum, the most commonly used electrocatalyst, we have modeled Pt-water interfaces and are interested in evaluating adsorption energies using DFT calculations[2]. The Pt(111) configuration was selected because it is a relatively stable and well characterized model. A 4-layer Pt slab with an explicitly added water molecule was created using the automated python script and a similar ionic relaxation was run (*fig. 2*).

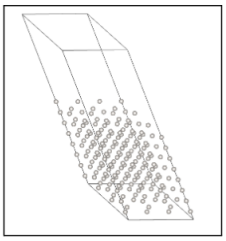
Figure 2: Automatically Generated 4-layer Pt Slab

Further analysis is being conducted using Bader Charge Analysis for both systems to visualize and analyze their charge distributions and further determine their viability for energy-based application following the so-far promising results.

[1]Seo, H., Kim, D., Park, S. et al. A comprehensive review of liquid electrolytes for silicon anodes in lithium-ion batteries. Adv. Ind. Eng. Chem. 1, 3 (2025). https://doi.org/10.1007/s44405-025-00004-1

[2]Ungerer, M. J., Santos-Carballal, D., Cadi-Essadek, A., van Sittert, C. G., & De Leeuw, N. H. (2019). Interaction of H2O with the Platinum Pt (001),(011), and (111) surfaces: a density functional theory study with long-range dispersion corrections. The Journal of Physical Chemistry C, 123(45), 27465-27476.

Session IV: Computational Methodology

Chairs:

Manoj Praveen Nandigama, Kuldeepsinh Raj, Ruichen Xu, Haochun Wang, Karin Hasegawa

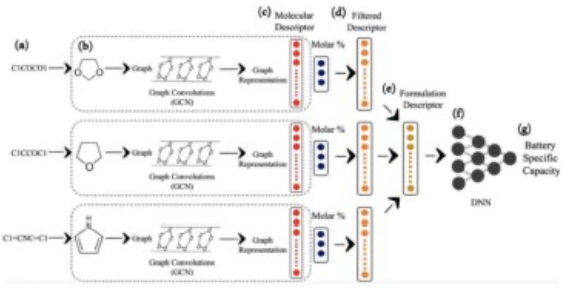

Figure 2: Visualization of the F-GCN model [2]

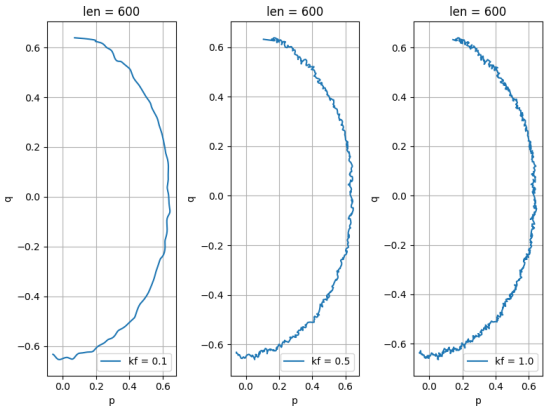

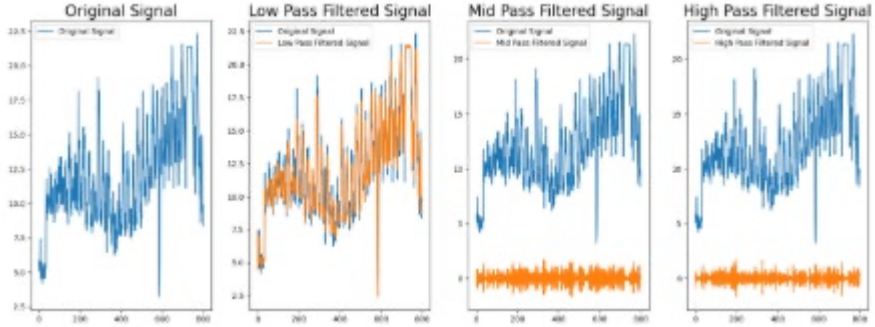

Leveraging a Large Language Model to Build Structured Electrolyte Databases for Multicomponent Property Prediction

Ray Zhang[1], Albert Huang[2], Yuanxi Yao[3], Manoj Praveen Nandigama[4], Kuldeepsinh Raj[4], Nav Nidhi Rajput[4]

[1] *St. George's School, Vancouver, Canada,* [2] *Saigon South International School, Ho Chi Minh City, Vietnam,* [3] *Shenzhen Middle School, Shenzhen, China,* [4] *Stony Brook University, NY, 11790*

Electrolytes are an integral component of various cutting-edge electrochemical applications. As technologies like electric vehicle batteries and carbon dioxide electrochemical reduction (CO_2ER) advance, their performance is increasingly dependent on their electrolyte properties. However, electrolytes are generally not single components, but instead complex mixtures of solvents and salts which determine their properties. As such, identifying optimal compositions is both experimentally challenging and computationally intensive [1]. To address this, we explore the usage of a Formulation Graph Convolution Network (F-GCN), a deep learning model for multicomponent electrolyte property prediction [2]. Structured datasets for training this model are currently unavailable [3]; therefore, this study involves the construction and employment of a Large Language Model (LLM), called BatteryLLM, for automated data extraction of electrolyte data from scientific literature, creating a comprehensive, structured database to train the F-GCN model to accelerate accurate prediction of electrolyte properties.

We assembled a corpus of relevant literature: 21 scientific electrolyte-related articles in PDF format. Each PDF was then converted with GROBID (GeneRation Of Bibliographic Data) into JSON (JavaScript Object Notation) files, yielding structured documents preserving the text and figures of the original PDFs. These files are passed into the OpenAI API with a prompt detailing the electrolyte information to search for, along with instructions to ensure consistency in units and JSON formatting. We then utilized MongoDB to insert each output JSON file into a database for accessible processing. From here, we manually benchmarked the model's performance by searching for the electrolyte properties in the original papers and comparing with the model outputs. Thus, we could determine the precision and recall of the model, and in turn find that the F1 score is 0.840 (Fig. 1). This indicates that the model performs well overall, as we plan on further refining it through extensive prompt engineering.

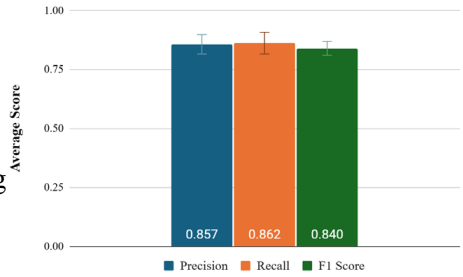

Figure 1: Average values of precision, recall and F1 score of BatteryLLM

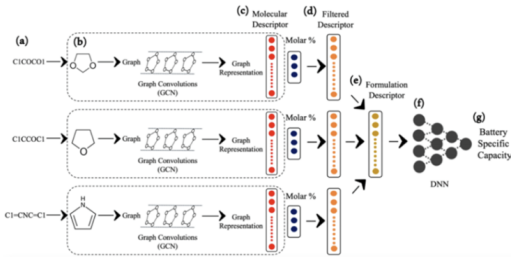

Figure 2: Visualization of the F-GCN model [2]

This database will be used to train a F-GCN model, a deep learning model capable of predicting the properties of the liquid formulation in multicomponent systems from the structure-composition relationships of its constituents [2]. The framework has two components: a Graph Convolutional Network that generates formulation descriptors encoding molecular structure and composition, and a Deep Neural Network that uses these descriptors to predict electrolyte properties via backpropagation (Fig. 2). While originally designed to predict battery capacity and Coulombic efficiency, it will be retrained to predict two key metrics for CO_2ER: Faraday efficiency and current density, leveraging the data gathered by BatteryLLM. Overall, due to minimizing extensive manual data aggregation, this LLM-focused approach is promising not just for CO_2ER, but also broader applications in electrolyte-based technology.

[1] Sharma, V., Tek, A., Nguyen, K., Giammona, M., Zohair, M., Sundberg, L., & La, Y.-H. (2025). Improving electrolyte performance for target cathode loading using an interpretable data-driven approach. *Cell Reports Physical Science*, *6*(1). https://doi.org/https://doi.org/10.1016/j.xcrp.2024.102347

[2] Sharma, V., Giammona, M., Zubarev, D., Tek, A., Nugyuen, K., Sundberg, L., Congiu, D., & La, Y.-H. (2023). Formulation Graphs for Mapping Structure-Composition of Battery Electrolytes to Device Performance. *Journal of Chemical Information and Modeling*, *63*(22), 6998–7010. https://doi.org/https://doi.org/10.1021/acs.jcim.3c01030

[3] Chew, A. K., Afzal, M. A. F., Kaplan, Z., Collins, E. M., Gattani, S., Misra, M., Chandrasekaran, A., Leswing, K., & Halls, M. D. (2025). Leveraging high-throughput molecular simulations and machine learning for the design of chemical mixtures. *Npj Computational Materials*, *11*, Article 72. https://doi.org/https://doi.org/10.1038/s41524-025-01552-2

Adaptive-Balance Active Learning for Neural Operators

Aiden Kwon[1], Ruichen Xu[2], Yuefan Deng[2]
[1]Palos Verdes Peninsula High School, [2]Stony Brook University

Neural Operators are emerging as a promising method for solving Partial Differential Equations (PDEs) due to their ability to map between function spaces. Common variants include the Fourier Neural Operator (FNO) and DeepONet. A key advantage is discretization invariance, in which differing spatial or temporal resolutions do not require retraining.[1] To train a neural operator, a dataset with the initial conditions, PDE parameters, and the corresponding solutions must be available. This often requires prohibitively expensive numerical solvers for dataset labeling. Active learning is a method that cuts simulation costs by selectively choosing training samples.[2] Selected samples must balance uncertainty and diversity to ensure optimal training. This research proposes Adaptive-Balance Active Learning (ABAL), a strategy that dynamically balances uncertainty and diversity by gradually adjusting the exponent p in the PDE loss throughout training, making the data-acquisition process adaptive.

A one-dimensional Bateman-Burger's dataset of 2048 samples is split into initial labeled, validation, and test data (100/100/100). The remaining data are treated as the unlabeled pool from which samples are chosen during the active learning loop. A four layer Fourier Neural Operator is trained with batch size 20 and learning rate 10^{-3}. An adaptive-balance schedule raises the PDE-loss exponent (p) from 0.1 to 10 across the total number of epochs, gradually shifting acquisition from exploration (high diversity sampling) to exploitation (high uncertainty sampling). In each active learning round, the FNO scores the unlabeled pool of data and draws 20 candidates, updating the training dataset. The proposed dynamic-p strategy is compared to a static-p variant, pure uncertainty sampling, and random sampling over 10, 30, and 50 active learning iterations. Each configuration is repeated for ten random seeds, and the average validation mean-squared error (MSE) curves with a 95% confidence interval are reported. The dynamic method shows consistent improvement over the static variant after approximately halfway through the learning process for all configurations. When evaluated on the separate test dataset, ABAL shows reduction in MSE for 10 and 30 iterations, but performs slightly worse when running 50 iterations.

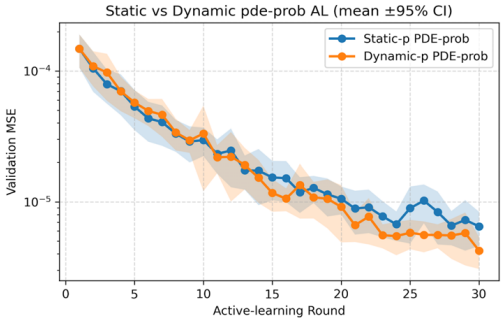

Fig 1. Static vs Dynamic PDE Loss for 50 AL Iterations

Iterations	Seeds	Type	Average Test MSE (± Std)
10	10	Static	$2.9995 \times 10^{-5} \pm 4.6203 \times 10^{-6}$
10	10	Dynamic	$2.5536 \times 10^{-5} \pm 5.0724 \times 10^{-6}$
30	10	Static	$6.2446 \times 10^{-6} \pm 9.4677 \times 10^{-7}$
30	10	Dynamic	$4.2722 \times 10^{-6} \pm 9.0632 \times 10^{-7}$
50	10	Static	$3.8151 \times 10^{-6} \pm 1.0359 \times 10^{-6}$
50	10	Dynamic	$3.9458 \times 10^{-6} \pm 1.2414 \times 10^{-6}$

Table 1: Average Test MSE for Static v. Dynamic

Overall, ABAL allows the Fourier Neural Operator to balance between training on uncertain and diverse samples, resulting in improvement over static processes. The current limitation of this research is its applicability to 3D PDEs, as the 1D Burger's dataset was utilized for the development of the ABAL framework. Future work can explore a wider range of datasets, including Darcy Flow and Navier-Stokes.

[1]Nikola B. Kovachki, Zongyi Li, Burigede Liu, Kamyar Azizzadenesheli, Kaushik Bhattacharya, Andrew M. Stuart, and Anima Anandkumar. Neural operator: Learning maps between function spaces. Journal of Machine Learning Research, 24(89):4061–4157, 2023. arXiv:2108.08481.
[2]Burr Settles. Active learning literature survey. Technical Report 1648, University of Wisconsin–Madison, Computer Sciences Technical Report, 2009.

Fourier-Denoising for Noisy Hamiltonian Systems: Enhancing Symplectic Dynamics Learning

Chloe Ho[1], Ruichen Xu[2], Yuefan Deng[2]
[1]Basis Independent Silicon Valley, CA [2]Stony Brook University, NY

Hamiltonian Neural Networks (HNNs) allow for modeling physical and dynamical systems, but their performance deteriorates when trained on noisy real-world data. We demonstrate that such noise disrupts the symplectic structure HNNs are designed to preserve, leading to unstable trajectories and energy drift [1]. We propose a low-pass Fourier filtering approach to remove high-frequency artifacts prior to training, reducing the mismatch between the true and learned dynamics. Our preliminary findings indicate that this frequency-domain preprocessing substantially enhances HNN robustness, yielding both short-horizon accuracy gains and long-horizon stability.

Low-pass Fourier filtering is a simple yet powerful step for HNN training on noisy data. The keep frequency must be large enough to retain the real dynamical content yet small enough to discard irrelevant high-frequency fluctuations as illustrated in Fig. I. Mathematically, the cutoff Ω_c affects how quickly the final Hamiltonian trajectory deviates. In systems where the natural frequency range is well-known, setting the cutoff near or just above that range yields an effective balance [2].

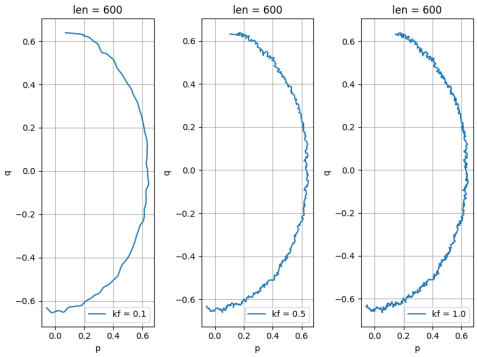

Fig. 1 Mass–spring data across three low-pass filter frequencies k=0.1, k=0.5, and k=1.0

We illustrate the impact of low-pass Fourier filtering on two classical Hamiltonian systems: a mass--spring oscillator and a pendulum (Table. I). In each figure, the test loss is shown at various filtering frequency (k) values. For both experiments, applying a low-pass Fourier filter before HNN training results in better performance than an HNN trained directly on raw noisy data (k=1.0), both achieving the smallest test loss at k=0.5.

k	Mass–Spring Loss	Pendulum Loss
0.1	6.80×10^{-5}	8.68×10^{-5}
0.3	6.77×10^{-5}	8.08×10^{-4}
0.5	6.55×10^{-5}	7.92×10^{-5}
0.6	7.40×10^{-4}	2.44×10^{-4}
0.7	6.76×10^{-5}	2.05×10^{-4}
0.9	1.04×10^{-4}	8.39×10^{-5}
1.0	9.68×10^{-5}	8.27×10^{-5}

Table I. Comparison of test loss across seven low-pass filter frequencies k for mass–spring and pendulum systems

These results, however, also reveal limitations of the Fourier-based filter. If Ω_c is set too low, genuine high-frequency components motions may be lost, creating a bias. Yet, if Ω_c is set too high, significant noise persists in the training signals. Moreover, more complex systems may have richer frequency spectra or time-varying modes that a fixed cutoff cannot fully accommodate. Despite these caveats, the denoised HNN aligns more faithfully with the ground truth and exhibits better stability than the unfiltered model, supporting the premise that discarding high-frequency artifacts curtails the exponential amplification of noise in Hamiltonian models.

[1] Tian Qi Chen, Yulia Rubanova, Jesse Bettencourt, and David K. Duvenaud. Neural ordinary differential equations. In Advances in Neural Information Processing Systems (NeurIPS), 2018.
[2] Bo Chang, Minmin Chen, and Emmanuel Martin. Neural pde-based hamiltonian modeling with energy regularization. IEEE Transactions on Neural Networks and Learning Systems, 33(9):4368–4381, 2022.

Seasonal-Trend-Noise Decomposition via Frequency Band Splitting

Andy Jiang[1], Spark Zhao[2], Haochun Wang[3]

[1]Stuyvesant High School, New York, NY 10282, [2]BASIS International School Guangzhou, Guangzhou, China 510515, [3]Stony Brook University, NY 11790

Time series prediction is essential in various fields, such as supply chain management, healthcare, and finance. Within this domain of prediction problems, the classic approach is to engineer various temporal neural networks that predict data of interest based on either other variables and features or derivative features from the data of interest generated by techniques such as moving average and trend decomposition. Yet, this approach required enormous training resources and time, making it unrealistic to implement in environments where resources are scarce.

On the other hand, time series prediction based on the frequency domain requires fewer computational resources, making peripheral implementation reasonable. As such, we utilize the Frequency Interpolation Time Series (FITS) framework [1] to reinterpret the problem of time series prediction. Using Real Fast Fourier Transform (rFFT) to map low-frequency information to trend, mid-frequency information to cycle and seasonality, and high-frequency information to noise (Figure 1), we aimed to provide a novel perspective to interpret the properties of data in time series prediction.

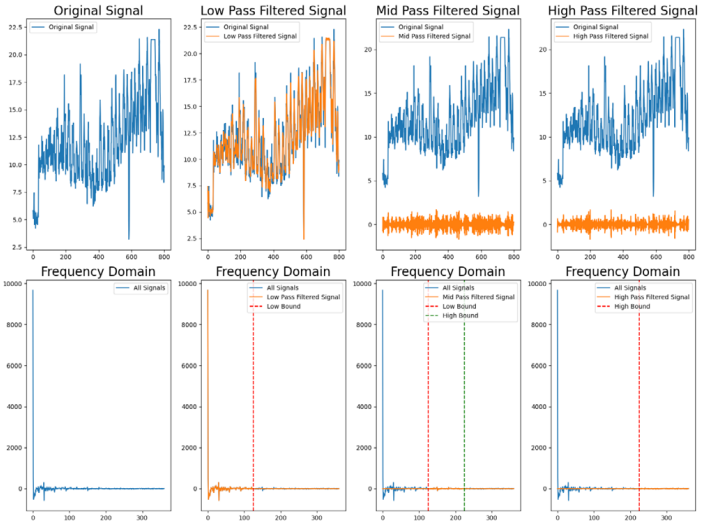

Figure 1. Temporal and frequency domain data for different filters

In our experiments, we illustrate that the entirety of the data within the frequency domain served to yield accurate prediction results. We categorized the data into the frequency bands based on the preset cutoff frequency, then implemented the Inverse Fast Fourier Transform (iFFT) to extrapolate data in those frequency bands back into the time domain. Afterwards, the process data was upsampled and concatenated via weighted sum to yield the final prediction result based on the chosen prediction window . In particular, we found that a prediction model using FITS with high-frequency data (noise) obtained a lower MSE compared to the model without it, illustrating an essential property of time series data in the frequency domain.

In summary, this new framework for analyzing time series prediction shows great potential in obtaining accurate prediction results, making it ideal for low-resource situations. In addition, our results show important properties regarding frequency domain data, revealing correspondence to those in the temporal domain, thus revealing a new view on the popular approach to the problem. For the future, further research can be done on investigating the potential of frequency-based features in the composition of seminal temporal-based features.

1. Xu, Zhijian, Ailing Zeng, and Qiang Xu. "FITS: Modeling time series with $10k$ parameters." *arXiv preprint arXiv:2307.03756* (2023).

Using Velocity-Inferred Hamiltonian Networks: Symplectic Dynamics from Position-Only Observations

Claire Yu[1], Ruichen Xu[2], Yuefan Deng[2]
[1]Germantown Friends School, Philadelphia, PA 19144, [2]Department of Applied Mathematics & Statistics, Stony Brook University, Stony Brook, NY 11790

Modeling high-fidelity dynamical systems faces challenges from high dimensionality and partial observability. Classical geometric integrators preserve invariants but are limited in capability [1]. Consequently, data-driven methods like Hamiltonian Neural Networks (HNNs) have emerged to learn physical flows and preserve structure across complex partial differential equations [2]. Conventional HNNs rely on access to positions q and momenta p, constraining their application in real-world scenarios where momentum data are unavailable [1]. To address this limitation, we introduce the Velocity-Inferred Hamiltonian Neural Network (VI-HNN), a framework that learns Hamiltonian dynamics strictly from position data by leveraging the invertibility of the momentum–velocity mapping $p = M(q)v$, with $M(q)$ a positive-definite mass matrix. This allows the Hamiltonian to be reparameterized as $H(q,v)$, enabling the use of inferred velocities, computed via finite differences, in place of canonical momenta during training while maintaining the symplectic structure foundational to Hamiltonian flow [1][2].

We provide a formal derivation establishing the equivalence between position–velocity and position–momentum representations under an invertibility assumption. Our methodology constructs a neural Hamiltonian $\widetilde{H}_\theta(q,v)$ trained on trajectories synthesized from four classical physical systems: spring–mass oscillator, simple pendulum, two-body, and three-body gravitational problems. Velocities are estimated from noisy position traces, and the network is optimized using a physics-inspired loss that enforces Hamilton's canonical equations. Comparative experiments demonstrate that VI-HNN, trained with only position observations, achieves trajectory reconstruction accuracy and energy conservation on par with HNN baselines. For all systems, VI-HNN models exhibit stable long-horizon predictions and robust conservation of energy-like invariants, as substantiated by quantitative results (Tab. 1) and trajectory analyses (Fig. 1).

System	Model	Train Loss	Test Loss	Energy
Spring–Mass	Baseline	5.32 ± 0.16	5.46 ± 0.18	0.30 ± 0.04
	HNN	4.25 ± 0.133	4.09 ± 0.14	0.030 ± 0.0015
Simple Pendulum	Baseline	20.58 ± 0.40	20.58 ± 0.40	438 ± 164
	HNN	20.9 ± 0.40	20.7 ± 0.42	187.79 ± 39.20
Two-Body†	Baseline	1.09 ± 0.036	1.03 ± 0.067	1685.0 ± 77.0
	HNN	0.73 ± 0.038	0.71 ± 0.069	1.56 ± 0.56
Three-Body	Baseline	3.79 ± 0.13	3.97 ± 0.25	95.73 ± 34
	HNN	4.53 ± 0.22	4.94 ± 0.47	0.59 ± 0.14

† Two-Body results are scaled by 10^4.

Table 1: Performance of Baseline and HNN models across four physical systems. Loss and energy values are scaled by 10^3 unless otherwise noted.

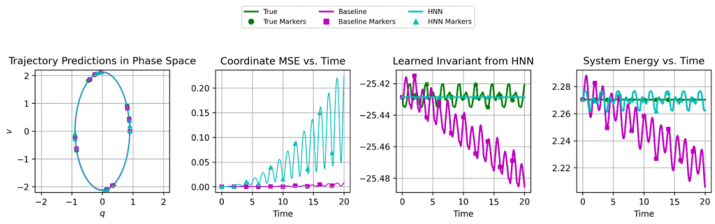

Figure 1. Comparison of baseline models and HNN on the pendulum system. HNN maintains stable trajectories and energy conservations, unlike the diverging baseline model.

Our results indicate that VI-HNN provides a mathematically principled approach for data-driven discovery of Hamiltonian structure when only position data is available. By exploiting the invertible velocity–momentum relation, our approach bridges a critical gap between theoretical modeling and experimental constraints in physics-aware machine learning. Future work may explore adaptively refined velocity approximation and more robust noise-handling approaches. Real-world deployment of physics-informed learning such as celestial mechanics and biomechanical motion highlight the importance of this position-only Hamiltonian learning.

[1] Hairer, E., Lubich, C., & Wanner, G. (2006). *Geometric Numerical Integration: Structure-preserving Algorithms for Ordinary Differential Equations* (2nd ed.). Springer.

[2] Greydanus, S., Dzamba, M., & Yosinski, J. (2019). Hamiltonian Neural Networks. *Advances in Neural Information Processing Systems, 32*, 15353-15363.

The Effect of Temperature on the Binding Dynamics Between the SARS-CoV-2 Spike Glycoprotein and Polylactic Acid Surface

Audrey Huang[1], Karin Hasegawa[2], Miriam Rafailovich[3], Yuefan Deng[2]
[1]Woodbridge High School, Irvine, CA, 92604, [2]Department of Applied Mathematics and Statistics, Stony Brook University, Stony Brook, NY 11794, [3]Department of Materials Science and Chemical Engineering, Stony Brook University, Stony Brook, NY 11790

The spike glycoprotein (S-protein) of SARS-CoV-2 protrudes from the virion and mediates host-cell entry and adsorption to surfaces. Understanding how the S-protein interacts with different surfaces can reveal the mechanisms of viral inactivation and guide the development of more effective virucidal materials. While previous studies have examined adsorption on polystyrene[1], cellulose, and graphene surfaces, we focus on the S-protein's interactions with polylactic acid (PLA), a material commonly used in personal protective equipment (PPE), food packaging, and 3D printing[2].

The structure of the S-protein was retrieved from the Protein Data Bank (PDB: 6VXX) and prepared with the CHARMM36 force field and TIP3P water model, with 15 sodium ions. Following energy minimization, the system was triplicated to test three different temperatures: 3°C (cold chain conditions), 24°C (typical indoor conditions), and 50°C (extremely hot climates). Each system underwent NVT and NPT equilibration before being merged with a similarly-prepared PLA substrate. The S-protein-PLA complexes underwent 2000 ns production runs.

To quantify the S-protein's structural changes upon adsorption, we calculated its radius of gyration (R_g), solvent accessible surface area (SASA), and volume over time. Figure 1a shows that the R_g decreased in all systems over time, indicating more compact structures caused by contact with the PLA surface. SASA and volume, indices of the protein's stability and folding state, analyses showed clear differences between the values of the S-proteins in the 3°C and 24°C systems, compared to those of the S-protein in the 50°C system, which exhibited lower SASA and volume values (Figure 1b and 1c). This result is consistent with those seen in MD simulations of the S-protein alone, without a PLA surface[3].

We found significant structural changes in the S-protein as it interacted with the PLA surface at different temperatures. Our findings could be applied to improve the development of PLA-based materials for viral capture and deactivation, contributing to the global effort against infectious diseases.

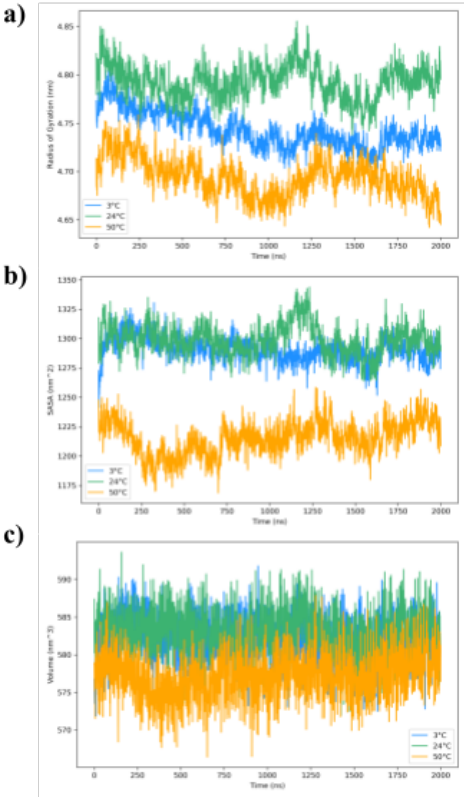

Figure 1: Time evolution of a) radius of gyration, b) SASA, and c) protein volume.

[1]Sahihi, M., & Faraudo, J. (2022). Molecular Dynamics Simulations of Adsorption of SARS-CoV-2 Spike Protein on Polystyrene Surface. *Journal of Chemical Information and Modeling, 62*(16), 3814–3824. https://doi.org/10.1021/acs.jcim.2c00562
[2]Siracusa, V., Blanco, I., Romani, S., Tylewicz, U., Rocculi, P., & Rosa, M. D. (2012). Poly(lactic acid)-modified films for food packaging application: Physical, mechanical, and barrier behavior. *Journal of Applied Polymer Science, 125*(S2), E390–E401. https://doi.org/10.1002/app.36829
[3]Niu, Z., Hasegawa, K., Deng, Y., Zhang, Z., Rafailovich, M., Simon, M., & Zhang, P. (2022). Modeling of the thermal properties of SARS-CoV-2 S-protein. *Frontiers in Molecular Biosciences, 9*. https://doi.org/10.3389/fmolb.2022.953064

Session V: Biopolymers

Chairs:

Shoumik Saha, Dezhao Meng, Sangita Das, Yiwei Fang, Kaniz Fatema

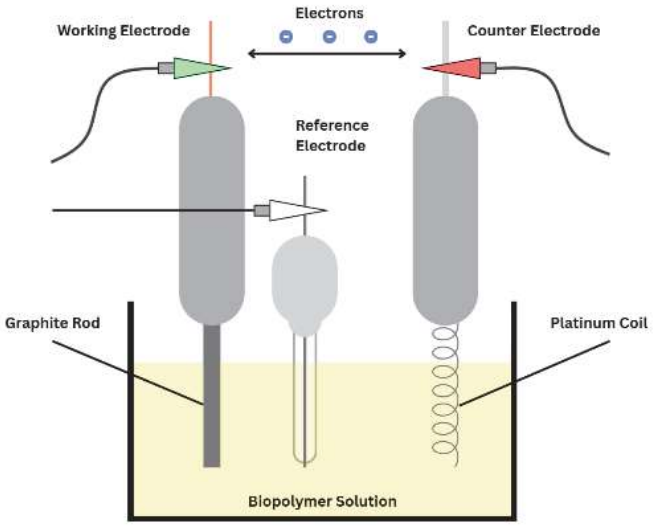

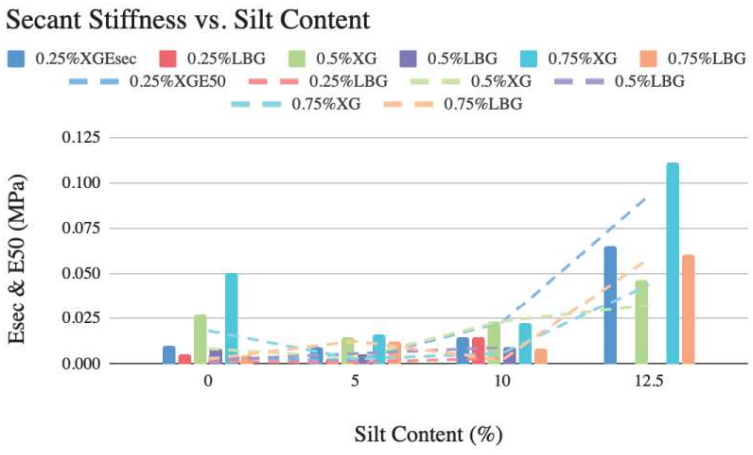

Fig 1. Secant Stiffness vs. Silt %

Mechanisms of Soil-Strengthening for Polyelectrolyte Nanocomposite Gels

Nathaniel Gao[1], Benson Chou[2], Max Xu[3], Daniel Zhou[4], Samuel Sylvia[5], Shoumik Saha[5], Dilip Gersappe[5], Miriam Rafailovich[5]

[1]Lower Merion High School, Wynnewood, PA 19096, [2]Great Neck South High School, Great Neck, NY 11020, [3]William G. Enloe Magnet High School, Raleigh, NC 27610, [4]Skyline High School, Ann Arbor, MI 48103, [5]Stony Brook University, NY 11790

Biopolymers have emerged as potential sustainable soil additives for combating soil erosion.[1] In particular, polyelectrolyte (PE) chain and nanofiller blends have been promising for enhancing soil strength and cohesion. When introduced into soil pores, clay-reinforced biopolymers form networks via physical and chemical interactions, increasing stability.[2] However, the exact molecular mechanisms and interplay of factors leading to its soil-strengthening properties remain an enigma. This study examines the structure and dynamics of PE-nanofiller composites in both equilibrium (non-shear) and non-equilibrium (shear) environments to elucidate the mechanisms leading to its unique rheology.

The molecular dynamics software LAMMPS was used to simulate both environments. Using the coarse-grained Kremer-Grest model, the system consisted of PE chains, nanofillers, solvent particles, counterions, and co-ions enclosed within periodic boundary conditions. For non-bonded interactions, Lennard-Jones and Coulombic potentials were used, while a harmonic angle style was used for the angular constraints between bonded nanofiller particles. The system was equilibrated using *nVT* and *nPT* equilibrium ensembles with thermostatting and barostatting, followed by a production run for non-shear data. The simulation box was then changed from an orthogonal to a triclinic structure to allow for tilting of the system during subsequent shear. To create the simple shear effect, a strain rate was applied via a non-equilibrium molecular dynamics (NEMD) simulation. This non-equilibrium shear environment was equilibrated using a Nose-Hoover thermostat, followed by data collection.

Analyzing the properties of gels during equilibrium, two different archetypes of polymer chains were compared: one with an $\varepsilon_{pf} = 5.0$ and the other with $\varepsilon_{pf} = 1.0$, representing varying physical attraction strengths. As shown in Figure 1, a wider distribution of R_g values is observed in Polymer B ($\varepsilon_{pf} = 5.0$), indicating a greater variation in polymer chain size. As a higher ε_{pf} leads to more stable PE-nanofiller adsorption, hence stronger 3D polymeric networks, this suggests that increased polydispersity, through factors such as enhanced cross-linking and entanglement, results in a more reinforced gel. Additionally, to quantify the nanofiller stacking behavior, stacking size and orientation via Legendre's polynomial were analyzed. The smaller nanofiller stack sizes in Polymer B (Fig. 2) suggest improved dispersion, increasing PE-nanofiller interactions and network cohesion due to larger surface area, which aligns with the increased polymeric gel strength associated with greater ε_{pf} values.

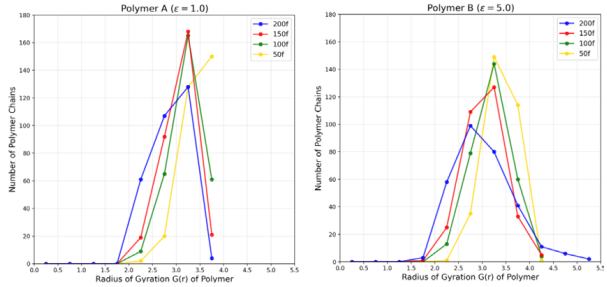

Figure 1. Polymer radius of gyration distributions with various nanofiller concentrations plotted for Polymer A and B

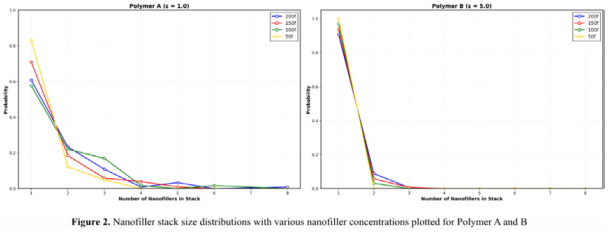

Figure 2. Nanofiller stack size distributions with various nanofiller concentrations plotted for Polymer A and B

For the non-equilibrium (shear) model, computations are anticipated to conclude in a few days; with these results, we will analyze and compare findings with the non-shear system to strengthen our understanding of the mechanisms behind PE gel properties. We hypothesize that shear thinning will occur, marked by metrics such as increased end-to-end chain distances and reduced stack alignment, as indicated by a decay in Legendre's polynomial order parameter along the shear direction.

[1] Soldo, Antonio et al. "Biopolymers as a sustainable solution for the enhancement of soil mechanical properties." Scientific reports vol. 10,1 267. 14 Jan. 2020, doi:10.1038/s41598-019-57135-x

[2] Kumar, M Ashok et al. "Enhancing durability and erosion resistance of soils with varying plasticity using crosslinked biopolymers." Scientific reports vol. 15,1 12572. 12 Apr. 2025, doi:10.1038/s41598-025-96977-6

Characterization of the Metal Absorption Capability of Rhizobium Tropici-Produced Exopolysaccharide

Alli Katila-Miikkulainen[1*], Caleb Son[2*], Talon Xing[3*], Ian Zhang[4*], Dezhao Meng[5], Sangita Das[5], Yiwei Fang[5], Miriam Rafailovich[5]

[1]*Palo Alto High School, Palo Alto, CA 94301*, [2]*Mount Hebron High School, Ellicott City, MD 21042*, [3]*North Allegheny Senior High School, PA, 15143*, [4]*Martin Luther King High School, Riverside, CA 92508*, [5]*Stony Brook University, Stony Brook, NY 11794*

**All contributed equally, listed alphabetically*

A promising strategy to absorb toxic metal ions has recently emerged from a Rhizobium tropici-produced exopolysaccharide (EPS), which was found to form a precipitate when placed in an $FeCl_3$ solution. Rhizobium tropici-produced exopolysaccharide is especially viable due to its non-toxic, environmentally friendly, and biodegradable nature. When compared to traditional methods of filtering heavy metals, EPS shows great viability; unlike traditional methods of separating iron, such as chemical precipitation, EPS does not face problems with generating unwanted sludge and requiring costly reagents.[1] Thus, this study aims to quantitatively characterize EPS and its ability to absorb metal ions for the purpose of purifying drinking water, enhancing food safety in soil, and treating wastewater.

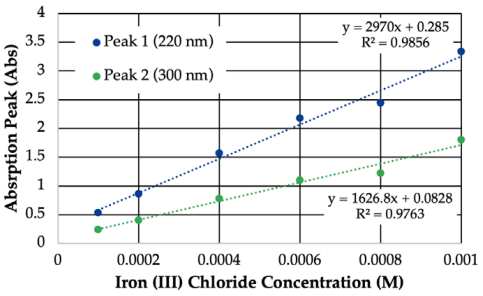

Figure 1. Calibration curves for UV-Vis absorbance peaks near 220 nm and 300 nm vs. $FeCl_3$ concentration. Linear trends were used to quantify unknown samples.

Firstly, a range of concentrations of diluted $FeCl_3$ solution in water from 0.0001 M to 0.001 M were synthesized. These dilutions were used in the UV-Vis spectroscopy machine to form a calibration curve for absorption peaks near 220 nm and 300 nm (Fig. 1). These calibration curves were then used to create a linear-regression model to predict the Fe^{3+} concentrations for molarities not measured.

Concentrations of 12, 20, 53, 108, and 163 mg/mL of EPS solution were added to 0.001 M of $FeCl_3$. Each solution was formed using a vortex mixer for 2 minutes and left to mix with a WavingShaker for 4 hours until dissolved. After mixing, the samples were spun in a centrifuge to separate iron precipitates from solution. It was noted that only the 3 mg, 12 mg, and 20 mg/mL EPS concentrations formed precipitates, while the 53, 108, and 163 mg/mL concentrations formed gels. The three precipitated solutions were filtered using a 1 mL syringe and a 0.2 µm cellulose acetate filter, leaving the filtrate to be used in UV-Vis spectroscopy.

A control of 0 mg/mL EPS in 0.001 $FeCl_3$ M was then placed into a UV-Vis spectroscopy to create a baseline for the other concentrations to be compared to. While lower mg/mL amounts of EPS added increased the iron concentrations (ex. 0.00126 M for 12/mg/mL), it can be seen that at around 20 mg/mL, the iron concentrations decreased to about 0.00080 M (Fig. 2). This result implies that higher concentrations of EPS is required to efficiently remove iron from the solution, as EPS itself contains iron.

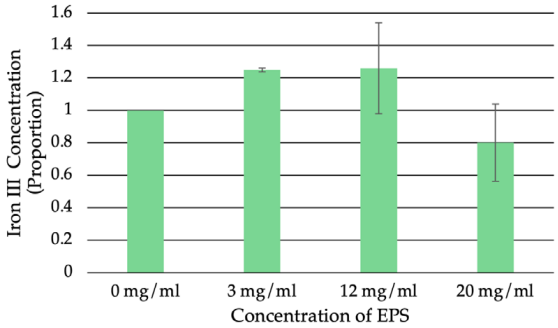

Figure 2. Iron III concentration at various concentrations of EPS biopolymer. Lower concentrations of biopolymer increase iron concentration due to iron present in EPS. Higher concentrations (20 mg/ml) show a decrease in iron content.

XRF spectroscopy was used to compare the 3 mg/mL concentration measurement and found to be in accordance. Future work includes using XRF and ICP-MS to compare and corroborate with UV-Vis and more testing is needed with different concentrations of EPS and $FeCl_3$.

[1]Qasem, N.A.A., Mohammed, R.H. & Lawal, D.U. Removal of heavy metal ions from wastewater: a comprehensive and critical review. *npj Clean Water* 4, 36 (2021)

Evaluation of the Structural and Electrochemical Properties of Extracellular Polymeric Substance Derived from *Rhizobium tropici*

Sarah Dabees[1], Michael Cuiffo[2], Miriam Rafailovich[2] [1]*Florida Gulf Coast University, Naples, FL 33965,* [2]*Stony Brook University, Stony Brook, NY 11794*

Current environmental challenges that require both sustainable and efficient solutions to combat issues such as pollution and ecosystem degradation have led to research into biopolymers as sustainable alternatives and supplements in biotechnologies [1]. The bacterium *Rhizobium tropici* is known to benefit soil health through erosion prevention, promotion of plant growth and root formation, and amplification of soil tolerance to heavy metals, pH changes, and salinity [2-3]. However, the physical and chemical properties of its derived biopolymer are not widely understood due to detection complexity in common characterization scans. A greater understanding of the properties of *R. tropici*'s Extracellular Polymeric Substance (RT-EPS) can advance future applications of this biopolymer for aspects including and beyond soil health. In this study, several tests to evaluate the structural properties of RT-EPS were conducted, including cyclic voltammetry using a three-electrode setup (**Figure 1**), UV treatments, adhesion tests using deweaved cotton fibers (**Figure 2**) and soil, and pH adjustment studies. 10 mg/mL solutions of the dialyzed biopolymer sample were treated with HCl and NaOH to reach desired pH levels of 4 and 10 to test how structural properties of the RT-EPS change under pH-stress conditions with respect to ion conductivity. Electrochemical properties (**Figure 3**) and response to pH and UV treatment observed both imply a coiled linear structure of the biopolymer, potentially with insoluble salts bound to the structure that enable redox reactivity. RT-EPS expresses surface adhesion when dry and moisture retention when saturated and likely undergoes structural changes in response to pH and electrical current. This study provides insight into the structure of RT-EPS as a naturally abundant and sustainable biopolymer for biotechnological applications regarding both its electrochemical and adhesive properties.

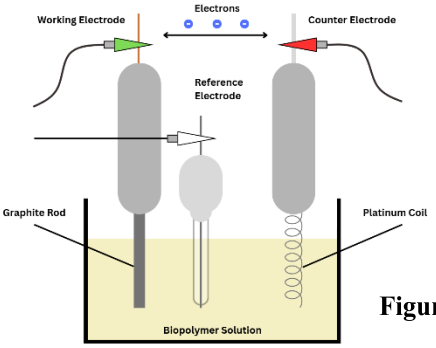

Figure 1: Three-Electrode Setup.

Figure 2: Optical microscopy of deweaved cotton fibers with biopolymer (a), UV-treated biopolymer (b), and water (c).

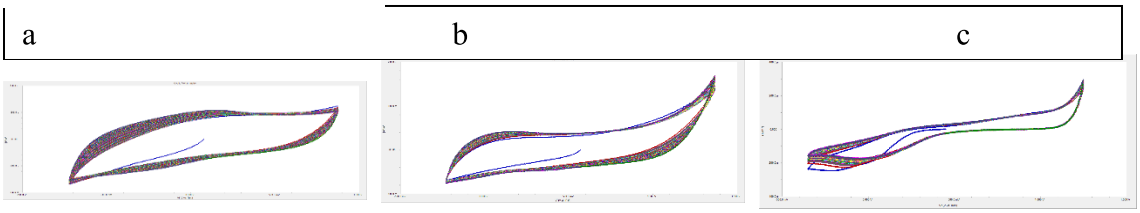

Figure 3: Cyclic voltammograms of neutral (a), acidic (b), and basic (c) biopolymer solutions at a scan rate of 10 mV/s for 200 cycles, -0.8 to 0.8 volts from open circuit potential.

[1]Jia, M., Kim, J., Nguyen, T., Duong, T., & Rolandi, M. (2021a). Natural biopolymers as Proton Conductors in bioelectronics. Biopolymers, 112(7). https://doi.org/10.1002/bip.23433

[2]Gopalakrishnan, S., Sathya, A., Vijayabharathi, R., Varshney, R. K., Gowda, C. L., & Krishnamurthy, L. (2014). Plant growth promoting rhizobia: Challenges and opportunities. 3 Biotech, 5(4), 355–377. https://doi.org/10.1007/s13205-014-0241-x

[3]Larson, S., Nijak, G., Corcoran, M., Lord, E., & Nestler, C. (2016). (rep.). Evaluation of Rhizobium tropici-derived Biopolymer for Erosion Control of Protective Berms. Environmental Security Technology Certification Program (ESTCP). Retrieved 2025.

Impact of *Rhizobium Tropici*-Produced Biopolymer on the pH of Acidic and Basic Solutions

Angel Zhu[1], Susie Yang[2], Cosmo Perfetti[3], Kaniz Fatema[3], Yiwei Fang[4], Aaron Sloutski[5], Miriam Rafailovich[4]

[1]Shenzhen Middle School, Shenzhen, China, [2]Sendelta International Academy, Shenzhen, China, [3]Stony Brook University, Stony Brook, NY 11794, [4]Department of Materials Science and Chemical Engineering, [5]Department of Oral Biology & Pathology, Stony Brook University, Stony Brook, NY 11794

Soil acidification and alkalinization have become global environmental problems. Acidification is caused mainly by human activities, including contamination from fertilizers and acid rain. Alkalization is primarily caused by agriculture, especially the irrigated cropping system.[1] Both present serious threats to the environment. To combat these rapidly growing global challenges, ethanol precipitable material (EPM) derived from extracellular polymeric substances produced by *Rhizobium Tropici*[2] was evaluated for its ability to neutralize pH under acidic and alkaline conditions with the maximum pH range of 4-10, enabling EPM to neutralize pH in most soil-systems.[3]

pH testing was conducted to assess these properties of EPM. Distilled water was adjusted to the target pH values of 4 and 10 by adding drops of hydrochloric acid and sodium hydroxide. The same volume and concentration of acid or base used in the water tests were added to EPM solutions of varying concentrations (50, 125, 250, 500 mg/L). A calibrated pH meter was used to monitor pH changes. Measurements were taken every 5 minutes for the first hour and every 30 minutes for the second hour. The results show that EPM acts quickly (over the span of a few hours), with 50 mg/L EPM appearing to offer the most effective stabilization across both pH extremes. pH readings were recorded the following day to assess long-term changes.

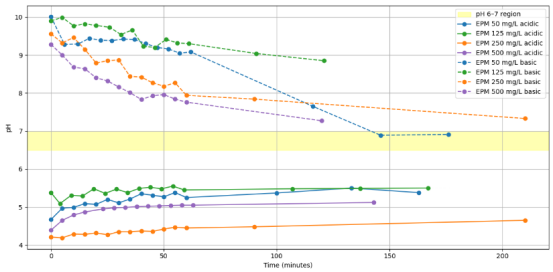

Figure 1: pH vs. Time for Various EPM Concentrations

The zeta potential of the EPM solutions was measured with a Brookhaven ZetaPALS using phase analysis light scattering. Zeta potential allows for a quantitative measurement of the charge in solution.[3] Various solutions were tested at a wide range of pH and EPM concentrations. Results are shown in Fig. 2, with a cubic fit.

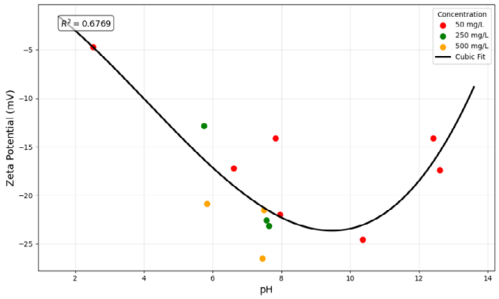

Figure 2: Zeta Potential vs. pH for Various EPM Concentrations

The pH variation over time for EPM solutions is shown in Fig. 1. All EPM concentrations displayed an upward trend in pH changes in acidic solutions and a downward trend in basic solutions, which is effective for combating soil acidification and alkalinization. 50 mg/L EPM showed the most pronounced effect in both acidic and basic conditions. The zeta potential of all solutions was negative, even in acidic solutions (Fig. 2). Future work involves investigating the presence of negative charges in highly acidic solutions to gain a better understanding of the mechanism by which EPM neutralizes solutions at pH extremes and testing the function of EPM in simulated soil conditions.

[1]Chen, C., Xiao, W., & Chen, H. Y. H. (2023). Mapping global soil acidification under N deposition. Global Change Biology, 29, 4652–4661. https://doi.org/10.1111/gcb.16813

[2]Stavi, I., Thevs, N., & Priori, S. (2021). *Soil salinity and sodicity in drylands: A review of causes, effects, monitoring, and restoration measures Frontiers in Environmental Science, 9*, 712831. https://doi.org/10.3389/fenvs.2021.712831

[3]*Queensland Government. (n.d.). Soil pH levels. Queensland Government. https://www.qld.gov.au/environment/land/management/soil/soil-properties/ph-levels*

[4]Lunardi CN, Gomes AJ, Rocha FS, De Tommaso J, Patience GS. Experimental methods in chemical engineering: Zeta potential. Can J Chem Eng. 2021; 99: 627–639. https://doi.org/10.1002/cjce.23914

Rhizobium Tropici-Produced Biopolymer Impact on Water Evaporation and Sublimation

Christian Chan[1], Ella Li[2], Jay Gao[3], Aaron Sloutski[4], Marcia Simon[5], Miriam Rafailovich[4]

[1]South Side High School, Rockville Centre, NY, 11750, [2]Lexington High School, Lexington, MA, 02421, [3]Stony Brook University School of Dental Medicine, Stony Brook, NY 11794, [4]Department of Materials Science and Chemical Engineering, [5]Department of Oral Biology & Pathology, Stony Brook University, Stony Brook, NY 11794

In the modern day, global climate change and unsustainable industrial practices have ushered in an era of unpredictable and extreme weather events, causing eutrophication, decreased biodiversity, and desertification of farmland. Additionally, with the prevalence of overtilling, monocultural agriculture, and irresponsible irrigation practices, soil erosion is on the rise, with the world losing "half a percent of arable soil every year."[1] To combat the rapidly deteriorating condition of arable soils worldwide, an extracellular polymeric substance (EPS) produced by *Rhizobium Tropici* was tested for its ability to stabilize soil through mechanical interactions with the soil and indirect soil stabilization through upregulation of root-associated genes.

This biopolymer, called Ethanol Precipitable Material (EPM), is characterized by its ability to sequester nutrients and enhance subterranean root structures. Due to its erosion-resistant properties, EPM offers promising applications in sustainable agriculture and environmental preservation in the face of increasingly volatile weather patterns. Based on its ability to aggregate soil particles as a biopolymer, we hypothesized that EPM would increase the water-retention capabilities of soil. To test EPM's ability to buffer water loss in different temperatures, EPM-impregnated sand and EPM-solution samples (in concentrations of 100mg-EPM/kg-Sand and 250mg-EPM/kg-Sand, respectively) were left to evaporate in temperatures of 23°C, 4°C, -20°C, and -80°C. Although both the EPM and control samples in all temperatures reached similar final water levels, their evaporation trajectories differed significantly. The EPM samples in 23°C showed no significant effect on water levels. But in the first 24 hours in 4°C, EPM sand and liquid samples evaporated at half the rate of the control and interestingly, evaporated at a constant rate, as opposed to the control, which lost water at a progressively slower rate over time (see *Figure. 1*). The EPM samples in 4°C indicate potential for applications in plant transport and future experiments requiring controlled water loss. The samples in -20°C, however, performed similarly to the control. Notably, the liquid EPM samples in -80°C lost 1000 times less water than the control in the first 24 hours, indicating EPM's resistance to water loss in subzero conditions. Interestingly, the EPM-impregnated sand sample in -80°C performed the same as the control. The liquid -80°C samples' resistance to water loss compared with the relatively less extreme buffering capabilities of the lower temperatures indicate that EPM's interactions with water are highly temperature dependent. Additionally, EPM's interactions with water in liquid samples don't seem limited to a specific phase as the EPM samples in 4°C showed a two-fold decrease in water loss, while the 23°C samples had no apparent effect, regardless that both were in the liquid phase. The same is true for the -80°C liquid samples, which lost 1000x less water than the -20°C, again regardless of the shared phase of water. More testing is necessary to ascertain the role of temperature in EPM's interactions with water.

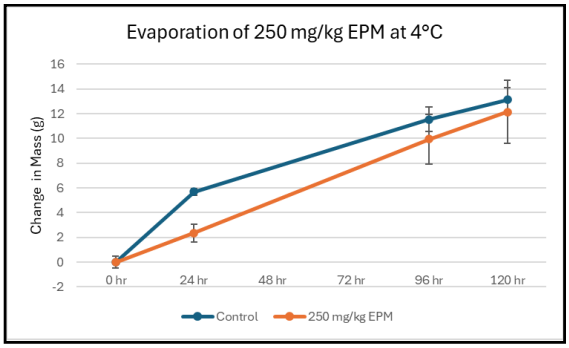

Figure 1. Cumulative water loss in liquid EPM samples at 4°C.

As the mechanism of temperature with respect to EPM's water retention is largely unknown, this study provides insight into how EPM acts as a natural protectant in nature and can provide potential solutions for stabilizing soils in extreme climates.

The authors would like to thank the US Army Corps of Engineers (ERDC) and the Louis Morin Charitable Trust for their support (W912HZ-20-2-0054) in this research.

[1]Grantham, J. (2018). The Race of Our Lives Revisited [pdf]. *GMO White Paper*. https://www.gmo.com /globalassets/articles/white-paper/ 2018/ jg_morningstar_race-of-our-lives_8-18---short-version.pdf

Stabilization of Silty Sand Using Xanthan Gum, Locust Bean Gum, and *Rhizobium Tropici* Biopolymer

Evan Liu[1], Damien Crowley[2], Yiwei Fang[3], Kaniz Fatema[3], Miriam Rafailovich[3]

[1]*Lynbrook High School, San Jose, CA 95129,* [2]*Stanford University, Stanford, CA 94305*

[3]*Department of Materials Science and Chemical Engineering, Stony Brook University, Stony Brook, NY 11794*

Biopolymers have recently emerged as effective sustainable materials in soil binding, useful for combating erosion and strengthening soil. Traditional methods, such as cement or lime, raise significant environmental concerns [1]. Cement has been found to affect the pH of soil and groundwater, and extensive carbon dioxide emissions are generated from its production [1]. This study investigates the effect of xanthan gum (XG), locust bean gum (LBG), and an ethanol precipitable material (EPM) derived from Rhizobium Tropici produced extracellular polymeric substances (EPS), three environmentally friendly biopolymers, on the stabilization of silty sand.

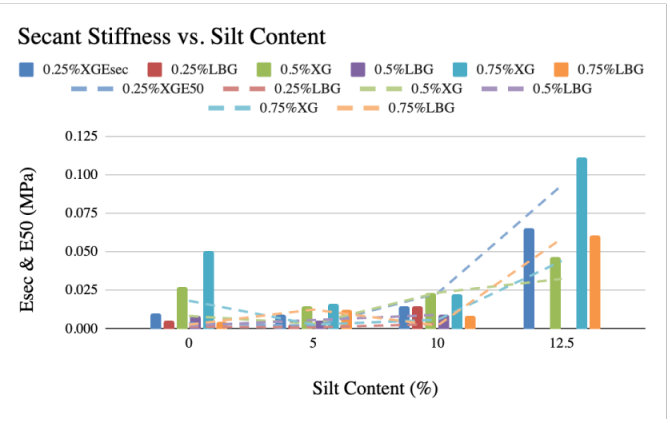

Fig 1. Secant Stiffness vs. Silt %

Samples were produced at eight silt concentrations (0%, 5%, 10%, 20%, 30%, 50%, 70%, and 100%) and cured for five different lengths of time (1 day, 2 days, 3 days, 7 days, 14 days). To produce the samples, a total of 110 grams of sand and silt were mixed along with 16mL of biopolymer solution for silt samples and 20mL for sand samples. Biopolymer concentrations were 0.25, 0.50, and 0.75 wt% in solution for XG and LBG, and 125mg/L for EPM (0.0125 wt%). Samples were mixed in a THINKY ARE-250 for 80 seconds, compacted into column molds (68mm in height and 34mm in diameter) and manually pressed out.

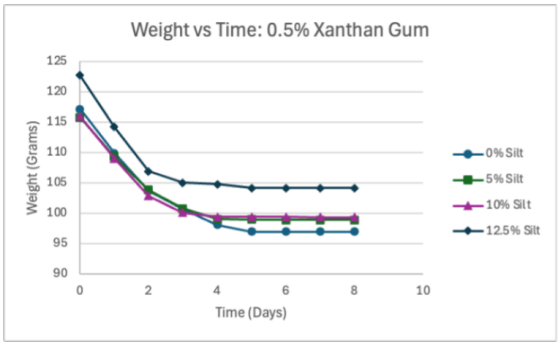

Fig 2. Wt vs Time: 0.5% XG

Unconfined compression strength (UCS) testing was done on an Instron 5542 and thermogravimetric analysis on a TA Instruments TGA 550. Scanning electron microscopy (SEM) and X-ray micro-computed tomography (MicroCT) imaging were conducted to show the binding of biopolymer within the samples and particle size and shape. Samples were weighed daily to test the rate of evaporation of samples. TGA samples were isothermaled at 40 degrees centigrade for 10 minutes to ensure evaporation of remaining water, then ramped to 500 degrees. XG, LBG, and EPM generally degrade around 300-400 degrees.

Secant stiffness generally increases as silt concentration increases, as shown in Fig 1. UCS and stiffness follow the same trend. Thermogravimetric analysis (TGA) shows potential core-shell formation in pure sand but not silt containing samples. The samples made with water appear to dry after 2 days, EPM and LBG dry after 3, and XG (fig 2) dries after 5 days. Further testing is necessary on samples with a shorter curing time; specifically, UCS for 2-day and 3-day samples and dry columns. Additionally, unconsolidated undrained (UU) triaxial testing will be performed on dry 0% and 10% silt samples and continued TGA to verify the formation of a shell-core structure.

[1] Chang, I., Lee, M., Tran, A. T., Lee, S., Kwon, Y.-M., Im, J., & Cho, G.-C. (2020). Review on biopolymer-based soil treatment (BPST) technology in Geotechnical Engineering Practices. Transportation Geotechnics, 24, 100385. https://doi.org/10.1016/j.trgeo.2020.100385

Session VI: Brain Aneurysm Models

Chair:

Robert Wong, Aaron Sloutski

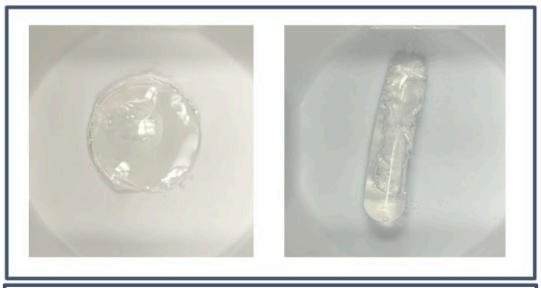

Figure 1: 20% PVA-MA UV crosslinked with Irgacure 651. 3D disk (left), 3D tube (right).

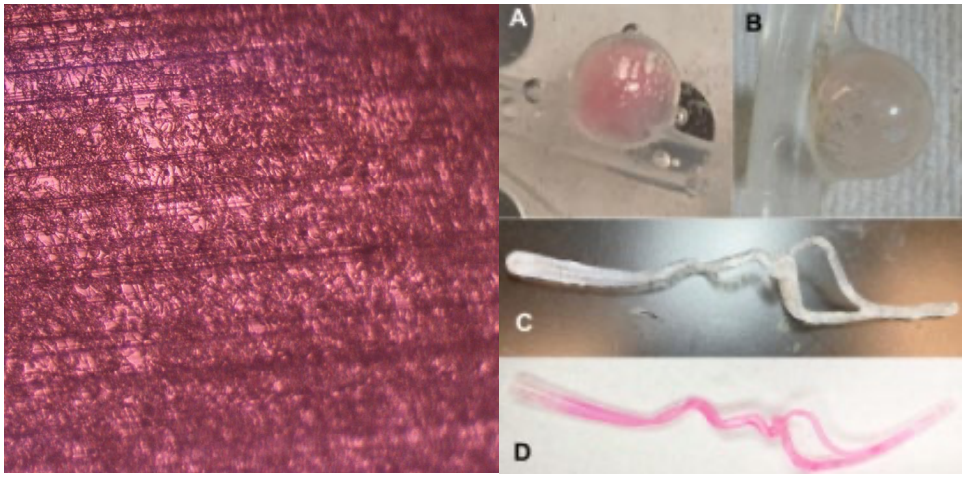

Engineering UV-crosslinked Poly(vinyl alcohol)-based Vascular Graft and Brain Aneurysm Models

Rachel Lee[1], Jashmin Gill[2], Aaron Sloutski[3], Robert Wong[3], Chander Sadasivan[4], Miriam Rafailovich[3]
[1]Palos Verdes Peninsula High School, Rolling Hills Estates, CA 90274, [2]Stony Brook University, Stony Brook, NY 11794, [3]Department of Materials Science and Chemical Engineering, Stony Brook University, Stony Brook, NY 11794, [4]Department of Neurological Surgery, Stony Brook University Medical Center, Stony Brook, NY 11794

Brain aneurysms are focal dilations in the brain's vascular system which can prompt hemorrhagic stroke or death if ruptured. To improve treatment methodology, modeling of complex aneurysm geometries both *in vitro* and *in vivo* allows for a clearer understanding of aneurysm behavior tailored for each patient [1, 2]. Poly(vinyl alcohol) (PVA) demonstrates promising potential for use in vascular graft construction and brain aneurysm modeling due to its biocompatibility and tunable mechanical properties [2]. Chemical crosslinking is known to induce enhanced mechanical characteristics but is limited by its time-consuming procedure and inconsistent results. Thus, by developing a methodology for efficient 3D-printing of PVA through ultraviolet (UV) crosslinking, PVA-based grafts and models can become significantly more accessible and applicable. This study aims to engineer an effective procedure of UV crosslinking for 3D-printing and characterize material properties for production optimization.

PVA was reacted with isocyanatoethyl methacrylate (IEMA) to form PVA-MA [3]. To identify if the polymer was capable of crosslinking, ammonium persulfate (APS) and tetramethylethylenediamine (TEMED) were mixed with 10%, 15%, and 20% PVA-MA. Once proving its feasibility, the focus was shifted to UV crosslinking to study future directions with 3D-printing. UV-initiated crosslinking was conducted with photoinitiators Irgacure 2959 and Irgacure 651. To determine the applicability of this methodology while examining the impact of various concentrations of PVA-MA, 3D-printed disks were fabricated using 10%, 15%, or 20% PVA-MA (Figure 1). Oscillatory amplitude sweeps were performed to assess the stability and shear modulus (elastic component) of each sample. The gel disks exhibited superior mechanical stability and structure maintenance as PVA concentration increased (Figure 2).

Figure 1: 20% PVA-MA UV crosslinked with Irgacure 651. 3D disk (left), 3D tube (right).

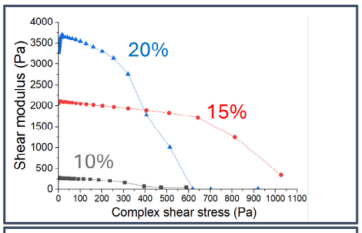

Figure 2: Complex shear stress (Pa) vs. shear modulus (Pa) for 10%, 15%, and 20% PVA-MA with Irgacure 2959.

Crosslinked gels were researched for their durability in aqueous medium. Analysis of the samples' minimal changes in water uptake demonstrate stability and represent the desired mechanical characteristic of water swelling resistance. The process of developing 3D disks through UV-initiated crosslinking was then applied to engineering 3D tubes using glass rods (Figure 1). The qualitative structural integrity of the various samples suggests that the 20% PVA-MA mixed with Irgacure 651 crosslinked through UV develops more stable 3D gel tubes compared to other combinations.

The results indicate significant advancements in UV crosslinking methodology and demonstrate potential for further production of vascular grafts and aneurysm models following additional analysis and characterization of UV-based crosslinking mechanical properties. Future studies will focus on biocompatibility studies and fine-tuning of the mechanical properties, both by changing PVA:IEMA ratio and by utilizing different UV-based crosslinking techniques, aiming at producing 3D-printed models at a later stage.

[1] Andaluz N, Zuccarello M (2011). Treatment strategies for complex intracranial aneurysms: review of a 12-year experience at the university of cincinnati. Skull Base. 21(4):233-42.
[2] Conconi, M. T., et al. (2014). Evaluation of Vascular Grafts Based on Polyvinyl Alcohol Cryogels. Molecular Medicine Reports
[3] Goldvaser, M et al (2022). Poly(vinyl alcohol)-methacrylate with CRGD peptide: A photocurable biocompatible hydrogel. Journal of tissue engineering and regenerative medicine, 16(2), 140–150

Optimizing Material Properties of a Pluronic Hydrogel Blend for Brain Aneurysm Treatment

Chetas Aduri[1], Josh Feigenbaum[2], Rosalie Liu[3], Aaratrika Mondal[4], Yeji Son[5], Alessandro Verona[6], Wendy Yu[7], Robert Wong[8], Aaron Sloutski[8], Chander Sadasivan[9], Miriam Rafailovich[8]

[1]*Ames High School,* [2]*South Side High School,* [3]*Westview High School,* [4]*Wayzata High School,* [5]*American School of Guatemala,* [6]*American School of Milan,* [7]*Guangdong Country Garden School,* [8]*Department of Materials Science and Chemical Engineering, Stony Brook University, NY, 1179,* [9]*Department of Neurological Surgery, Stony Brook University Medical Center, Stony Brook, NY 11794*

Current brain aneurysm treatments involve permanent implantation of metal devices or liquid embolic agents (LEA) at the aneurysm site, which leads to unfavorable primary outcomes in at least 20% to 30% of cases on average.[1] This study uses a novel hydrogel to form an injectable, crosslinked coil to fill aneurysms with greater range for high-risk locations and morphologies. The hydrogel consists of Pluronic F88 functionalized with dimethacrylate (FDMA) and crosslinked with ammonium persulfate (APS) and tetramethylethyldiamine (TEMED). But FDMA contracts significantly, so this project incorporated pure F88 to reduce crosslinking, creating microholes, and subsequently optimized the material properties including stability, strength, and biocompatibility of the FDMA-F88 blend for brain aneurysm treatment.

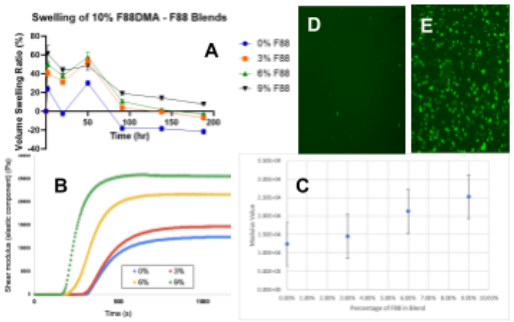

Figure 1: A) Swelling over time as % change in volume B) Longitudinal change in elastic modulus for best samples of each blend C) Graph showing the average of the last 50 values of figure B (stabilizing of gel elasticity,) error represented by standard deviation of points (spread) D) Day 4, 6% F88 E) Day 4, control

To monitor gel swelling, spherical gels with 10% FDMA and 0%, 3%, 6%, and 9% F88 were incubated in 37°C saline water. The volume of all concentrations increased initially, then decreased to a constant level as the F88 leached out from the microholes. Adding F88 successfully reduced the shrinking property of FDMA, with 6% F88 being best suited for the aneurysm treatment due to having close to 0% net volume change (Fig. 1A).

To investigate the mechanical properties of the gels, a rheological study involving a temperature/time sweep was conducted on blends containing 10% FDMA with varying concentrations of F88 (0%, 3%, 6%, and 9%). This revealed crosslinking dynamics and gel mechanical strength. Overall, blends with higher F88 concentrations demonstrated stronger and faster cross-linking with higher elastic modulus, indicating greater stiffness and resistance to deformation. (Fig. 1B). The 6% and 9% F88 blends showed both high shear modulus and the fastest crosslinking times, making them the most promising concentrations.

To assess cell adhesion, 10% FDMA – 0%, 2%, 6% F88 blends were formed, cut, and placed into 24-well plates before HUVEC EGPF cells were plated onto the gels, cultured, and imaged on days 1, 4, and 7. (Fig. 1C-D). Cells exhibited low confluency and rounded morphology across all F88 concentrations whereas the control exhibited normal cell growth, meaning the blends are noncytotoxic and not inherently cell-adhesive. This is beneficial to avoid excessive proliferation within the aneurysm.

In conclusion, the 10% FDMA-6% F88 gel is the optimal blend due to non-cytotoxicity, low swelling, and strong rheological properties. Future work to implement this gel will further the available treatments of brain aneurysms.

[1]Deshmukh, A. S., et al. (2024). The management of intracranial aneurysms: Current trends and future directions. Neurology International, 16(1), 74–94. https://doi.org/10.3390/neurolint1601000

Optimizing Injection Procedure of Pluronic Hydrogel Blends for Study of Brain Aneurysms

Chetas Aduri[1], Josh Feigenbaum[2], Rosalie Liu[3], Aaratrika Mondal[4], Yeji Son[5], Alessandro Verona[6], Wendy Yu[7], Robert Wong[8], Aaron Sloutski[8], Chander Sadasivan[9], Miriam Rafailovich[8]

[1]*Ames High School,* [2]*South Side High School,* [3]*Westview High School,* [4]*Wayzata High School,* [5]*American School of Guatemala,* [6]*American School of Milan,* [7]*Guangdong Country Garden School,* [8]*Department of Materials Science and Chemical Engineering, Stony Brook University, NY, 1179,* [9]*Department of Neurological Surgery, Stony Brook University Medical Center, Stony Brook, NY 11794*

Current brain aneurysm treatments have recurrence rates of 20.8%.[1] To improve treatment outcomes, this injection procedure utilizes a biphasic injection that starts as a liquid agent in a syringe but crosslinks inside a catheter, resulting in hydrogel coils to fill aneurysms with diverse morphologies. The injection procedure involves two injection phases separated by a wait time for crosslinking. For the hydrogel, pluronic F88 was functionalized with methacrylate (FDMA) and crosslinked with ammonium persulfate (APS) and tetramethylethyldiamine (TEMED). But pure FDMA contracts significantly over time, F88 is added to aid in stronger rheological properties and control swelling. This project identifies the ideal gel composition and optimizes the injection procedure.

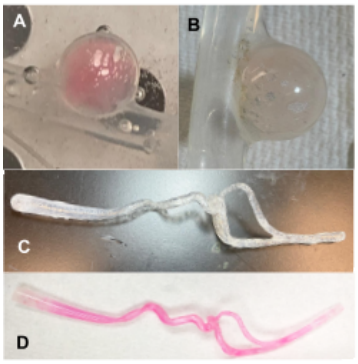

Figure 1: A) Gel in model aneurysm day of injection B) Gel in model aneurysm left overnight C) Dip-coated silicone vessel D) Vessel dyed for hydrogel coating

10% FDMA – 0% F88 and 10% FDMA– 6% F88 were tested in a silicone aneurysm model for injectability. It is critical to get a consistent procedure to ensure correct timing of the crosslinking. The optimal injection rate was determined to be 0.1 mL/min for the 0% blend and 0.15mL/min for the 6% blend, and the wait time between the injection phases was determined to be 2 minutes 45 seconds for both blends. The gels were kept in the aneurysm model overnight under a flow loop at 10 mL/sec, and both blends remained in the aneurysm model, demonstrating stability (Fig. 1A-B). The 6% blend was more promising due to its distinct stages of injection.

The packing density of the coil was determined by measuring the volumes of the inside of the aneurysm and the coil within the aneurysm. After the volumetric measurements, the packing density was determined to be 93.5%, establishing that the aneurysm was adequately loaded with coil. The coil used for the packing density experiment was the 10% FDMA - 6% F88 gel, showing that 6% F88 is the optimal blend for the prevention of blood flow in the aneurysm.

For the upcoming in-vivo experiment to test this procedure, vessels were created for practice injections in-vitro. An aneurysm mold was 3D-printed with acrylonitrine butadiene styrene and dipcoated with silicone to form a vessel (Fig. 1C). This was coated with acrylamide coating that is crosslinked under UV light, meant to mimic the surface of a blood vessel for catheter injection. When stained, it shows a consistent hydrogel coating that verifies the technique, which is reliable for in-vivo studies (Fig. 1D).

Overall, 10% FDMA-6% F88 gel is the ideal blend for smooth injections. The gel is stable within the in-vitro model, and with proper cooling, injection rates, and wait times, injections are possible without unwanted crosslinking. Ongoing experiments are exploring injection pressure further, and future steps include improving vessel stability and in-vivo testing in surgical conditions. Ultimately, the goal is to create a successful aneurysm treatment to improve patient outcomes.

[1]dos Santos., et al. (2015). Survival Analysis of Risk Factors for Major Recurrence of Intracranial Aneurysms after Coiling. Canadian Journal of Neurological Sciences / Journal Canadien Des Sciences Neurologiques, 42(1), 40–47. doi:10.1017/cjn.2014.126

Polymer-based Flow Diverter Systems for Endovascular Embolization

Danielle Lu[1], Juwon Kim[2], Phoebe Zheng[3], Krystal Lazo[4], Aaron Sloutski[3], Fernando Aguilar-Perez[3], Robert Wong[3], Chander Sadasivan[5], Miriam Rafailovich[3]

[1]South Side High School, Rockville Centre, NY, 11550, [2]Seoul Academy, Seoul, Republic of Korea, 06200, [3]Department of Material Science and Chemical Engineering, Stony Brook University, Stony Brook, NY, 11794, [4]Suffolk County Community College, [5]Department of Neurological Surgery, Stony Brook University Medical Center, Stony Brook, NY, 11794

Brain aneurysms are localized dilation in the wall of cerebral blood vessels which, upon rupture, can lead to severe neurological damage. Flow diverters (FDs), unlike traditional clipping or coiling, offer a less invasive and more durable solution by redirecting blood flow to promote aneurysm thrombosis and vessel remodeling. Their performance, however, depends on material properties such as biocompatibility, flexibility, and endothelial support. By guiding blood flow along the parent vessel and enabling the formation of a neointimal layer, FDs ultimately seal off the aneurysm from circulation.[1] The aim of this research was to develop a biocompatible polymeric system for FD stents. Conventional stents are typically 20%–30% metal; instead, polymers such as phosphorylcholine can be integrated to the structure to provide versatility and biocompatibility.[2] An ideal polymer must be biocompatible, mechanically strong, and exhibit shape-memory properties—the ability to return to a pre-defined shape when exposed to stimuli like heat.

Electrospinning is an ideal way to achieve fibers with the flexibility and structural integrity needed for flow diverter stents. Polycaprolactone (PCL), a thermoplastic polymer, is semicrystalline, flexible, and elastic, allowing it to mimic soft body tissues. Polylactic acid (PLA), which is strong and stiff, is suitable for holding shape and bearing loads, and is often blended with other materials—like PCL—to improve its toughness and flexibility. In the developed polymers, PCL will act as the switching segment due to its relatively low melting temperature, whereas the PLA and the crosslinked junctions will act as the net points, holding the structure and enabling shape memory transition. Combining both will yield a flow diverter that is strong yet flexible, long-lasting but biodegradable, and safe to use inside the human body.

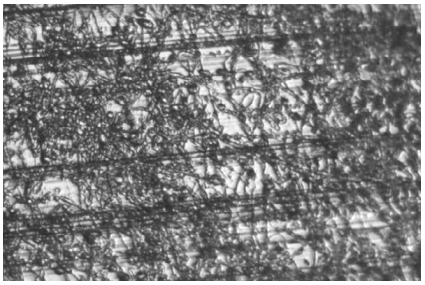

Figure 1. 10x Microscopy image of *PPG4K-PCL 60 dissolved in 100% chloroform, electrospun at 20mL/min.*

For this research, PPG-PCL copolymers were synthesized and end-capped with double bonds for future crosslinking. As the study progressed, longer polymers were synthesized to create more crystalline chains, leading to more favourable fiber formation, leading to stronger and flexible structure suitable for flow diverters. NMR and FTIR results validated the synthesis, with peaks indicating the presence of double bonds and CL units. For each polymer, samples were made with either a 20% or 25% polymer concentration and 4 different solvents: 100% chloroform, 9:1 and 3:1 ratios of chloroform to ethanol, and a 4:1 ratio of dichloromethane to dimethylformamide. To fine-tune fiber properties, parameters (voltage, distance, and flow rate) were adjusted during the electrospinning process.

Keyence microscopy was used to analyze fiber formation and structure (Figure 1). DSC and XRD were used to study crystalline formation in the polymers before and after electrospinning. XRD samples showed well-defined peaks consistent with crystalline domains. IR and NMR spectroscopy were also conducted to confirm the presence of double bonds and estimate the molecular weights of the synthesized polymers.

Future work will focus on synthesizing PLA/PCL based copolymers followed by electrospinning studies, where the different parameters, such as flow rate, voltage, or needle size, will be fine-tuned, aiming at achieving optimized fiber formation. Chosen composition will be further developed for 3D printing of flow diverter stents.

(1) Briganti, F.; Leone, G.; Marseglia, M.; Mariniello, G.; Caranci, F.; Brunetti, A.; Maiuri, F. Endovascular Treatment of Cerebral Aneurysms Using Flow-Diverter Devices: A Systematic Review. *Neuroradiol. J.* **2015**, *28* (4), 365–375. https://doi.org/10.1177/1971400915602803.

(2) Hudson, J. S.; Lang, M. J.; Gross, B. A. Novel Innovation in Flow Diversion. *Neurosurg. Clin. N. Am.* **2022**, *33* (2), 215–218. https://doi.org/10.1016/j.nec.2021.11.004.

Thermal Shape-Memory Polymer for Mechanical Severance of Injected Polymer in Brain Aneurysm Treatments

Kevin Qiu[1], Ishmeet Singh[2], Christopher Wang[3], Connor Zhao[4]
Bandari Chen[5], Leonard Johnson[5], Aaron Sloutski[5], Robert Wong[5], Chandramouli Sadasivan[5], Miriam Rafailovich[5]

[1]Wayzata High School, Plymouth, MN 55446, [2]Stockdale High School, Bakersfield, CA 93311, [3]Solon High School, Solon, OH 44139, [4]North Hollywood High School, North Hollywood, CA 91601, [5]Department of Materials Science and Chemical Engineering, Stony Brook University, Stony Brook, NY 11790

A brain aneurysm occurs when a blood sac forms in the brain, significantly increasing the risk of stroke or seizure if ruptured. Modern treatments for brain aneurysms can involve occluding inflow to the sac, promoting thrombosis through endovascular coil embolization, or redirecting blood flow via flow-diverting stents. The injection of a biodegradable polymer into the aneurysm sac is one such way to prevent rupture[1]. However, this polymer frequently adheres to the catheter tip, increasing the risk of vascular damage when the catheter is removed. To address this issue, a novel biocompatible shape memory polymer (SMP) network was synthesized that is actuated at physiological temperatures and can be integrated within the catheter tip to induce mechanical severance, thereby preventing unwanted adherence of the embolic agent.

SMPs, which change shape upon stimulus, contain two distinct phases: net points, permanently fixed with chemical bonds, and switching segments, which undergo a phase transition and deform under stimulus[2]. Thus, once an environmental trigger is activated (temperature, pH etc), the polymer can be deformed and quickly fixed into a temporary shape. Upon restimulation, the polymer relaxes into its original shape. The SMP was synthesized with varying numbers of caprolactone (CL) units as the switching segments copolymerized on polypropylene glycol (PPG) blocks, followed by end-capping with 2-isocyanatoethyl methacrylate (IEMA). NMR spectroscopy and IR spectroscopy confirmed the chemical composition of the formed macromer. The polymers were then crosslinked with benzoyl peroxide and N,N-dimethyl-p-toluidine (DMPT) to form 3D constructs for further studies.

Crosslinking efficiency analysis by washing the samples with tetrahydrofuran (THF) indicated efficiency of 90% and higher. DSC and XRD analyses were conducted to study the crystalline formation and track the changes with growing PCL segments, as well as a closer insight on the step-by-step of the shape memory cycling. Once enough data was collected to understand the polymers, shape memory cycles were conducted at a 3D tube construct (Figure 1) showing promising fixity and recovery rates, vital for efficient shape memory behavior.

The polymers will be further adjusted chemically to exhibit the most suitable shape memory behaviour while presenting sufficient mechanical properties for implementation on catheter tips. Cell studies will be conducted to validate the biocompatibility of the polymers and finally, 3D structures will be printed and their gel-cutting transition, mediated by the shape memory movement, will be investigated as the temperature triggering will be enabled by incorporating ferromagnetic particles[3].

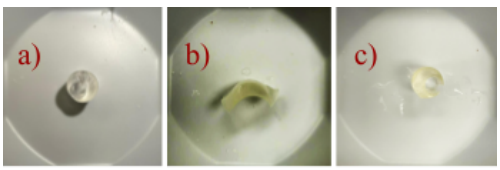

Figure 1: a) Original SMP b) Deformed SMP c) Reset SMP

[1]Wong, R., Sloutski, A., Gopal, M., Dashti, N., Li, J., Rai-Gersappe, D., Pandey, I., Guo, J., Tsai, E., Freychet, G., Peselev, Z., Cohn, D., Sadasivan, C., & Rafailovich, M. (2024). Engineering a biopolymer for vascular embolization based on fundamental polymer principals. *Polymer, 309*, 127437.

[2]Lendlein, A., & Gould, O. E. C. (2019). Reprogrammable recovery and actuation behaviour of shape-memory polymers. *Nature Reviews Materials, 4*(2), 116–133.

[3]Cohn, D., Zarek, M., Elyashiv, A., Sbitan, M. A., Sharma, V., & Ramanujan, R. V. (2021). Remotely triggered morphing behavior of additively manufactured thermoset polymer-magnetic nanoparticle composite structures. *Smart Mater. Struct., 30,* 045022.

Session VII: Biomechanics and Biomedical Devices

Chairs:

Hugh Rosshirt, Shi Fu

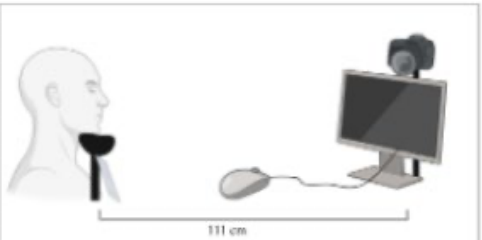

Figure 1: The DISC recording setup. The camera and monitor are located 111 cm away from the chinrest. The participant was instructed to click on Waldo using the mouse. The mirror on the chinrest allows for cross reference of when the *Where's Waldo* image switches on the monitor, confirming the participant found Waldo.

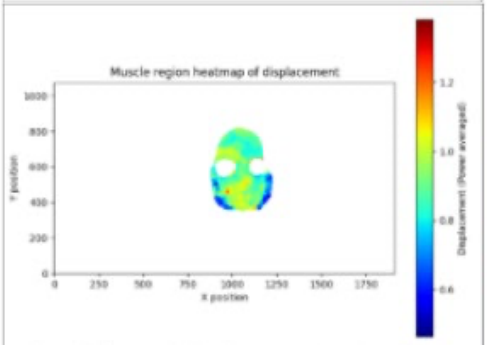

Figure 2: Averaged displacement of confused state for participant across 4 s. Active regions are seen on the eyebrows and near the mouth.

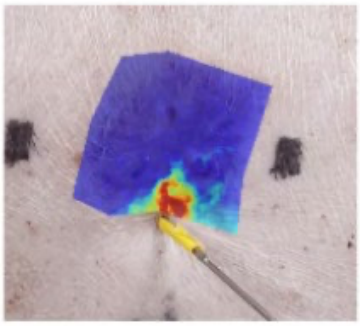

Figure 2. Resulting heat map after running DISC on a poked pig burn wound

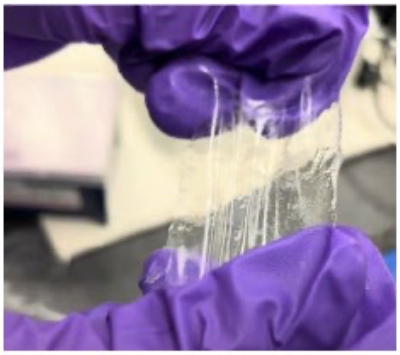

Expression Detection from *Where's Waldo* Using Digital Image Speckle Correlation (DISC)

Kiara Yoon[1], Ryan Gu[2], Catherine Ji[3], Lemi Gao[4], Chloe Shim[5], Chloe Yim[6], Spark Zhao[7], Briman Yang[8], Shi Fu[8], Miriam Rafailovich[8]

[1]Palo Alto High School, Palo Alto, CA, [2]Westwood High School, Austin, TX, [3]New Trier High School, Winnetka, IL, [4]Dulwich College Beijing, Beijing, China, , [5]Hong Kong International School, Hong Kong, [6]William A. Shine Great Neck South High School, Great Neck, NY, [7]BASIS International School Guangzhou, Guangzhou, China, [8]Department of Materials Science and Chemical Engineering, Stony Brook University, Stony Brook, NY

Digital markers, data-based indicators derived from digital sources, have been a point of interest in detecting emotional states and understanding human health. More specifically, assessing facial muscle movements in response to visual stimuli can aid in clinical diagnoses of neurodegenerative and neuromuscular disorders. One such technique is Digital Image Speckle Correlation (DISC), a noninvasive method that measures facial muscle activity by tracking skin pore displacement.[1]

Prior research has demonstrated that DISC can detect asymmetrical facial enervation patterns in clinical populations, such as patients with Bell's Palsy.[2] However, there still remains a need to validate DISC's utility in tracking real-time emotional states during complex visual tasks. The image searching game, *Where's Waldo*, presents an ideal, controlled challenge that elicits dynamic mental states—*confusion*, *excitation*, and *realization*—in rapid succession. Analyzing this DISC data characterizes normative reaction patterns and allows for potential recognition of atypical facial responses in individuals with neurodegenerative conditions.

In this study, 35 participants played *Where's Waldo* across four levels of increasing difficulty. Facial movements were recorded using a Canon EOS 60D camera mounted 111 cm away from participants (Fig. 1). DISC then analyzed participant muscle activity during the three distinct emotion states. Displacement heatmaps were generated to visualize regions of muscle activation, while mean displacement over time was quantified and compared to a reference frame captured from each participant's initial neutral expression.

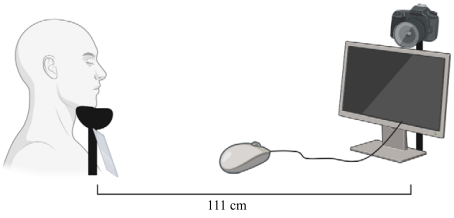

Figure 1: The DISC recording setup. The camera and monitor are located 111 cm away from the chinrest. The participant was instructed to click on Waldo using the mouse. The mirror on the chinrest allows for cross reference of when the *Where's Waldo* image switches on the monitor, confirming the participant found Waldo.

Here, DISC successfully characterized facial muscle activity across the three defined stages of playing *Where's Waldo*. Heatmap comparison during the *confusion* states, four seconds preceding participant's click on finding Waldo, revealed consistent activation in facial regions centered around the eyebrows and mouth across participants (Fig. 2). Analysis of mean facial displacement over time showed a prominent peak immediately before the Where's Waldo level progressed, demonstrating a pattern of increased facial movement, or excitation, while locating Waldo (Fig. 3). Additionally, a smaller but distinct peak was observed immediately after the image switch, indicating an *affirmation* response in which participants confirmed their successful identification of Waldo.

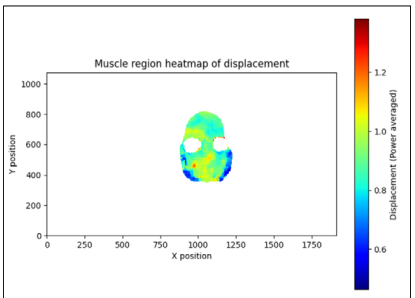

Figure 2: Averaged displacement of confused state for participant across 4 s. Active regions are seen on the eyebrows and near the mouth.

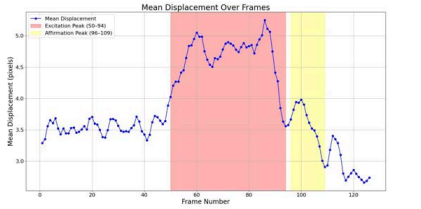

Figure 3: Prominent peak shown in red, showing excitation stage from finding Waldo before participant affirms that their selection was correct (frame 94). Additional affirmation peak shown in yellow.

These findings represent further developments for DISC to understand trends in human expression and reaction. Observed temporal and spatial patterns of muscle activation provide insight into underlying cognitive and affective processes, such as attentional engagement, visual recognition, and satisfaction upon task completion. To ensure DISC's broader clinical relevance, further analysis of patients with neurodegenerative disorders is necessary to validate its utility as a noninvasive diagnostic tool. In addition, reaction times can be quantified by measuring the number of frames between peaks associated with confusion and realization. Future studies with larger sample size are needed to better capture individual facial expression and enhance generalizability of these findings.

[1] Saadon, J. R., Yang, F., Burgert, R., Mohammad, S., Gammel, T., Sepe, M., Rafailovich, M., Mikell, C. B., Polak, P., & Mofakham, S. (2023). Real-time emotion detection by quantitative facial motion analysis. 18(3), e0282730–e0282730. https://doi.org/10.1371/journal.pone.0282730
[2] Fu, S., Polak, P., Fiore, S., Passman, J. N., Davis, R., Manu, L. M., & Rafailovich, M. (2025). Digital Image Speckle Correlation (DISC): Facial Muscle Tracking for Neurological and Psychiatric Disorders. Diagnostics, 15(13), 1574. https://doi.org/10.3390/diagnostics15131574

Porker Poker: Developing a Noninvasive Method to Measure Tensile Metrics Using Digital Image Speckle Correlation (DISC)

Andy Jiang[1], Chloe Shim[2], Chloe Yim[3], Spark Zhao[4], Jerry Gu[5], Hugh Rosshirt[6], Shi Fu[7], Miriam Rafailovich[7]

[1]Stuyvesant High School, New York, NY 10282, [2]Hong Kong International School, Hong Kong 999077, [3]William A. Shine Great Neck South High School, Great Neck, NY 11020, [4]BASIS International School Guangzhou, Guangzhou, China 510515, [5]Princeton International School of Mathematics and Science, Princeton, New Jersey, [7]Department of Mechanical Engineering, Stony Brook University, NY 11790, [7]Department of Materials Science and Engineering, Stony Brook University, NY 11790

Wound healing monitoring is essential to assess treatment efficacy. Traditional wound healing diagnosis relies on invasive biopsy, which often causes great pain to the patients and is often time-consuming when sampling. To address these limitations, a poking device was designed that facilitates non-invasive wound assessment using Digital Image Speckle Correlation (DISC), an algorithm that measures pore structure displacement across captured photos[1]. The device analyzes skin deformation under an applied force, empowering elastic deformation analysis between wounded and normal skin.

The goal of the poker design was to generate consistent mechanical force across different skin samples, allowing accurate DISC measurements of elastic deformation and making it a reliable and portable instrument for tracking wound recovery. This project also evaluated pig burn wound healing, comparing a poking device combined with DISC to traditional biopsy methods.

The device consists of a GoPro camera with a dual-casing mechanism designed using Autodesk Fusion 360. The outer casing houses the camera and electronics, while the inner casing contains a spring-loaded mechanism that enables controlled force application (Figure 1). When pressure is applied to the inner casing by the screw driver, it compresses the spring at a predetermined force threshold and triggers the camera to take a second photo after the initial is taken by pressing the button. This force was verified to be 3 newtons using a Goyojo Digital Force Gauge. To streamline this process, the GoPro was hotwired to connect in parallel to the mechanical triggering system.

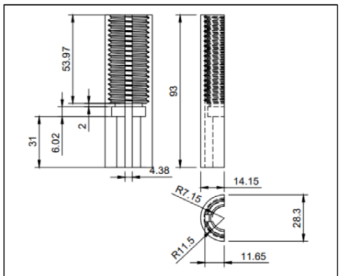

Figure 1. Engineering drawing of the final outer casing CAD design

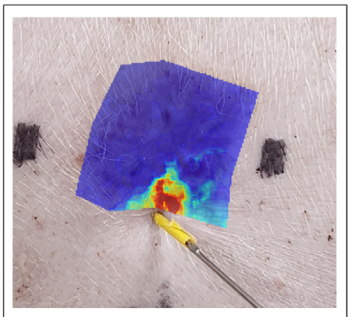
Figure 2. Resulting heat map after running DISC on a poked pig burn wound

In addition, this project evaluated the efficacy of using a poking device with DISC as an alternative to invasive evaluation methods such as biopsies (Figure 2). Analyzing data from a study testing recell treatments on pig burn wounds, DISC found there to be no significant difference in restoration of mechanical property between the 24 and 48 hour treatments, identical to results produced by the biopsies.

Future improvements on the device would include an interchangeable casing mechanism for variable levels of force and software integration for efficient DISC analysis. This design demonstrates great potential for clinical deployment with minimal training, making wound healing analysis more consistent and less invasive.

In summary, the poker system enables the standardized application of mechanical force, capturing clinical-level images for DISC-based wound monitoring. By facilitating non-invasive and consistent data collection, this tool enhances the accuracy and efficiency of wound healing analysis.

---

[1] Staloff, Isabelle Afriat, et al. "An in Vivo Study of the Mechanical Properties of Facial Skin and Influence of Aging Using Digital Image Speckle Correlation." *Skin Research and Technology*, vol. 14, no. 2, 27 July 2007, pp. 127-34, https://doi.org/10.1111/j.1600-0846.2007.00266.x.

Supercritical CO2-Mediated Decellularization of Human Dermis Samples

Lemi Gao[1], Ryan Gu[2], Catherine Ji[3], Kiara Yoon[4], Briman Yang[5], Shi Fu[5], Miriam Rafailovich[5]
[1]Dulwich College Beijing, Beijing, China, [2]Westwood High School, Austin, TX, [3]New Trier High School, Winnetka, IL, [4]Palo Alto High School, Palo Alto, CA, [5]Department of Materials Science and Chemical Engineering, Stony Brook University, Stony Brook, NY 11790

Decellularization is a prominent technique in regenerative medicine, enabling the creation of acellular scaffolds for skin grafts. These scaffolds retain the structural and biochemical properties of the extracellular matrix (ECM) while minimizing immune rejection upon implantation. Among emerging decellularization methods, supercritical carbon dioxide ($scCO_2$) has gained attention as a non-toxic, efficient alternative. With gas-like diffusivity and liquid-like solvating ability, CO_2 effectively penetrates tissue and dissolves cellular material while maintaining ECM architecture.[1] Its mild critical point (31°C, 1070 psi) makes it suitable for biologically sensitive tissues. However, due to the nonpolar nature of CO_2, polar components such as cell nuclei may remain, necessitating the use of polar cosolvents like isopropyl alcohol (IPA) or ethanol (EtOH). Additionally, the rate of depressurization can significantly impact ECM integrity, underscoring the importance of optimizing $scCO_2$ processing conditions for scaffold preservation.[2]

Engineered human dermis samples were treated with $scCO_2$ using the Spe-ed SFE Basic machine (Applied Separations). Tissue samples were loaded into mesh containers inside a 100 stainless steel milliliter vessel, stabilized by surrounding polypropylene wool to prevent movement during processing. A range of experimental conditions were evaluated to determine optimal decellularization parameters, including cosolvent type (EtOH or IPA), cosolvent concentration (70% or 100%), sample pretreatment method (fresh, freeze-dried, or frozen), flow type (continuous flow via outlet or rapid depressurization via vent), and the number of treatment cycles. To assess decellularization efficacy, 4',6-diamidino-2-phenylindole (DAPI) staining was performed after each trial to visualize nuclei. The successful removal of nuclear material served as a key indicator of effective cellular component elimination as the nucleus is the largest and most structurally resilient organelle.[3]

DAPI staining revealed that EtOH is a more effective cosolvent than IPA for cellular removal in dermis samples. Fresh samples, compared to freeze-dried or frozen, showed fewer visible nuclei, supporting their use as a preferred pretreatment. Additionally, longer treatment times of at least two hours combined with a continuous flow system instead of venting further decreased cell density. Singular cycles showed incomplete removal of nuclei, but repeating $scCO_2$ cycles improved results. Optimal results were seen after fresh samples were placed for cycles of 30 minutes of closed-system soaking and 30 minutes of continuous flow with six milliliters of 100% EtOH as cosolvent followed by three hours of soaking and three hours of continuous flow with five milliliters of 70% EtOH. The samples were then rocked for 60 hours and exhibited significant reduction in cellular remnants after DAPI staining (Fig. 1). The 2-cycle sample (Fig. 1B) shows visibly fewer nuclei compared to the control (Fig. 1A), and the transmitted light view (Fig. 1C) confirms intact tissue.

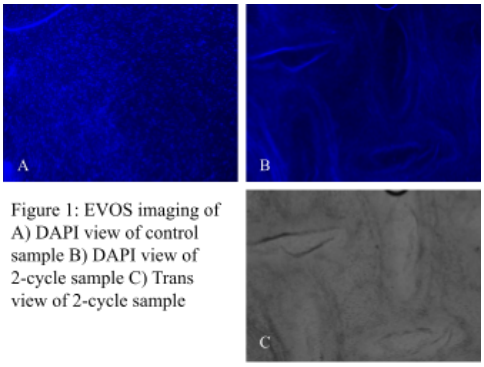

Figure 1: EVOS imaging of A) DAPI view of control sample B) DAPI view of 2-cycle sample C) Trans view of 2-cycle sample

$scCO_2$ shows promise for decellularization of dermal tissues when paired with varying concentrations of EtOH cosolvent, fresh pretreatment, and extended treatment times with cycles. Future directions include further optimizing cycle durations, scanning electron microscopy for structural analysis, redesigning sample containers to improve $scCO_2$ flow, and conducting *in vivo* experiments to evaluate immunoresponse.

[1] Gilpin, A., & Yang, Y. (2017). Decellularization Strategies for Regenerative Medicine: From Processing Techniques to Applications. BioMed research international, 2017, 9831534. https://doi.org/10.1155/2017/9831534
[2] Neishabouri, A., Soltani Khaboushan, A., Daghigh, F., Kajbafzadeh, A. M., & Majidi Zolbin, M. (2022). Decellularization in Tissue Engineering and Regenerative Medicine: Evaluation, Modification, and Application Methods. Frontiers in bioengineering and biotechnology, 10, 805299. https://doi.org/10.3389/fbioe.2022.80529
[3] Crapo, P. M., Gilbert, T. W., & Badylak, S. F. (2011). An overview of tissue and whole organ decellularization processes. Biomaterials, 32(12), 3233–3243. https://doi.org/10.1016/j.biomaterials.2011.01.057

Build and Design of a Page Turner Based on Proportional Integral Derivatives (PIDs)

Jerry Gu[1], Andy Jiang[2], Spark Zhao[3], Susie Yang[4], Hugh Rosshirt[5], Miriam Rafailovich[5]

[1]Princeton International School of Mathematics and Science, Princeton, New Jersey, [2]Stuyvesant High School, New York, NY 10282, [3]BASIS International School Guangzhou, Guangzhou, China 510515, [4]Sendelta International Academy, Shenzhen, China 518000, [5]Department of Mechanical Engineering, Stony Brook University, NY 11790

Paralysis affects nearly six million patients in America, with a significant portion of those patients struggling to perform daily tasks. For many patients, simple tasks like reading can feel insurmountably difficult. Current solutions, such as exoskeletons, aimed to facilitate those tasks, but often run into high costs, portability problems, and high power draw amongst other issues, thus demanding for cheaper alternatives. In such, our project aimed to provide a convenient, low-cost, and easy solution for some daily functions, with a particular emphasis on turning pages.

To achieve this, we used the DOBOT® Magician, a versatile robotic arm that provides precise, repeatable movements, ideal for automating tasks like turning pages, as our mechanical framework. A custom-designed, 3D-printed module was to the robot's arm to physically interact with the pages. To ensure accuracy and responsiveness, we incorporated a PID controller that helps optimize precision during repetitive tasks.

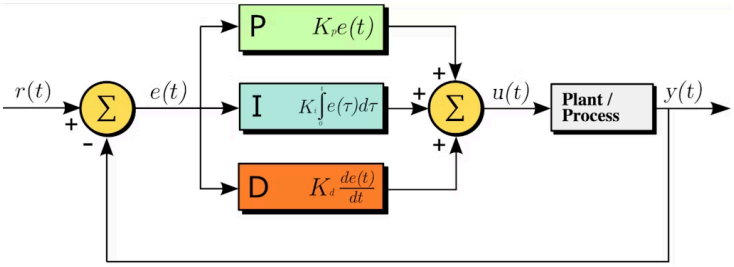

In the future, we plan on transitioning to a tendon based hand design for optimal multipurposed functionality. Another key development is tongue actuation, which would allow users to control the page-turning mechanism using their tongue for added ease of use and less strain on critical regions. To accommodate for the added components, an Automatic transmission based gearbox will also be implemented for better control over the fingers and a more efficient minimal motor design. These advancements will help ensure that the project can address a variety of needs, making daily life more accessible for those affected by paralysis.

1. *What is a PID controller?*. Data Acquisition | Test and Measurement Solutions. (2025, April 6). https://dewesoft.com/blog/what-is-pid-controller
2. DOBOT. (n.d.). Magician Robot. DOBOT Magician | Desktop Grade Robot For Advanced Education. https://www.dobot-robots.com/products/education/magician.html

Reverse Thermo-Responsive Polymer-Based Systems for Bioadhesive Applications

Cleo Xu[1], Amanda Salanitri[2], Sam Specht[3], Aaron Sloutski[4], Miriam Rafailovich[4]
[1]Phillips Academy Andover, MA, 01810, [2]University of Connecticut, CT, 06269, [3]Duke University, NC, 27708,
[4]Stony Brook University, NY 11794

The reverse-thermo responsive phenomenon describes the behavior of polymers for which, when in aqueous solution, the viscosity increases with temperature due to micelle formation.[1] One of the most studied polymers exhibiting this feature is the Pluronic polymers, and mainly F88 and F127. Such behavior allows these biopolymers to facilitate the transport of drugs in the bloodstream and act as a protective barrier for superficial wounds.[2] However, these hydrogels currently lack the adhesiveness essential for the aforementioned biomedical applications. This research proposes the solution of adding polysaccharides, pectin (Pc) and methyl amide pectin (MPc), into the synthesized polymer solutions and characterizing the mechanical and chemical properties of the modified hydrogels for future applications in the biomedical field.[3] The initial step was synthesizing chain-extended polymers from the commercially available F88 and F127 polymers. Infrared Spectroscopy confirmed the formation of urethane bonds in the synthesized polymer. Solutions of F88, F127, PF88, and PF127 dissolved in distilled water were made at 10%, 15%, 20%, and 25% concentrations. The PF hydrogels were then diluted at 10% with 1% polysaccharide solutions. Storage modulus was researched by rheometer as the temperature increases from 5°C to 45°C. PF88 and PF127 demonstrated a significantly higher increase in viscosity and a clearer transition from liquid to gel states in comparison to F88 and F127, where gelation only occurred at the highest concentrations and only for F127. Polysaccharide solutions exhibited less micelle formation than the PF88 and PF127 solutions. Differential Scanning Calorimetry confirmed this result, and additionally showed that polysaccharide solutions have a higher transition temperature and enthalpy compared to the F and PF solutions (Figure 1). To study the durability of gels in the presence of water, gravimetrical changes over time were recorded. The PF solutions held about 48 hours, which was 12 times longer than the F solutions. To model the time it takes for hydrogels to solidify on human skin, gelation ex vivo studies were conducted (Figure 2). Pictures of the hydrogels on synthesized skin strips were taken at different time intervals, which were then analyzed using ImageJ. Across all tests, the PF88 and PF127 demonstrated distinct gelation with more micelle formations compared to F88 and F127. Though the Pc and MPc were observed to inhibit micellar formations to an extent, the RTR features were maintained and showed satisfactory gelation results. In the future, polysaccharide concentration will be adjusted to optimize the adhesiveness of the hydrogels. Applying biopolymers on animal skin could model how they operate on human wounds, and investigating polymer interactions in biological environments could evaluate their compatibility as an injectable material.

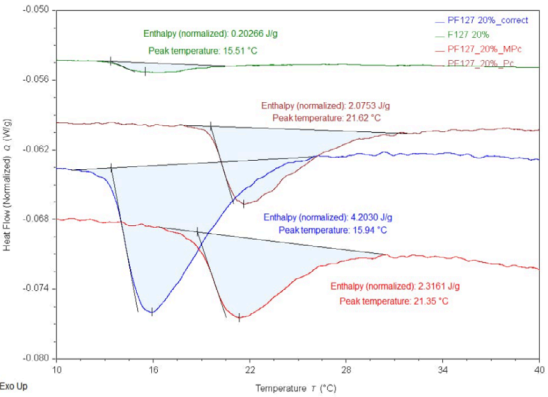

Figure 1. DSC data of F127, PF127, PF127 with Pc and MPc [20%]

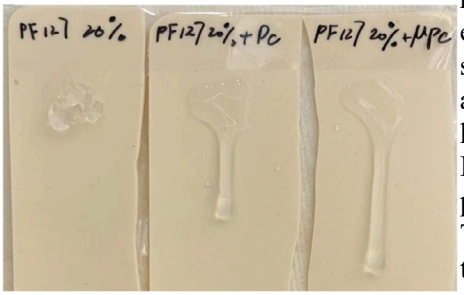

Figure 2. Gelation study PF127 and PF127 with Pc and MPc [20%]

[1] Cohn, Daniel et al. "Improved reverse thermo-responsive polymeric systems." *Biomaterials* vol. 24,21 (2003): 3707-14. doi:10.1016/s0142-9612(03)00245-x.

[2] Alexandridis, Paschalis, and T. Alan Hatton. "Poly(ethylene Oxide) poly(propylene Oxide) poly(ethylene Oxide) Block Copolymer Surfactants in Aqueous Solutions and at Interfaces: Thermodynamics, Structure, Dynamics, and Modeling." *Colloids and Surfaces A: Physicochemical and Engineering Aspects*, vol. 96, nos. 1-2, Mar. 1995, pp. 1-46, https://doi.org/10.1016/0927-7757(94)03028-x.

[3] Zheng, Yifan, et al. "Functional Adhesion of Pectin Biopolymers to the Lung Visceral Pleura." *Polymers*, vol. 13, no. 17, 2 Sept. 2021, p. 2976, https://doi.org/10.3390/polym13172976.

Spreadable Poly(tetramethylene ether)glycol/Poly(ε-caprolactone)-Based Crosslinkable Polymer for Biomedical Applications

Yicheng Zhang[1], Xuehan Fan[2], Mengdi Xie[2], Lingjie Pan[3], Aaron Sloutski[4], Fernando Aguilar Perez[4], Miriam Rafailovich[4]

[1]The High School Affiliated to Renmin University of China, Beijing, China, [2]The Experimental High School Attached to Beijing Normal University, Beijing, China, [3]Department of Chemistry, Stony Brook University, Stony Brook, NY 11794, [4]Department of Materials Science and Chemical Engineering, Stony Brook University, Stony Brook, NY 11794

Polymeric materials play a crucial role in biomedical engineering, including the development of flexible sheets for drug delivery systems and tissue interfaces. This study aims to develop a polymer that can be spread on the skin while maintaining mechanical strength and structure integrity, with potential applications in sustained topical drug delivery. To achieve this, poly(tetramethylene ether) glycol (PTMG) was selected for its flexibility and low melting point,[1] which facilitates spreading on skin and partial solidification at body temperature; and polycaprolactone (PCL) for its biocompatibility, well-documented bio-adhesion properties in tissue engineering. Isocyanatoethyl methacrylate (IEMA) was incorporated to introduce double bonds that allows crosslinking, a process that reduces crystallinity and hardens the polymer. While increasing the PCL content hinders the PTMG crystallization, as the PCL segments become longer, they begin to exhibit their own tendency to crystallize.[3] By tuning the PTMG:PCL ratio, it was aimed to achieve a balance between spreadability, melting temperature, tensile strength and crystallinity to produce a polymer suitable for skin-based biomedical applications.

PTMG-$(PCL_x)_2$-$(DMA)_2$ was synthesized through a two-step reaction process. PTMG was used as the main polymeric segment with which PCL oligomers of varying lengths (x = 0, 3, 6, 10) were synthesized, followed by end-capping with IEMA. The formed polymers were then melted (Figure 1a) and mixed with a photoinitiator solution (Irgacure 651 in NMP). The mixture was crosslinked under UV light to form thin films (Figure 1b), which were subsequently washed in acetone.

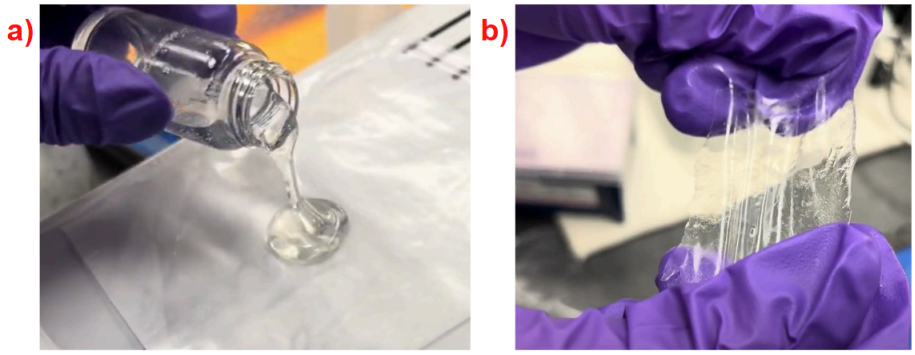

Figure 1: a) Spreading of PTMG-$(PCL_3)_2$-$(DMA)_2$; b) Crosslinked polymer film demonstrated resistance to manual stretching.

NMR and IR were used to confirm the formation of the polymer and the crosslinking. XRD patterns of crosslinked samples revealed a broad diffraction peak in all samples, indicating that the polymers were predominantly amorphous. As the PCL content increased, crystallinity initially decreased due to the suppression of PTMG chain ordering, but then increased as longer PCL chains began to crystallize independently. Similarly, DSC measurements showed a decrease in melting enthalpy with increasing PCL content.

Future studies will focus on rheology analysis on the non-crosslinked polymers followed by tensile testing on the crosslinked polymer sheets. These tests will help determine the optimal balance between melting temperature and mechanical strength, where also different 3D geometries will help assess the applicability of the gels. Drug release studies will explore the possibility of incorporation of active ingredients in the spreadable polymers. Once an optimal formulation will be designed, cell toxicity will be studied, followed by initial studies on *ex vivo* and *in vivo* animal models.

[1] Wu, S.; Zhang, Y.; Han, J.; Xie, Z.; Xu, J.; Guo, B. Copolymerization with Polyether Segments Improves the Mechanical Properties of Biodegradable Polyesters. ACS Omega 2017, 2 (6), 2639–2648. https://doi.org/10.1021/acsomega.7b00517.

[2] He, Y.; Chen, J.; Rafique, I.; Lu, Z. Star-Shaped Polycaprolactone Bearing Mussel-Inspired Catechol End-Groups as a Promising Bio-Adhesive. European Polymer Journal 2020, 139, 110025. https://doi.org/10.1016/j.eurpolymj.2020.110025.

[3] Yun-Kyu;Kwak, Y. Effects of Physical Properties on Waterborne Polyurethane with Poly(Tetramethylene Glycol) (PTMG) and Polycaprolactone (PCL) Contents. Polymer(Korea) 2016, 29 (1), 81–86.

Session VIII: PLA Blends and Composites

Chair:

Akash Ranjan Pati, Sangita Das, Dezhou Meng

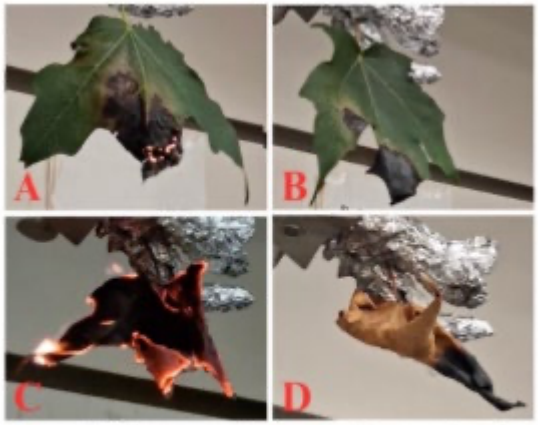

Figure 1. Sugar maple leaves 5 seconds after flame was removed: fresh uncoated (A), fresh coated (B), dry uncoated (C), dry coated (D).

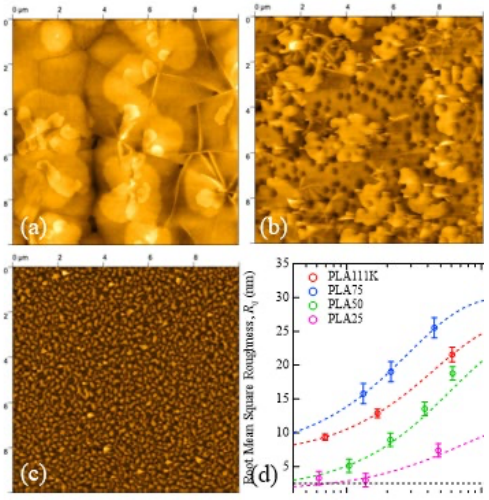

Figure 1. AFM topographic image of PLA111K (a) 61nm, (b) 17nm and (c) 6nm. (d) Thickness dependent of root mean square roughness (R_q).

Eco-friendly Phosphorus-Based Flame Retardant Formulations for Wildfire Prevention in Vegetation

Ishita Bafna[1], Emily Do[2], Danica Stout[3], Tabarjah Neal[4], Akash Ranjan Pati[4], Miriam Rafailovich[4]

[1]Enloe High School, NC 27610, [2]The Brearley School, NY 10028, [3]Montclair High School, NJ 07042, [4]Department of Materials Sciences & Chemical Engineering at Stony Brook University, NY 11790

Phosphorus-based flame retardants (PFR) have been increasingly common to combat wildfires as toxicity concerns surrounding brominated FRs have increased. PFRs can act in both the solid phase, forming a char layer between fuel and oxygen needed to sustain a flame, and in the gas phase, removing free radicals to slow burning.[1] This study aims to formulate an effective, non-toxic PFR for vegetation to reduce the spread of forest fires.

FR solutions were prepared using four ingredients to enhance fire resistance in foliage. Resorcinol bis(diphenyl phosphate) (RDP) works as a FR in the solid and gas phases,[1] while ammonium polyphosphate (APP) also works in the solid phase.[2] Lactide monomer (LM) was used to bind APP and RDP, providing an additional char layer.[3] Additionally, Brij-35 surfactant was added to improve the dispersion of the hydrophobic components of RDP within the solution. Different solutions were prepared by considering various concentrations of RDP and Brij-35; however, 5% APP, 2% RDP, 3% LM, and 0.25% Brij-35 (wt%) were selected due to FR performance.

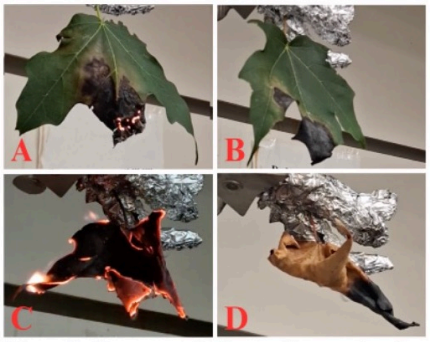

Figure 1. Sugar maple leaves 5 seconds after flame was removed: fresh uncoated (A), fresh coated (B), dry uncoated (C), dry coated (D).

Initially, the burning test (Figure 1A-D) was conducted on both coated and non-coated fresh and dry sugar maple leaves. The solution was sprayed and allowed to dry completely. A standardized flame was administered to control and treated samples for 12 seconds, and the subsequent duration of sustained flames and embers were recorded for each test. Both dry and fresh uncoated leaves sustained flames for ~20 seconds and embers for ~120 seconds (Figure 1A, 1C), while the coated leaves self-extinguished within ~5 seconds (Figure 1B, 1D).

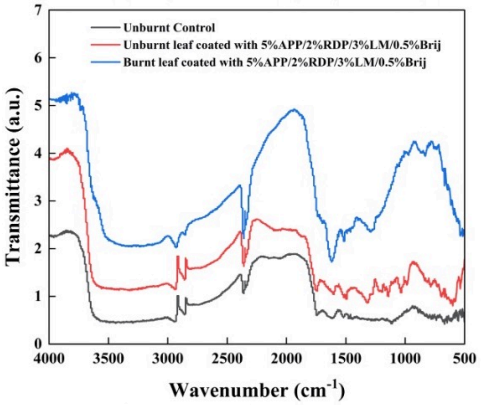

Figure 2. FT-IR spectra of unburnt control, Unburnt coated and burnt coated leaves

Various characterizations were performed to evaluate the effectiveness of the PFR coatings. FTIR analysis (Figure 2) of unburnt sugar maple leaves coated with FR showed clear chemical changes compared to uncoated leaves. Broader O–H stretching (~3300 cm^{-1}), a distinct ester C=O peak (~1750 cm^{-1}), and strong phosphate-related bands (~1250–950 cm^{-1}) confirmed successful deposition of FR components. Increased aromatic signals (~1600 and 980 cm^{-1}) indicated RDP integration. After combustion, P=O, P–O–C, and aromatic peaks in coated leaves were retained, indicating a stable, phosphorus-rich char layer that enhances thermal resistance. Contact angle measurements showed that the FR solution with Brij-35 had a low angle of 21±2°, compared to 45±3° without it. This indicates that Brij-35 lowers surface tension, improving spreadability and uniform coverage on leaves. To test the effect of the FR on vegetation, green bean plants were sprayed, and growth was tracked. The visual observation of the plants showed no physical change and continued growth after FR treatment. Overall, the proposed FR formulation shows promising results for wildfire prevention. Future work should aim to enhance dispersion stability of the solution, understand the cytotoxicity of the FR, and compare efficacy across different types and species of vegetation.

[1]van der Veen, I., & de Boer, J. (2012). Phosphorus FRs: properties, production, environmental occurrence, toxicity and analysis. *Chemosphere*, *88*(10), 1119–1153.

[2]Lim et al. (2015). A review of application of ammonium polyphosphate as intumescent FR in thermoplastic composites. *Composites Part B: Engineering*, 84, 155-174.

[3]He et al. (2017). Biodegradable, flame retardant wood-plastic combination via in situ ring-opening polymerization of lactide monomers. *Journal of Wood Science*, 63, 154-160.

Development of Graphene-Enhanced Biodegradable Polymer Nanocomposites for Conductive Applications

Alli Katila-Miikkulainen[1*], Caleb Son[2*], Talon Xing[3*], Ian Zhang[4*], Christian Apostol[5], Sangita Das[5], Dezhou Meng[5], Yiwei Fang[5], Miriam Rafailovich[5]

[1]*Palo Alto High School, Palo Alto, CA 94301*, [2]*Mount Hebron High School, Ellicott City, MD 21042*, [3]*North Allegheny Senior High School, PA, 15143*, [4]*Martin Luther King High School, Riverside, CA 92508*, [5]*Stony Brook University, Stony Brook, NY 11794*

**All contributed equally, listed alphabetically*

Both metals (e.g. gold, copper, platinum) and non-metals (e.g. arsenic, silicon) are commonly used as electrical conductors. While effective, metals are highly susceptible to corrosion, especially for under-water applications. As for non-metals, many conductors are produced through pollutive methods or contain materials toxic to humans and the environment (e.g. carbon nanotubes)[1]. This study presents the synthesis and characterization of a fully biodegradable, non-toxic, and conductive polymer nanocomposite consisting of a blend of Polylactic Acid (PLA), polybutylene adipate-co-terephthalate (PBAT), and graphene nanoplatelets (GNP H-5).

The synthesized materials achieved conductivity above 1 S/m, comparable or better to many conductive non-metals. Furthermore, this study found that printed samples are stronger than molded, a result that has not been achieved by previous studies on GNP. With rising demand for sustainable and conductive materials, particularly in flexible electronics and 3D printing, this research addressed the limitations of conventional metal, petroleum, and carbon-based conductors by developing a green alternative that is printable, biodegradable, ductile, and non-corrosive.[2]

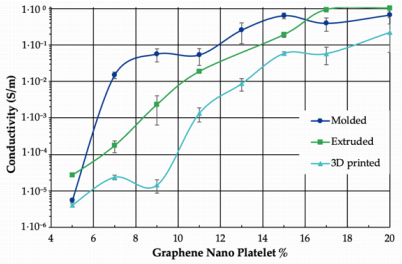

Figure 1. Electrical conductivity of molded, extruded, and 3D printed PLA/PBAT-graphene composites vs. GNP content. Conductivity increased with GNP loading. Percolation occurred at 7% (molded) and 11% (3D printed); molded samples had the highest values.

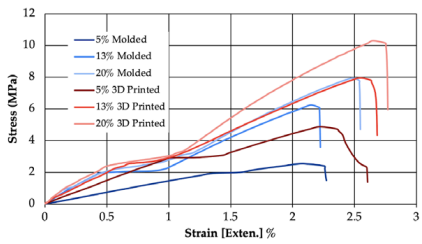

Figure 2. Stress-strain curves for molded and 3D printed blends with 5%, 13%, and 20% GNP. Toughness, Young's modulus, and ultimate strength increased with GNP loading, with 3D printed samples consistently higher.

PBAT and PLA were combined in a 3:1 ratio and blended with varying concentrations (5–20%) of GNPs using extrusion, molding, and 3D printing. Two-point probe electrical conductivity testing revealed that conductivity increased with GNP content, achieving percolation thresholds at 7% for molded samples and 11% for printed (Fig. 1). Maximum conductivities were 0.668 S/m (molded), 1.037 S/m (extruded), and 0.222 S/m (3D printed), making the material comparable to similar non-metal conductors. Contact angle testing on polymer interactions also revealed that GNP was most attracted to PBAT (35.6°), and PBAT and PLA had low attraction (58.2°), which suggests the molded samples' enhanced conductivity could be attributed to GNP localization at PLA-PBAT interfaces.

Mechanical testing showed improved tensile strength, toughness, and Young's modulus with higher GNP loading, and printed sample points were consistently higher than their corresponding molded ones (Fig. 2). Impact testing showed no significant increase in brittleness with increasing GNP %, with 3D printed showing higher breaking energy than molded (Fig. 3).

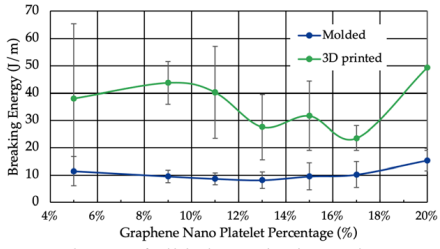

Figure 3. Breaking energy of molded and 3D printed PLA/PBAT-graphene nanocomposites across 5-20% GNP weight from impact testing. 3D printed samples were consistently stronger than molded, and showed no significant increase in brittleness with increasing GNP %.

Potential applications include flexible electronics, marine sensors, underwater electronics, wind turbine components, and other environments demanding lightweight, degradable, and high-performance conductive materials. Future work includes further contact angle data collection, TEM imaging, and SEM imaging to confirm GNP localization at the PLA-PBAT interface. Additionally, work with comparing conductivity against new ratios of PBAT to PLA and running biodegradability testing with ASTM standards.

[1]Shikha Awasthi, et al., Environmental Advances, Volume 18, 2024, 100601, ISSN 2666-7657

[2]Christian Apostol, Avishek Mojumdar, Journal of Undergraduate Chemical Engineering Research, Volume 14, May 2025, ISSN 2373-4221

Unraveling the morphology of PS/PLA homopolymer blends by planar-substrate model system

Eric Lin[1], Brenna Ren[2], Kaden Ren[3], Zhixing Huang[4], Miriam Rafailovich[4]

[1]*Adlai E. Stevenson High School, Lincolnshire, IL,* [2]*The Harker School, San Jose, CA,* [3]*Martin Luther King High School, Riverside, CA,* [4]*Department of Materials Science and Chemical Engineering, Stony Brook University, Stony Brook, NY*

Plastic pollution has become a major environmental issue due to the widespread use of polymer materials in industrial and commercial applications, driven by their low weight, durability, and ease of processing. Poly(lactic acid) (PLA) has gained attention as a renewable, biodegradable, and biocompatible alternative[1,2]. Various methods, such as foaming, injection molding, cold-drawing, and electrospinning, have been developed to improve PLA properties[3,4,5], with immiscible polymer blending being one of the most cost-effective and scalable approaches[6].

In this study, two polystyrenes (PS) with different molecular weights were blended with PLA to investigate: (I) the effect of PS molecular weight and (II) the PS/PLA weight ratio on blend morphology, using planar silicon substrates and appropriate characterization techniques.

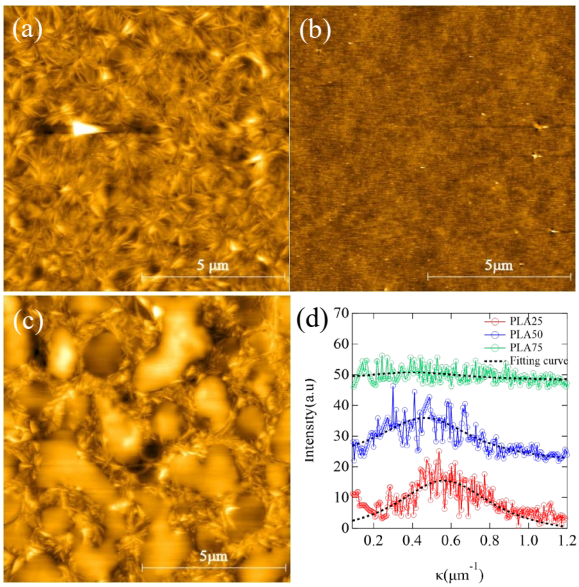

Figure 1. AFM topographic image of (a) PLA111K, (b) PS280K, and (c) PLA-50, (d) 1D FFT profiles

For hydrophobic PS and PLA, Si wafers were immersed in hydrofluoric solution to make a hydrophobic surface. Thin film morphology was analyzed by AFM at room temperature. Blends with varying PS:PLA ratios were prepared in a chloroform solvent and labeled by PLA content (e.g., PLA-25 = 25 wt% PLA, 75 wt% PS), ranging from PLA-0 (100% PS) to PLA-100 (100% PLA).

Figure 1(a–c) shows AFM height images of all 150 nm-thick PS280K/PLA films, revealing μm-scale phase separation due to a strong contrast between semicrystalline PLA and amorphous PS. The 1D FFT profiles in Figure 1(d) show a broad peak in the $\kappa = 0.4–0.6\ \mu m^{-1}$ range, indicating characteristic domain spacing. Notably, the peak position shifts toward the lower-κ region as PLA content increases, suggesting a strong dependence of domain spacing on blend composition. To enable quantitative comparison, each profile was fitted using a single Lorentzian function to extract the peak position.

Our results demonstrate that the morphology of PS/PLA blends can be effectively tuned by adjusting the PLA weight fraction, with phase separation occurring at the micron scale. This tunable morphology offers valuable insights into the design of biodegradable polymer systems in environmental applications. Furthermore, the findings lay a foundation for future studies on nanoconfinement effects in PS/PLA phase-separated structures.

[1]Shalem, Adi, et. al. *Environmental Biotechnology*. 2024.

[2]Xu, Bin, et. al. *Environmental Reviews*. 2022.

[3]Liu, Xiaohua, et. al. *Ann Biomed Eng*. 2004.

[4]Ghosh, Satyabrata, et. al. *Acta Biomaterialia*. 2008.

[5]Virgilio, Nick, et. al. *Biomaterials*. 2010.

[6]Gu, Liangliang, et. al. *Polymer*. 2018.

Local morphological changes of PS/PLA blends in Si substrate based thin films

Eric Lin[1], Brenna Ren[2], Kaden Ren[3], Zhixing Huang[4], Miriam Rafailovich[4]

[1]Adlai E. Stevenson High School, Lincolnshire, IL, [2]The Harker School, San Jose, CA, [3]Martin Luther King High School, Riverside, CA, [4]Department of Materials Science and Chemical Engineering, Stony Brook University, Stony Brook, NY

Polymer thin film-based materials are now widely used across applications ranging from consumer products to heavy industry[1,2], so it is crucial to accurately predict their performance[3]. Polymer-solid interfacial microscopic properties strongly influence macroscopic material properties, understanding this interface is key for developing next-generation polymeric systems[4]. As described in the previous abstract, a polystyrene (PS)/poly(lactic acid) (PLA) blend system was selected for this study. The objectives are to investigate: (I) nanoconfinement effects induced by solid surfaces, and (II) the influence of PS/PLA weight ratio on blend morphology. To create a hydrophobic substrate suitable for the hydrophobic PS and PLA, silicon wafers were treated with hydrofluoric acid to remove the native oxide layer. Thin film morphologies were characterized by atomic force microscopy (AFM) at room temperature. Blends with varying PS:PLA ratios were prepared with chloroform solvent and labeled according to PLA content (e.g., PLA-25 = 25 wt% PLA, 75 wt% PS), ranging from PLA-0 (pure PS) to PLA-100 (pure PLA). Film thicknesses from a few nanometers up to ~60 nm was achieved by diluting stock solutions to appropriate concentrations.

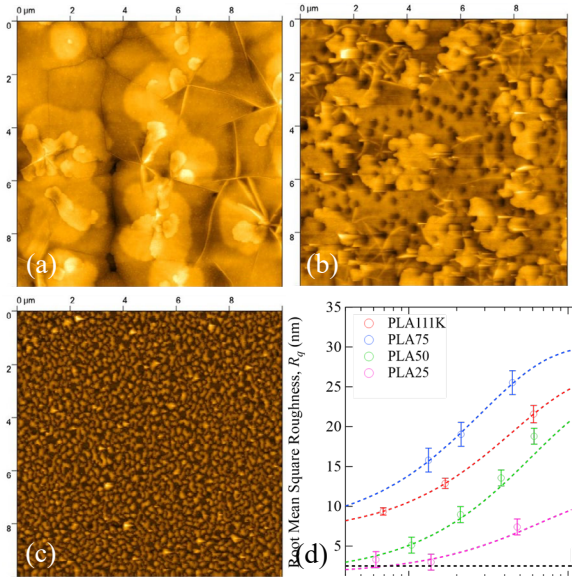

Figure 1. AFM topographic image of PLA111K (a) 61nm, (b) 17nm and (c) 6nm. (d) Thickness dependent of root mean square roughness (R_q).

Figure 1(a–c) shows AFM images of PLA111K ultrathin films with thicknesses ranging from 6 to 61 nm. As the thickness decreases, a clear suppression of crystallinity is observed, attributed to increasing nanoconfinement effects imposed by the Si substrate (add reference). Figure 1(d) presents the thickness-dependent root mean square roughness (R_q), obtained from 10 × 10 μm AFM height profiles. The R_q vs. thickness data were fitted using an exponential decay function, $f(x) = y_0 + A_0 * \exp(-invTau * x)$. For PLA111K, the results show that nanoconfinement strongly inhibits crystallization at reduced thickness, with a pronounced drop in roughness observed between 100 nm and 10 nm. In the PS/PLA blend system, introducing a small amount of PS increases surface roughness due to disrupted crystalline domains. However, further addition of PS, which is amorphous, leads to smoother surfaces. Similar to the neat PLA, the blend system also exhibits a "roughness rapid decrease region," highlighting the role of nanoconfinement and composition on surface morphology.

[1]Yang, Yuhui, et. al. *ACS Applied Materials & Interfaces*. 2021.

[2]Yang, Yuhu et. al. *The Journal of Physical Chemistry C.* 2021.

[4]Xu, Jie et. al. *Science.* 2017.

[4]Jiang, Naisheng, et. al. *Macromolecular Chemistry and Physics.* 2018.

Session IX: Nanoparticles for Catalysis and Enzymatic Reactions

Chairs:

Adam Hansen, Rebecca Isseroff, Md Ashraf Islam, Hyeonji Park

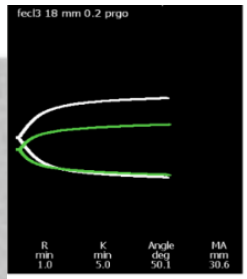

Figure 1: Comparison of TEG results between 0.2mM $FeCl_3$ pRGO solution (white) and normal pRGO (green).

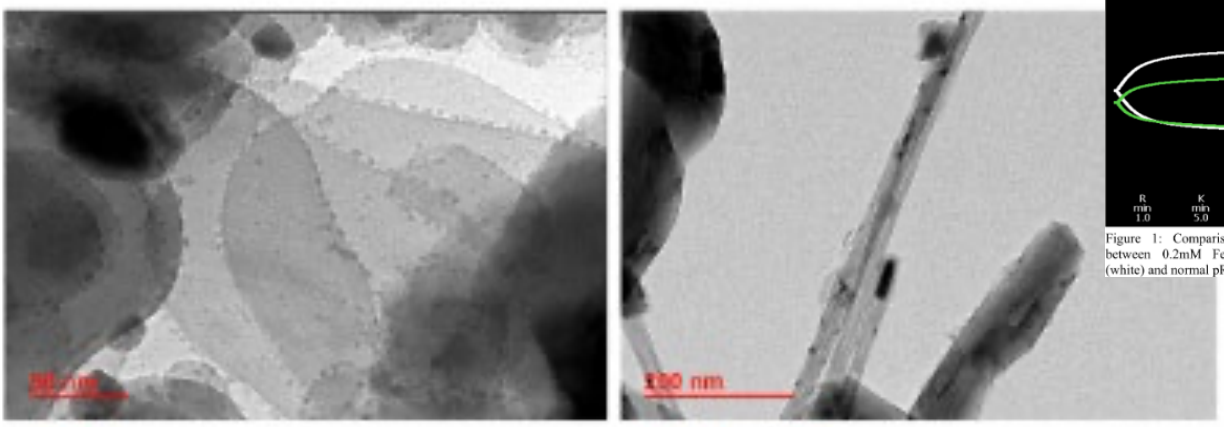

Figure 2: TEM imaging of 3 wt% CoO_x/hBN (left) and 1 wt% CuO_x/BNNT (right)

Comparing the Properties of GO, pRGO, and Metallized pRGO

Diana Sun[1], Julianne Mayetani[2], Shawn Lim[3], Leon Zhou[4], Adam Hansen[5], John Jerome[5], Rebecca Isseroff[5], Miriam Rafailovich[5]
[1]*Jericho Senior High School,* [2]*Palos Verdes Peninsula High School,* [3]*Syosset High School,* [4]*Rye Country Day School,*
[5]*Department of Materials Science and Chemical Engineering, Stony Brook University, NY, 11794*

Graphene oxide (GO) is a compound synthesized by oxidizing graphite. Partially-reduced graphene oxide (pRGO) removes some functional groups from GO which increases its conductivity. Previously, pRGO was found to enhance the enzymatic activity of thrombin when acting in fibrinogen clot formation[1] , as well as to assist yeast catalysis of hydrogen peroxide decomposition[2]. Furthermore, the nontoxic transition metals iron (III) chloride ($FeCl_3$) and cobalt (II) chloride ($CoCl_2$) were considered for their potential to improve the efficacy of pRGO[3]. In this study, the differing properties of GO, pRGO, and metallized pRGO were analyzed for a variety of biomedical applications.

0.025 mM, 0.05 mM, and 0.2 mM concentrations of $FeCl_3$ and $CoCl_2$ were dissolved in a 1 mg/mL GO solution and reduced with 18 mM sodium borohydride ($NaBH_4$). Thrombin (0.025 µg/mL) was used to promote fibrinogen (4 mg/mL) clotting in a thromboelastograph (TEG), which analyzes clot formation properties, including clotting time (R) and maximum amplitude. It was found that the 0.2 mM solution of reduced $FeCl_3$/pRGO performed better than the non-metallized 18 mM pRGO (Fig. 1). Reduced 0.2 mM $FeCl_3$ was tested without any thrombin, and it demonstrated no clot formation (Fig. 2). This result suggests that $FeCl_3$ does not act directly on fibrinogen, validating the earlier finding that $FeCl_3$/pRGO promotes thrombin's enzymatic activity and hastens clotting.

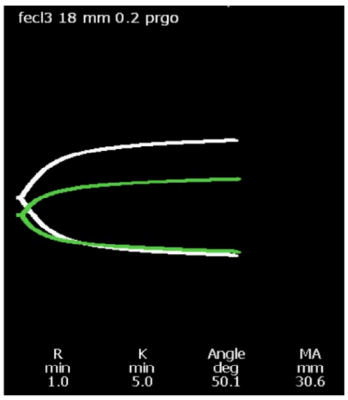

Figure 1: Comparison of TEG results between 0.2mM $FeCl_3$ pRGO solution (white) and normal pRGO (green).

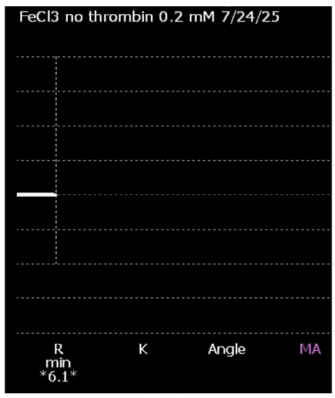

Figure 2: TEG graph of 0.2 mM $FeCl_3$ solution with no thrombin

To study the cytotoxicity of pRGO, HUVEC cell cultures were exposed to pRGO in concentrations of 0.042, 0.031, 0.019, and 0.008 mg/mL and incubated for 24 hours. Cell counting before and after exposure showed that there was an insignificant difference in the number of cells between the control and the cells exposed to increasing concentrations of pRGO, indicating that pRGO is not heavily cytotoxic (Fig. 3).

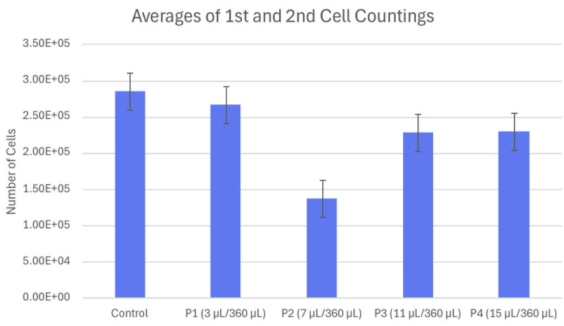

Figure 3: Averages of 1st and 2nd HUVEC cell countings of the Control, P1 (0.008 mg/mL), P2 (0.019 mg/mL), P3 (0.031 mg/mL), and P4 (0.042 mg/mL) groups.

Future research will investigate the effects of metallized pRGO on the catalytic activity of yeast-mediated hydrogen peroxide decomposition and processing through a nitrocellulose filter for antibacterial applications.

[1]Emily Zhang , Jennifer Gao, Rebecca Isseroff, Miriam Rafailovich, ***Effect of GO and pRGO on Thrombin Activity and Fibrinogen Clot Formation,*** Materials Research Society Fall Meeting 2024 Oral Presentation.

[2]Sophia Bracco, Sergio Rosa, Dominic Rossiello, Sam Specht, Rebecca Isseroff, Miriam Rafailovich, ***Testing the Potential of Partially-Reduced Graphene Oxide as a Catalyst Enhancer***, Materials Research Society Fall Meeting 2023 Oral Presentation.

[3]Nielsen, V. G., Goff, T., Hunsaker, B. D., & Neves, C. D. (2023). The gilded clot: Review of metal-modulated platelet activation, coagulation, and fibrinolysis. International Journal of Molecular Sciences, 24(4), 3302. https://doi.org/10.3390/ijms24043

A Novel Approach of Developing Metal Oxide + hBN/BNNT Nanocatalysts: Fundamental Studies of BN Materials and Support Effect on TMO_x

Krish Patel[1], Md Ashraful Islam[2], Tae Jin Kim[2], Miriam Rafailovich[2]
[1]*The Academy for Mathematics, Science, and Engineering, Rockaway, NJ, 07866,* [2]*Department of Materials Science and Chemical Engineering, Stony Brook University, Stony Brook, NY 11794*

Catalytic oxidation of toxic carbon monoxide (CO) is a key reaction for air pollution control, exhaust purification, and indoor CO poisoning mitigation. Therefore, developing stable, efficient, and cost effective catalysts for this reaction is crucial.[1] While noble metals such as Pd and Pt traditionally offer greatest catalytic activity, their high cost limits widespread application. However, transition metal oxides (TMO_x) have emerged as a promising catalysts for CO oxidation due to their lower cost and demonstrated catalytic activity at moderate temperatures; still, a strong support material is required to facilitate its catalytic activity.[2] Tangentially, hexagonal boron nitride (hBN) and boron nitride nanotubes (BNNT) are thermally stable and chemically inert, making them promising support catalysts. With a 2D wafer structure similar to graphene, hBN enables a high dispersion of metal nanoparticles on its surface and reduces agglomeration. Structurally similar to carbon nanotubes (CNTs), BNNT has a wide band gap of ~5.9 eV, owing to its ability to maintain its structure up to 900°C.[3]

Two 1 wt% CuO_x/hBN, one 1 wt% CuO_x/BNNT(80), one 3 wt% CoO_x/hBN, and one 3 wt% CoO_x/BNNT catalysts were synthesized with the one-pot chemical vapor deposition method (OP-CVD), which includes a pre-mixing to ensure homogeneity of metal precursor and support, evaporation to disperse the TMO_x precursor, and calcination fixation step, promoting the formation of a well dispersed TMO_x on the hBN/BNNT support catalyst (Figure 1). For this synthesis the copper precursor $Cu(acac)_2$ and the cobalt precursor $Co(acac)_2$ were used; hBN and BNNT(80) were chosen.[4]

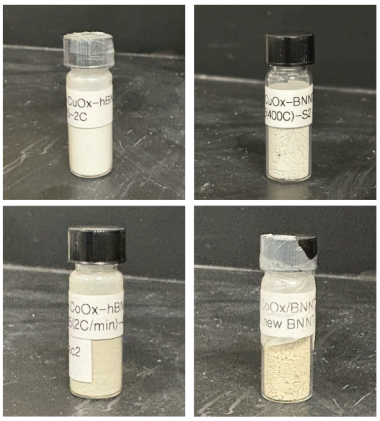

Figure 1: synthesized nanocatalysts–top left, CuO_x/hBN; top right, CuO_x/BNNT; bottom left, CoO_x/hBN; bottom right, CoO_x/BNNT

The catalytic activity test of 40 mg of both CuO_x/hBN and CuO_x/BNNT catalysts was performed in a fixed-bed flow reactor, which regulated appropriate flow rates for the carrier gas He, reactant gases 10% CO and O2, and product gas CO2. To analyze the support effect (hBN vs BNNT) and TMO_x effect (CuO_x vs CoO_x), a temperature vs CO% curve was produced. Comprehensive characterization methods such as Transmission Electron Microscopy (TEM) and Fourier Transform Infrared Spectroscopy (FTIR) were applied to illustrate physicochemical properties and validate catalytic activity (Figure 2). The techniques confirmed that the CoOx/hBN sample exhibited the least agglomeration with the greatest dispersion at the edge of hBN wafers. This study validated a method to produce catalytic synthesis of metal oxides at 1 and 3 wt% for both hBN and BNNT and affirmed cobalt oxide's greater synergistic effect with hBN/BNNT as compared to copper oxide.

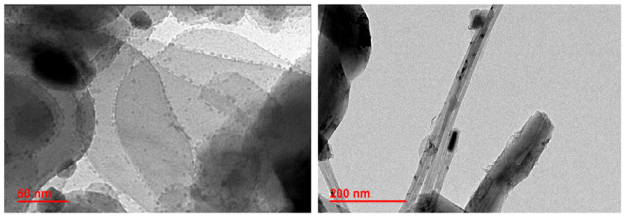

Figure 2: TEM imaging of 3 wt% CoO_x/hBN (left) and 1 wt% CuO_x/BNNT (right)

[1] Herz, R. K. (1990, June). CO-oxidation catalysts: Low-temperature CO oxidation over Noble-Metal Reducible Oxide (NMRO) catalysts. NASA, Langley Research Center, Low Temperature CO-Oxidation Catalysts for Long-Life CO2 Lasers. https://ntrs.nasa.gov/citations/19900015272
[2] Dey, S., Dhal, G.C., Mohan, D. et al. Advances in transition metal oxide catalysts for carbon monoxide oxidation: a review. Adv Compos Hybrid Mater 2, 626–656 (2019). https://doi.org/10.1007/s42114-019-00126-3
[3] Seo, J.-W., Amol Pophali, An, S., Seng, C., Li, S., Liu, H., Kim, J., An, K., Kim, J., & Kim, T. (2024). Fundamental structural study of hexagonal boron nitride (h-BN) and boron nitride nanotube (BNNT) at low and high temperatures. Journal of Molecular Structure, 1319, 139545–139545. https://doi.org/10.1016/j.molstruc.2024.139545
[4] Pophali, A., Shimogawa, R., Zhang, L., Kwon, G., Yoon, K., Roh, J., Kim, D. H., Song, H., Frenkel, A. I., & Kim, T. (2024). Development of ceria-supported metal-oxide (MOx/CeO2) catalysts via a one-pot chemical vapor deposition (OP-CVD) technique: Structure and reverse water gas shift reaction study. Chemical Engineering Journal, 504, 158726. https://doi.org/10.1016/j.cej.2024.158726

Characterization of the Freezing and Melting Behavior of Lithium Chloride Aqueous Solutions

Andrew Wang[1], Juwon Kim[2], Hyeonji Park[3], Taejin Kim[3], Miriam Rafailovich[3]

[1]Riverdale Country School, Bronx, NY, 10471, [2]Seoul Academy, Seoul, Republic of Korea, 06200, [3]Department of Materials Science and Chemical Engineering, Stony Brook University, Stony Brook, NY, 11794

Lithium chloride (LiCl) aqueous solutions are widely used in chemical, biological, and industrial applications due to their high solubility, strong hygroscopic properties, and antifreeze properties. Among various salts, LiCl stands out due to its ability to depress the freezing point of water, which is crucial for preventing road and soil erosion and transporting organs. This study investigated how the Li^+ and Cl^- ions influence the structure and dynamic behavior of water molecules as they freeze.

To accurately characterize this behavior, in-situ Raman spectroscopy was employed. Raman spectroscopy is a well-known tool for analyzing the behavior of water molecules. Raman scattering from liquid H_2O includes the OH stretching vibration band (ν_1) at 2800–3800 cm^{-1}, the bending band (ν_2) near 1645 cm^{-1}. At low temperatures, the solution crystallizes, resulting in peaks in the 100–400 cm^{-1} range. Moreover, asymmetric OH stretching dominates in the liquid state, whereas in the solid state, symmetric OH stretching is more prominent.[1] By analyzing the intensity and shifting of these bands, insight is gained into how the ions affect the vibrational modes of water molecules, from which we can infer the structure of the electrolyte solution.

In this study, Raman spectroscopy was introduced to characterize the antifreezing behavior of LiCl across varying concentrations and ramping rates. Additionally, the freezing and melting transitions of a 1.5 M LiCl solution were observed using visual indicators, methylene blue and food dye, to highlight the color changes associated with the liquid and solid states. Raman data were plotted using the software OriginLab. The Raman results for all concentrations were graphed and analyzed, and three relevant regions were identified for each sample: the intramolecular hydrogen bond vibration peak, HOH bending peak, and OH stretching peak (Figure 1[2-4]). For each sample, the appearance of the intramolecular peak and the dominance of the symmetric stretching peak over the asymmetric stretching peak were simultaneous. These changes indicated the presence of one phase transition temperature. The disappearance of the HOH bending peak, which occurred at a lower temperature, indicated a second phase transition temperature. Furthermore, changes in the structure of ice as temperature decreased were identified by analyzing spectral shifts: blue shifts (toward higher frequencies) and red shifts (toward lower frequencies). The results indicated that increasing LiCl concentration leads to the depression of the freezing point. The presence of two distinct phase transition temperatures indicated the existence of two structural changes. This study is expected to contribute to a deeper understanding of ion-specific effects on water structure and phase transitions by showing how concentrations influence Raman shifts and freezing point depression.

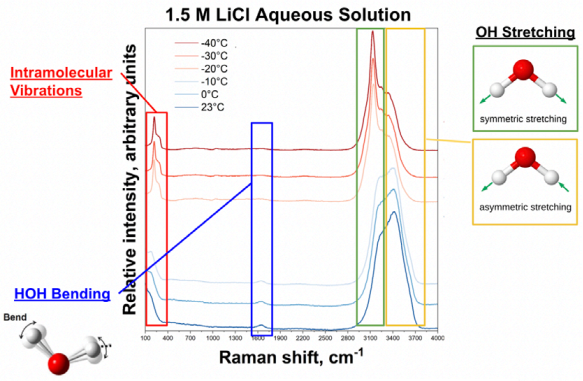

Figure 1. Raman spectra of a 1.5M LiCl solution as it freezes. The intramolecular, HOH bending, and OH stretching bands are highlighted.

(1) Maeda, Y.; Kitano, H. The Structure of Water in Polymer Systems as Revealed by Raman Spectroscopy. *Spectrochim. Acta. A. Mol. Biomol. Spectrosc.* **1995**, *51* (14), 2433–2446. https://doi.org/10.1016/0584-8539(95)01446-2.

(2) Ludwig, R. Water: From Clusters to the Bulk. *Angew. Chem. Int. Ed.* **2001**, *40* (10), 1808–1827. https://doi.org/10.1002/1521-3773(20010518)40:10<1808::AID-ANIE1808>3.0.CO;2-1.

(3) Yu, C.-C.; Chiang, K.-Y.; Okuno, M.; Seki, T.; Ohto, T.; Yu, Xi.; Korepanov, V.; Hamaguchi, H.; Bonn, M.; Hunger, J.; Nagata, Y. Vibrational Couplings and Energy Transfer Pathways of Water's Bending Mode. In Review July 28, 2020. https://doi.org/10.1038/s41467-020-19759-w.

(4) *Vibrational Dynamics - strawberry fields*. Vibrational dynamics - Strawberry Fields. (n.d.-a). https://strawberryfields.ai/photonics/apps/run_tutorial_dynamics.html

Session X: TiO_2 Nanoparticles

Chairs:

Huiting Luo, Muyun Cui, Jessica Hofflich, Shi Fu

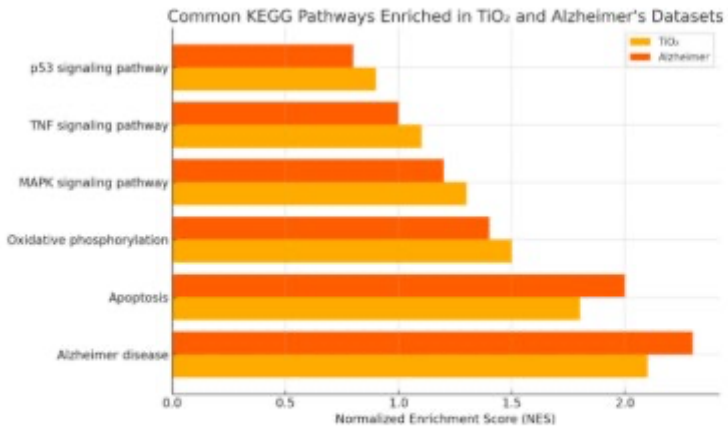

Fig 1. Common KEGG Pathways Enriched in TiO2 and Alzheimer's Datasets

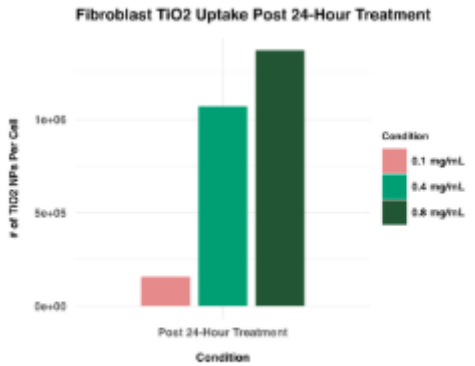

igure 4: TiO_2 absorption for FBs post 24-hour treatment

Quantifying TiO_2 Nanoparticle Uptake and Its Effects on Proliferation of Human Endothelial Cells and Fibroblasts

Ahyoung Song[1], Chunman Li[2], Emily Segall[3], Charlotte Huang[4], Suhrith Muvvala[5], Felicity Liao[6], Alyssa Wang[7], Shuyan Li[8], Sean Lee[9], Lucas Hofflich[10], Harper Falivene[11], Briman Yang[12], Huiting Luo[12], Muyun Cui[12], Jessica Hofflich[12], Shi Fu[12], Miriam Rafailovich[12]

[1] International Academy, Troy, MI 48083, [2] Beijing World Youth Academy, Beijing, [3] Yeshiva University High School for Girls, Queens, NY 11423, [4] W.T. Clarke High School, Westbury, NY 11590, [5] Portola High School, Irvine, CA, 92618, [6] Cushing Academy, Ashburnham, MA 01430, [7] East Ridge High School, Woodbury, MN 55129, [8] Suzhou North America High School, Jiangsu, China 215000, [9] Lambert High School, Suwanee,GA 30024, [10] Tuckahoe High School, Eastchester, NY 10709, [11] South Side High School, Rockville Center, NY 11570, [12] Stony Brook University, NY, 11790

Titanium dioxide (TiO_2) nanoparticles (NPs) are widely used in industrial and biomedical settings, but concerns about their cytotoxicity have risen in recent years due to TiO_2 NPs' ability to reduce cell viability by inducing production of reactive oxygen species.[1,2] However, TiO_2 toxicity requires further research and it is still unclear whether its effects stem from cellular uptake or extracellular accumulation. This study aims to quantify TiO_2 NP uptake using ICP-OES and evaluate the effects of treatment time and concentration on proliferation in human umbilical vein endothelial cells (HUVECs) and fibroblasts (FBs).

Cultured HUVECs were exposed to 0.1 and 0.2 mg/mL rutile TiO_2 NPs with ~50 nm diameter for 24 and 48 hours, and FBs were treated with 0.1, 0.4, and 0.8 mg/mL for 24 hours. Cell proliferation was quantified via cell counting after harvesting on days 1, 3, and 5 post-TiO_2 exposure. After counting, the cells were centrifuged and diluted with deionized water for ICP-OES analysis.

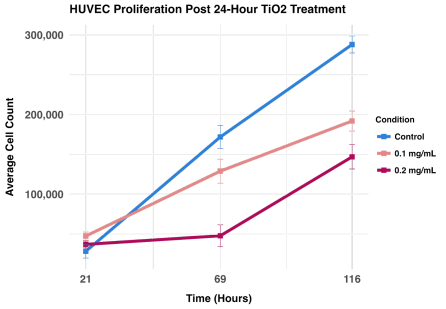

Figure 1: HUVEC proliferation post 24-hour exposure to 0, 0.1, 0.2 mg/mL TiO_2

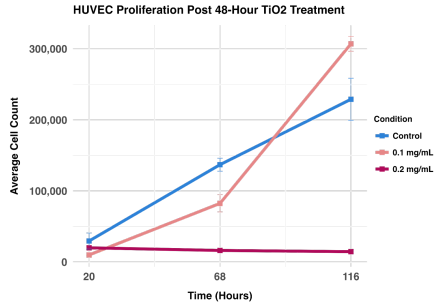

Figure 2: HUVEC proliferation post 48-hour exposure to 0, 0.1, 0.2 mg/mL TiO_2

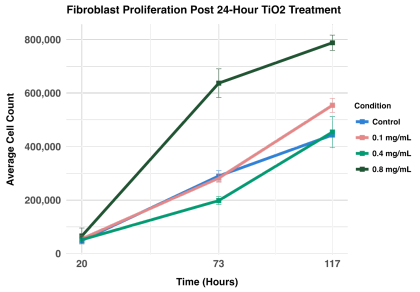

Figure 3: FB proliferation post 24-hour exposure to 0, 0.4, 0.8 mg/mL TiO_2

HUVEC proliferation decreased with higher TiO_2 concentration and exposure time, with the 0.2 mg/mL group experiencing a significant decrease in proliferation when exposed to TiO_2 for 48 hours (Fig. 1), while a decay in proliferation was also observed after 24 hours (Fig. 2). 0.1 mg/mL of TiO_2 observed decreased proliferation at 24 hours of exposure, however, it increased at 48 hours, suggesting a threshold effect for TiO_2 exposure. FBs were more resistant to TiO_2 exposure than HUVECs, suggesting cell-specific responses (Fig. 3).

Results from ICP-OES for FBs showed 4.45%, 7.59% and 7.61% TiO_2 NP absorption for 0.1 mg/mL, 0.4, and 0.8 mg/mL, respectively. This constitutes over a million TiO_2 NPs being absorbed per cell, which indicates that toxicity may originate from within the cell. Further studies need to be conducted on the specific biological mechanisms of TiO_2 NP activity on cell viability through RT-PCR and RNA-sequencing.

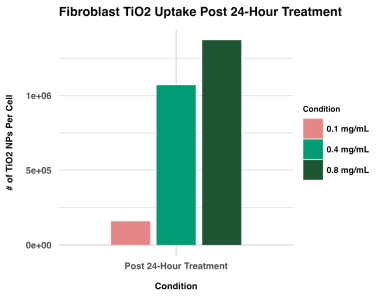

Figure 4: TiO_2 absorption for FBs post 24-hour treatment

[1] Gojznikar, J., Zdravković, B., Vidak, M., Leskošek, B., & Ferk, P. (2022). TiO2 Nanoparticles and Their Effects on Eukaryotic Cells: A Double-Edged Sword. *International journal of molecular sciences*, *23*(20), 12353. https://doi.org/10.3390/ijms232012353

[2] Fattori, A. C. M., et al. (2023, March 22). Titanium dioxide nanoparticle (TiO_2 NP) induces toxic effects on LA-9 mouse fibroblast. Cellular Physiology and Biochemistry, 57, 63–81. https://doi.org/10.33594/000000616

Decoding the Crosstalk: Computational Analysis of TiO_2 Exposure and Its Overlap with Alzheimer's and Osteoporotic Signaling

Xinying (Louis) Li[1], Muyun Cui[2], Miriam Rafailovich[2]

[1]*Shenzhen Middle School, Guangdong, China 518000,* [2] *Stony Brook University, Stony Brook, NY 11794, USA*

Nanoparticulate Titanium Dioxide (TiO_2 NPs) is a widely used material in biomedical and cosmetic applications. In recent years, the cytotoxic potential of TiO_2 NPs to produce reactive oxygen species (ROS)—causing cellular damage, inflammatory responses, and altered gene expression—has drawn increasing attention. However, possible common pathways between TiO_2-induced oxidative damage and other ROS-related diseases have not yet been thoroughly investigated. In this study, computational analysis was implemented to explore shared functional and molecular mechanisms between TiO_2-treated cellular responses and oxidative stress–related diseases, including Alzheimer's disease (AD) and osteoporosis.[1]

Data from human dendritic cells treated with 10 µg/mL TiO_2 NPs for 24 hours (GSE39316) and brain tissue samples from multiple regions of AD patients (GSE5281) were obtained from the Gene Expression Omnibus (GEO) and preprocessed.[2,3] Using linear modeling for microarray and RNA-seq data in R, differential expression analysis was conducted between control and treated/affected groups, generating differentially expressed genes (DEGs) for both TiO_2-treated and AD-affected samples. Gene set enrichment analysis (GSEA) using clusterProfiler was performed to calculate normalized enrichment scores (NES), reflecting the enrichment intensity of KEGG pathways. Overlapping KEGG pathways enriched in both datasets were then identified and visualized.

The horizontal bar chart highlights six major pathways upregulated in response to TiO_2 treatment or AD, with all showing NES > 0 (Figure 1). The high NES of the Alzheimer disease pathway reflects transcriptomic similarity between TiO_2-induced stress and AD pathology, suggesting that TiO_2 exposure may trigger or exacerbate neurodegeneration. Upregulated apoptosis, oxidative phosphorylation, and p53 signaling pathways indicate shared mitochondrial disruption and programmed cell death, supporting the hypothesis that TiO_2 damages mitochondrial structures and initiates apoptotic cascades. Meanwhile, the strong expression of MAPK and TNF signaling pathways mediates inflammation and stress responses, showing that TiO_2 exposure elicits reactions resembling chronic inflammation in AD brains.

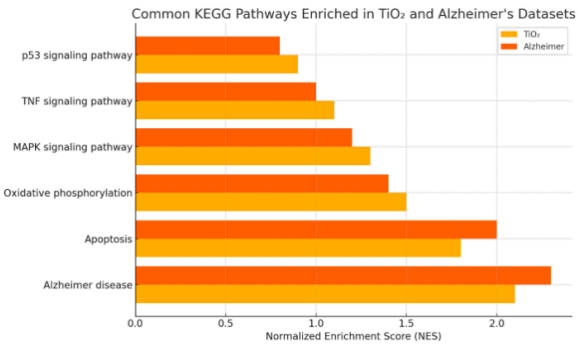

Fig 1. Common KEGG Pathways Enriched in TiO2 and Alzheimer's Datasets

Our results show that TiO_2 exposure activates key signaling pathways also enriched in Alzheimer's disease, highlighting a potential molecular link between nanoparticle exposure and neurodegeneration, and demonstrating the utility of computational analysis. Future work will extend the comparison to other oxidative stress–associated diseases such as osteoporosis.

[1] Manoharan, S., Guillemin, G. J., Abiramasundari, R. S., Essa, M. M., Akbar, M., & Akbar, M. D. (2016). *The Role of Reactive Oxygen Species in the Pathogenesis of Alzheimer's Disease, Parkinson's Disease, and Huntington's Disease: A Mini Review.* Oxidative medicine and cellular longevity, 2016, 8590578. https://doi.org/10.1155/2016/8590578

[2] Xu, M., Wang, Y., Xia, R., Wei, Y., Wei, L., Zhang, H., ... & Zhang, Z. (2013). *Titanium dioxide nanoparticle exposure induces functional impairments in human dendritic cells* [GSE39316]. NCBI Gene Expression Omnibus. https://www.ncbi.nlm.nih.gov/geo/query/acc.cgi?acc=GSE39316

[3] Liang, W. S., Dunckley, T., Beach, T. G., Grover, A., Mastroeni, D., Walker, D. G., ... & Stephan, D. A. (2007). *Gene expression profiles in anatomically and functionally distinct regions of the normal aged human brain* [GSE5281]. NCBI Gene Expression Omnibus. https://www.ncbi.nlm.nih.gov/geo/query/acc.cgi?acc=GSE5281

Phoebe Zheng

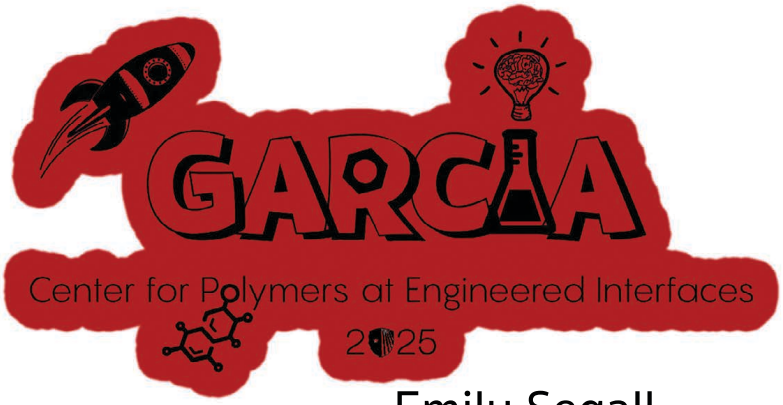

Emily Segall

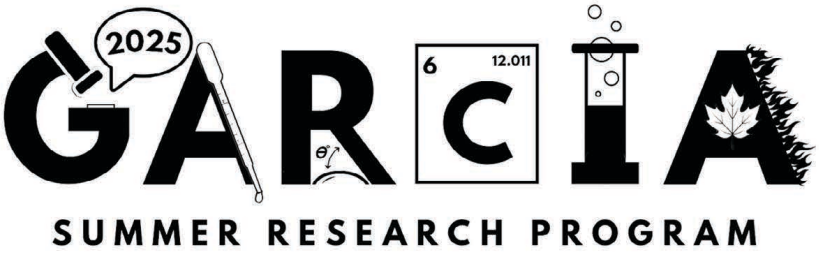

Danica Stout

Alice Hu

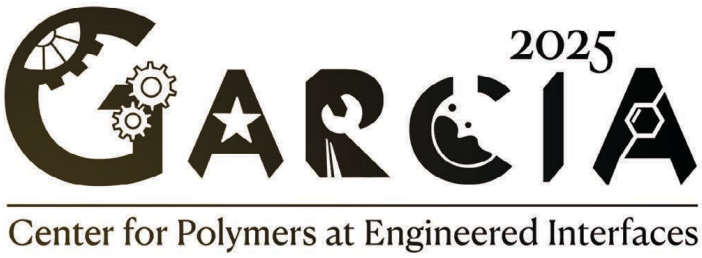

Chujia Yang

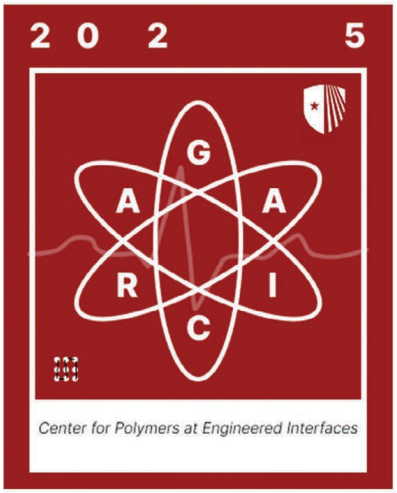

Emily Li

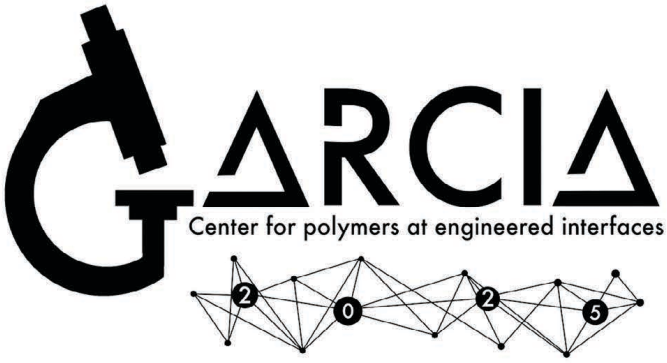

Nathaniel Gao

We gratefully acknowledge the support of the Louis Morin Charitable Trust

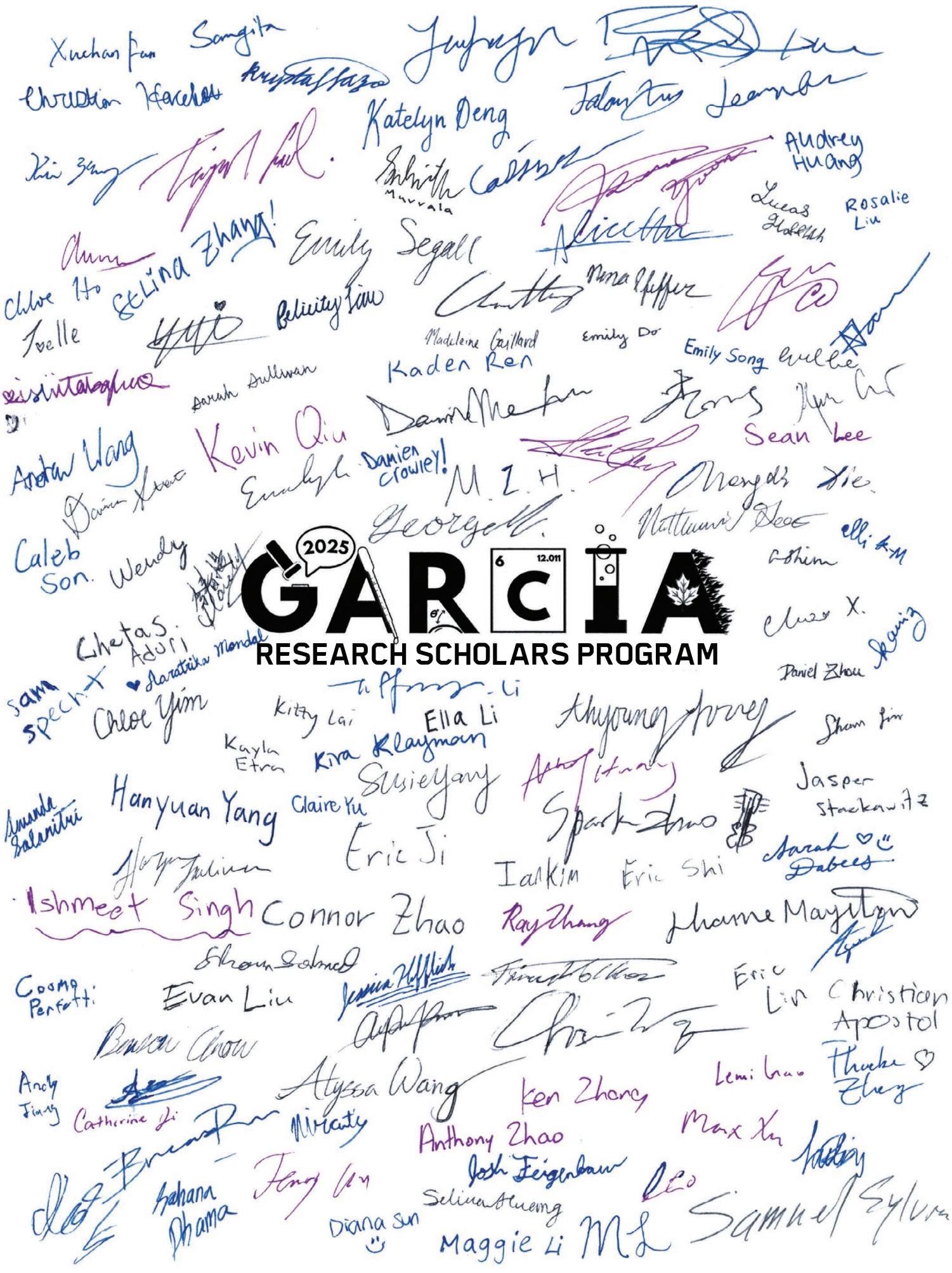
2025
GARCIA
6 12.011 C
RESEARCH SCHOLARS PROGRAM


Daniel Zhou
Sarah Sullivan
Maggie Li
Aaratrika Mondal
Rosalie Liu
Lemi Gao
Chloe Yim
Joelle Kim
Ryan Gu
Michael He
Selina Huang
Alice Hu
Cleo Xu
GARCIA
2025
Eric Shi
Alessandro Verona
Cassidy Kirschenbaum
Leo Pan-Wang
Thanks for a
great summer!